

**All-fiber Faraday Devices Based on
Terbium-doped Fiber**

by

Lei Sun

Submitted in Partial Fulfillment
of the
Requirements for the Degree
Doctor of Philosophy

supervised by

Professor John R. Marciante

The Institute of Optics
Arts, Sciences and Engineering
Edmund A. Hajim School of Engineering and Applied Sciences

University of Rochester
Rochester, New York

2010

Curriculum Vitae

The author was born in Tanggu, Tianjin, China, in 1978. He began his undergraduate studies in 1997 at the Physics Department of Nankai University, Tianjin, China, and received his B.S. degree in Applied Optics in 2001. In the same year, he entered the M.S. program at the Institute of Modern Optics, Nankai University, where he studied the fabrication and application of optical fiber gratings under the guidance of Prof. Xiaoyi Dong and received his M.S. degree in Optics in 2004. He started his graduate studies at the Institute of Optics, University of Rochester, in 2004. In 2005, the author began his doctoral research at the Laboratory for Laser Energetics, University of Rochester, where he studied all-fiber Faraday components and filamentation in large-mode-area fiber lasers under the guidance of Prof. John R. Marcante.

Publications

Journal Publications

- **L. Sun**, S. Jiang, and J. R. Marciante, "Compact all-fiber optical Faraday components using 65-wt% terbium doped fiber with a record Verdet constant of -32 rad/(Tm)," *Opt. Express* 18, 12191-12196 (2010)
- **L. Sun**, S. Jiang, and J. R. Marciante, "All-fiber optical Faraday mirror using 56-wt% terbium-doped fiber," *IEEE Photon. Technol. Lett.* 22, 999-1001 (2010)
- **L. Sun**, S. Jiang, and J. R. Marciante, "All-fiber optical magnetic-field sensor based on Faraday rotation in highly terbium-doped fiber," *Opt. Express* 18, 5407-5412 (2010), highlighted by *Nature Photonics*, 4, 425 (2010)
- **L. Sun**, S. Jiang, J. D. Zuegel, and J. R. Marciante, "All-fiber optical isolator based on Faraday rotation in highly terbium-doped fiber," *Opt. Lett.* 35, 706-708 (2010)
- **L. Sun**, S. Jiang, J. D. Zuegel, and J. R. Marciante, "Effective Verdet constant in a terbium-doped-core phosphate fiber," *Opt. Lett.* 34, 1699-1701 (2009)
- **L. Sun** and J. R. Marciante, "Filamentation analysis in large-mode-area fiber lasers," *J. Opt. Soc. Am. B* 24, 2321-2326 (2007)
- **L. Sun**, X. Feng, W. Zhang, et al, "Beating frequency tunable dual wavelength erbium-doped fiber laser with one fiber Bragg grating," *IEEE Photon. Technol. Lett.* 16(6): 1453-1455 (2004)
- **L. Sun**, X. Feng, Y. Liu, et al. "Moiré fiber Bragg grating written on prestrained fibers," *Chinese Phys. Lett.* 21(4): 669-670, (2004)

Conference Presentations

- **L. Sun**, S. Jiang, and J. Marciante, "All-fiber optical Faraday mirror," *CLEO 2010*, paper CMGG4

- **L. Sun**, S. Jiang, and J. Marciante, "All-fiber optical magnetic field sensor based on Faraday rotation," *OFC 2010*, paper OWL3
- **L. Sun**, S. Jiang, and J. Marciante, "Compact all-fiber optical Faraday isolator," **post-deadline**, *Photonics West 2010*, paper 7580-113
- **L. Sun**, S. Jiang, J. Zuegel, and J. Marciante, "All-fiber isolator based on Faraday rotation," in *Frontiers in Optics*, OSA Technical Digest (CD) (Optical Society of America, 2009), paper FTuD5
- **L. Sun**, S. Jiang, J. Zuegel, and J. Marciante, "Measurement of the Verdet constant in a Terbium-core-doped Fiber," in *Frontiers in Optics*, OSA Technical Digest (CD) (Optical Society of America, 2008), paper FWR2
- **L. Sun** and J. R. Marciante, "Filamentation analysis in large-mode-area fiber lasers," in *Frontiers in Optics*, OSA Technical Digest (CD) (Optical Society of America, 2006), paper FThN5

Patents

- Y. Liu, X. Dong, **L. Sun**, et al, "Single and Dual Wavelengths Switchable, Wavelength and Wavelength Spacing Tunable Erbium-doped Optical Fiber Laser," Chinese Patent, NO: 200310107066.2, 2004
- S. Yuan, W. Zhang, G. Kai, X. Dong, **L. Sun**, et al, "Meshed Optical Fiber Microbend Sensor," Chinese Patent, NO: 200320112295.9, 2004

Acknowledgments

This is a great opportunity to express my respect to Prof. John R. Marciante. I am deeply grateful for his guidance, support, and understanding for my doctoral studies. I feel fortunate to be under the mentoring of a great advisor for these years. Among all the merits of John, his creative thinking, experimental research experience, patience in technical writing, project and lab management skills, and humor impressed me most. I can not count how many times creative sparks were generated in our discussions. When I encountered experimental problems, he always found the reasons and helped me avoid detours. John is strict with us on scientific research, but not pushy. He guides us with direction, but does not limit us. He treats us not only as students, but also as friends. His advice in life and career development benefit us.

I would like to thank Prof. Govind P. Agrawal. I learned fundamental knowledge in fiber optics in his courses and benefited a lot from his wonderful text books in fiber optics. I am grateful to the members of my thesis committee, Prof. Govind P. Agrawal, Prof. Robert W. Boyd and Prof. Roman Sobolewski, for their valuable suggestions and questions. I sincerely thank all the faculty and staff members of the Institute of Optics. It is your professors that gave me comprehensive training in scientific research. Thanks to Joan Christian, Lissa Cotter, Gina Kern, Besty Benedict, Gayle Thompson and Noelene Votens for giving me great support during my studies.

I am grateful to Dr. Jonathan Zuegel, Prof. David Meyerhofer, and other scientists at the Laboratory for Laser Energetics (LLE) for their suggestions on technical writing and conference presentations. I would like to thank the Illustration Department of LLE for their preparation of my technical writing; Kathie Freson, Jennifer Taylor, Lisa Stanzel, Jennifer Hamson, Karen Kiselycznyk and Heidi Barcomb made beautiful figures and fluent text for me. Thanks to Sara Bodensteiner for her help in arranging my conference travel.

I would like to thank my colleagues in our research group, Zhuo Jiang, Weihua Guan, Jordan Leidner, Richard Smith, and Haomin Yao, for their help in the lab and discussions. The friendship from my classmates and friends in the Institute of Optics is important to me. Lianghong Yin, Weihua Guan and Li Ding gave me

great help for the first year when I came Rochester.

I would like to acknowledge the support of the Frank J. Horton fellowship from the LLE, University of Rochester. This thesis work was supported by the U.S. Department of Energy (DOE) Office of Inertial Confinement Fusion under Cooperative Agreement DE-FC52-08NA28302, the University of Rochester, and the New York State Energy Research and Development Authority. The support of DOE does not constitute an endorsement by DOE of the views expressed in this thesis. This work is also supported in part by Wright-Patterson Air Force Research Laboratory (AFRL) under contract FA8650-09-C-5433. I would like to acknowledge the technical support of Dr. R. L. Nelson and W. D. Mitchell from AFRL.

I am deeply grateful to my parents for encouraging me to pursue my education, for teaching me the value of experiences, and for their love.

Abstract

Surface damage is one of the most problematic power limits in high-power fiber laser systems. All-fiber Faraday components are demonstrated as a solution to this problem, since they can be completely fusion-spliced into existing systems, eliminating all glass-air interfaces. Beam filamentation due to self-focusing places another limit on the peak power attainable from fiber laser systems. The limits imposed by this phenomenon are analyzed for the first time.

The concept of an effective Verdet constant is proposed and experimentally validated. The effective Verdet constant of light propagation in a fiber includes contributions from the materials in both the core and the cladding. It is measured in a 25-wt% terbium-doped-core phosphate fiber to be -6.2 rad/(Tm) at 1053 nm, which is six times larger than silica fiber. The result agrees well with Faraday rotation theory in optical fiber.

A compact all-fiber Faraday isolator and a Faraday mirror are demonstrated. At the core of each of these components is an all-fiber Faraday rotator made of a 4-cm-long, 65-wt%-terbium-doped silicate fiber. The effective Verdet constant of the terbium-doped fiber is measured to be -32 rad/(Tm), which is $27\times$ larger than that of silica fiber. This effective Verdet constant is the largest value measured to date in any fiber and is 83% of the Verdet constant of commercially available crystals used in bulk-optics-based isolators. Combining the all-fiber Faraday rotator with fiber polarizers results in a fully fusion-spliced all-fiber isolator whose isolation is measured to be 19 dB. Combining the all-fiber Faraday rotator with a fiber Bragg grating results in an all-fiber Faraday mirror that rotates the polarization state of the reflected light by $88 \pm 4^\circ$.

An all-fiber optical magnetic field sensor is also demonstrated. It consists of a fiber Faraday rotator and a fiber polarizer. The fiber Faraday rotator uses a 2-cm-long section of 56-wt%-terbium-doped silicate fiber with a Verdet constant of -24.5 rad/(Tm) at 1053 nm. The fiber polarizer is Corning SP1060 single-polarization fiber. The sensor has a sensitivity of 0.49 rad/T and can measure magnetic fields from 0.02 to 3.2 T.

An all-fiber wavelength-tunable laser based on Faraday rotation is proposed. It consists of an all-fiber wavelength-tunable filter in a conventional fiber laser

cavity. The filter includes a fiber polarizer and a fiber Faraday mirror in which a chirped fiber Bragg grating is directly written onto the 65-wt% terbium fiber. The ytterbium-doped fiber in the laser is gain flattened using a 1030/1090 nm WDM filter, resulting a net gain ripple that is measured to be less than 0.2 dB from 1047 to 1060 nm. The wavelength tuning range of the resulting fiber laser is therefore expected to be in this 1047 to 1060 nm range.

Filamentation is one of the nonlinear peak-power-threshold limits in high-power fiber lasers. Starting from the paraxial wave equation, an analytic expression for the filamentation threshold in fiber lasers is derived using a perturbation method. The occurrence of filamentation is determined by the larger of two thresholds, one of perturbative gain and one of spatial confinement. The threshold value is around a few megawatts, depending on the parameters of the fiber.

Table of Contents

Foreword	1
Chapter 1	
Introduction	2
1.1 Brief Review of High-Power Fiber Lasers	2
1.2 Power-Threshold Limits in High-Power Optical Fiber Lasers	7
1.2.1 Nonlinear Effects	7
1.2.1.1 Stimulated Brillouin Scattering	7
1.2.1.2 Stimulated Raman Scattering	9
1.2.1.3 Self-Focusing	10
1.2.2 Thermal Effects	10
1.2.2.1 Thermal Fracture	10
1.2.2.2 Melting	11
1.2.2.3 Thermal Lensing	11
1.2.3 Optical Damage	12
1.3 Thesis Objective	12
1.4 Thesis Outline	14
Chapter 2	
Faraday Effect, Magneto-optical Materials, and Magnet Design	15
2.1 Faraday Effect	15
2.2 Magneto-Optical Materials	18
2.2.1 Diamagnetic Materials	19
2.2.2 Paramagnetic Materials	20
2.3 Magnet Design	21

Chapter 3

Effective Verdet Constant Model for Optical Fiber	29
3.1 Introduction	29
3.2 Theory	30
3.3 Experiment	31
3.4 Discussion	34

Chapter 4

Cleaving and Splicing of Terbium Fiber	36
4.1 Cleaving	36
4.2 Splicing	40
4.3 Coupling Efficiency	44

Chapter 5

All-Fiber Optical Faraday Components	48
5.1 All-Fiber Optical Faraday Isolator and Faraday Mirror	48
5.1.1 Introduction	48
5.1.2 Terbium Doped Optical Fiber	51
5.1.3 All-Fiber Polarizers	55
5.1.4 All-Fiber Optical Faraday Isolator	59
5.1.5 All-Fiber Optical Faraday Mirror	61
5.1.6 Discussion	66
5.2 All-fiber Optical Magnetic Field Sensor	67
5.2.1 Introduction	67
5.2.2 Experiment	68
5.2.3 Discussion	72

Chapter 6

All-Fiber Wavelength-Tunable Continuous-Wave Laser	74
6.1 Introduction	74
6.2 Working Principle	75
6.3 Conclusion	80

Chapter 7

Filamentation Analysis in Large-Mode-Area Fiber Lasers	82
---	-----------

7.1	Introduction	82
7.2	Theoretical Model and Steady-State Solution	84
7.3	Linear Stability Analysis and Filament Gain	87
7.4	Spatio-Temporal Analysis of Filament Gain in Optical Fiber Laser .	89
7.5	Discussion and Conclusion	96
Chapter 8		
	Conclusion	99
	Bibliography	101

List of Tables

4.1	Optimized LDC-200 parameters for terbium fiber cleaving.	38
4.2	Optimized Fitel S183PM parameters for terbium fiber splicing.	43
7.1	Parameters for ytterbium-doped fiber laser calculations.	90

List of Figures

1.1	Typical dimensions of different laser geometries[4].	4
1.2	Double-clad fiber with end pumping and side pumping[2].	5
1.3	Examples of double-clad fiber structures[4].	6
2.1	Faraday rotation in a magneto-optical crystal.	15
2.2	Excited-state splitting in diamagnetic materials.	19
2.3	Excited-state and ground-state splitting in paramagnetic materials.	19
2.4	Comparison of Verdet constant in various rare-earth ions[67].	22
2.5	Annular plane used to calculate magnetic field.	23
2.6	Dimensional configuration of a magnet tube.	24
2.7	Dimensional configuration of a magnet cuboid.	25
2.8	Theoretical (solid) and measured (circle) magnetic density flux distribution B_z along the center axis z of the N35 magnet cuboid, the dashed lines represent the physical ends of the magnet.	26
2.9	Theoretical (solid) and measured (star) magnetic density flux distribution B_z along the center axis z of the N48 magnet tube, the dashed lines represent the physical ends of the magnet.	27
2.10	Contour plot of magnetic field integration to reach 45° polarization rotation as functions of magnet length l and outer radius a_2	28
3.1	Normalized difference between factors Γ and α for single-mode fiber as a function of normalized frequency v	32
3.2	Experimental configuration of the Faraday rotation measurement.	32
3.3	Measured (star) rotation angle and corresponding curve fit (solid) at 1053 nm along the center axis z	33
4.1	Fitel S323A Precision Cleaver	37
4.2	Vytran LDC-200 Cleaver	37

4.3	Endface image of cleaved 65 wt% Tb fiber	39
4.4	Endface interferogram of cleaved 65 wt% Tb fiber	40
4.5	Endface image of mechanically cleaved standard silica fiber	41
4.6	Schematic of fusion splice and mechanical splice	41
4.7	Fitel S183PM fusion splicer	42
4.8	Pictorially explanation of the Arc Mid Offset	43
4.9	Fusion splice images of different fibers: (a) silica-to-silica, (b) Tb-to-silica (good), (c) Tb-to-silica (bad).	45
4.10	Fresnel transmittance as a function of n_2/n_1 . The circle represents the case of Tb and silica fibers.	46
4.11	Coupling efficiency as a function of ω_2/ω_1	47
5.1	Operation of a Faraday isolator illustrated in (a) the forward direction and (b) the backward direction.	49
5.2	Operation of a Faraday mirror illustrated in (a) the forward direction and (b) the backward direction.	50
5.3	Measured rotation angle (circle) and corresponding curve fit (solid) of 56 wt% Tb-doped fiber at a wavelength of 1053 nm as a function of the magnet location along the fiber axis z.	52
5.4	Theoretical rotation angle of 56 wt% Tb-doped fiber at a wavelength of 1053 nm as a function of the N35 magnet location along the fiber axis z.	54
5.5	Measured rotation angle (circle) and corresponding curve fit (solid) of 65 wt% Tb-doped fiber at a wavelength of 1053 nm as a function of the magnet location along the fiber axis z.	55
5.6	Measured (dot) and curve fit (line) Verdet constants of the 54 wt% Tb fiber, 56 wt% Tb fiber, 65 wt% Tb fiber and TGG as a function of Tb^{3+} concentration.	56
5.7	Cross-section structure of the SP1060 fiber.	57
5.8	Cross-section image of the SP1060 fiber.	57
5.9	Measured transmission spectra for two orthogonal polarization directions in a 0.3-m-long SP1060 fiber coiled with a 15 cm diameter.	58
5.10	Longitudinal structure of the CSG (Courtesy of Chiral Photonics).	58

5.11 Measured insertion loss and extinction ratio for CSG (Courtesy of Chiral Photonics).	59
5.12 Experimental configuration of the first all-fiber Faraday isolator. . .	60
5.13 Experimental configuration of the second all-fiber Faraday isolator.	61
5.14 The commercial all-fiber Faraday isolator. Photo courtesy of Ad-Value Photonics.	62
5.15 Experimental configuration of the first all-fiber Faraday mirror. . .	63
5.16 Polarization state measurement of the input and output light of the first Faraday mirror. Triangles and circles are measurement points of the input and output light, respectively. Dashed and solid lines are curve-fits of the input and output light, respectively.	64
5.17 Experimental configuration of the second all-fiber Faraday mirror. .	65
5.18 Polarization state measurement of the input and output light of the second Faraday mirror. Squares and circles are measurement points of the input and output light, respectively. Dashed and solid lines are curve-fits of the input and output light, respectively.	66
5.19 Integration of all-fiber Faraday components.	67
5.20 Sensing principle of the all-fiber Faraday magnet sensor.	69
5.21 Experimental configuration of the all-fiber magnet sensor.	69
5.22 Theoretical (solid) and measured (circle) magnetic density flux distribution B_z along the center axis z . Dashed lines represent the magnet ends, and the dotted line represents B_{av} , the magnetic density flux averaged over a 2-cm length along the axis z	70
5.23 Measured (circle) and calculated (solid) relative transmission of the all-fiber magnet sensor.	71
5.24 Measured (circles) and theoretical (solid) B_{av} as a function of the z axis. The dashed lines represent the end of the magnet.	71
6.1 Configuration of a general wavelength-tunable fiber laser.	75
6.2 Configuration of the all-fiber wavelength-tunable filter.	76
6.3 Rotation of polarization states of different wavelengths in the all-fiber filter.	77
6.4 Experimental configuration to measure the Yb-doped fiber gain spectrum.	78

6.5	Measured ASE spectra of the Yb-doped fiber at different pump currents: 800 mA (solid), 300 mA (dashed), 150 mA (dashed-dot) and 100 mA (dot).	78
6.6	Experimental configuration used to flatten the Yb-doped fiber gain spectrum.	79
6.7	Gain-flattened ASE spectrum of the Yb-doped fiber at 200 mA pump current.	79
6.8	Experimental configuration of the reflective all-fiber wavelength-tunable filter using Tb fiber.	80
6.9	Experimental configuration of the all-fiber wavelength-tunable laser.	80
6.10	Theoretical calculation of the wavelength tuning as a function of the magnet location.	81
7.1	An intense laser beam is focused due to the nonlinear refractive index.	83
7.2	Filamentation is induced by perturbations in a self-focused beam condition.	84
7.3	Infrared image of the top of a broad-area gain region in a semiconductor laser, illustrating the effect of filamentation[156]	84
7.4	The squared second-order bessel solution J_2^2 as a function of fiber radius.	90
7.5	Normalized filament gain versus normalized filament spacing and frequency for $d_{core} = 100 \mu m, P_s = 10 KW$	91
7.6	Normalized filament gain versus normalized filament spacing and frequency for $d_{core} = 100 \mu m, P_s = 10 MW$	91
7.7	(a) Normalized filament spacing and (b) normalized gain as a function of the signal peak power for various core diameters: 20 μm (dotted), 50 μm (dashed-dotted), 100 μm (dashed) and 200 μm (solid) ($f = 10 GHz$).	92
7.8	Gain threshold power [NA=0.2 (dashed), NA=0.1 (dashed-dotted), and NA=0.05 (solid with " + " symbol)] and spatial threshold power [NA=0.2 (solid), NA=0.1 (dotted), and NA=0.05 (dotted with " + " symbol)] as functions of core diameter for three numerical apertures ($f = 10 GHz$).	93

7.9	(a) non-normalized (b) normalized filament gain and (c) normalized filament spacing as a function of the signal peak power for three different cavity length: 0.5 m(solid), 2 m(dotted) and 4m(dashed-dotted)($d_{core} = 100 \mu m$, $f = 10 GHz$).	94
-----	---	----

Foreword

The following individuals are collaborators on the work presented in this thesis: Prof. John Marciante from the Institute of Optics, Univ. of Rochester, Dr. Shibin Jiang from AdValue Photonics, and Dr. Jonathan Zuegel from Laboratory for Laser Energetics, Univ. of Rochester.

In chapter 1, I did the background work, the calculations, and the technical writing. Prof. Marciante provided guidance on technical issues and writing.

In chapter 2, I did the background work, the calculations, the measurements, and the technical writing. Prof. Marciante provided guidance on technical issues and writing.

In chapter 3, I did the calculations, the measurements, and the technical writing. Dr. Jiang provided the terbium-doped fiber. Prof. Marciante provided guidance on technical issues and writing.

In chapter 4, I did the background work, developed the splicing and cleaving processes, and did the technical writing. Dr. Jiang provided the terbium-doped fiber. Prof. Marciante provided guidance on technical issues and writing.

In chapter 5, I fabricated the devices, developed the measurement technique, performed the measurements, analyzed the data, and did the technical writing. Dr. Jiang provided the terbium-doped fibers. Prof. Marciante provided guidance on technical issues and writing. Prof. Marciante and Dr. Zuegel proposed the concept of the all-fiber isolator.

In chapter 6, I developed the concept, performed the calculations and measurements, and did the technical writing. Prof. Marciante provided guidance on technical issues and writing.

In chapter 7, I did the derivation, the calculations, and the technical writing. Prof. Marciante provided guidance on technical issues and writing.

In chapter 8, I wrote the conclusions with guidance from Prof. Marciante.

Chapter 1

Introduction

1.1 Brief Review of High-Power Fiber Lasers

Lasers have become more and more important since their first demonstration by Maiman in 1960[1]. While originally limited to science and engineering fields, people today can find lasers in every corner of human life, for example, in consumer electronics, medical and cosmetic surgery, communications, avionics, and printing. As a subfield of lasers, high-power fiber lasers are attracting more and more attention. Due to the advantages of low weight, small size, robustness, high efficiency, and heat dissipation, high-power fiber lasers will replace chemical lasers, CO_2 lasers, and solid-state lasers in most high-power laser applications. Industrial welding and soldering, and commercial light detection and ranging (LIDAR) are fields in which high-power fiber lasers are mostly being applied[2], [3], [4].

The first fiber laser was demonstrated using neodymium-doped fiber, with side pumping and multi-spatial-mode output, by Snitzer in 1961[5]. In 1973, Stone reported a longitudinally pumped neodymium-doped fiber laser[6]. The longitudinal-pump technique had higher efficiency than the side-pump technique, and the output beam was a single-spatial-mode. In the next several decades, researchers doped different rare-earth ions into optical fiber. The first erbium-doped fiber amplifier (EDFA) was demonstrated by Mears in 1987[7]. The EDFA, together with wavelength-division-multiplexing (WDM), reduced the cost of long-haul communication systems and promoted the boom of telecommunications at the end of the 1990's. Due to its relatively low efficiency, erbium-doped fiber lasers are not

suitable for high-power applications.

Among the rare-earth ions doped in fiber lasers, neodymium (Nd) was the first considered as a dopant for high-power fiber lasers, because Nd-doped lasers have low lasing thresholds due to the four-level energy level structure of Nd^{3+} . Currently, ytterbium (Yb) is primarily used in high-power fiber lasers. Although Yb^{3+} has a quasi-three level energy structure, Yb^{3+} has a lower quantum defect than Nd^{3+} , which means a higher lasing efficiency. There is no ion-quenching effect in Yb-doped fiber lasers, which would reduce the lasing efficiency and induce self-pulsing phenomena.

Although the first Yb-doped fiber laser was demonstrated by Etzel in 1962[8], it was not until the 1990s that high-power Yb-doped fiber lasers began to develop in a dramatic manner. The output power of continuous-wave (CW) high-power Yb-doped fiber lasers have already evolved from the mW level[9] to the multi-kilowatt level[10]. This rapid development is due to the optical communication and semiconductor industry booms at the end of 1990s. Highly transmissive single-mode fiber and advanced doping technologies were enabled by the optical communication industry. The semiconductor industry made high-power laser diodes possible, which are necessary for fiber laser pumping.

Besides optical fiber, another laser geometry, the thin disk, was proposed by Giesen in 1994[11]. Both thin disk and optical fiber have been regarded as potential high-power laser geometries to replace rods in solid-state lasers. The most prominent difference between these two geometries and the rod shape is that they have a relatively small volume of laser-active material. Fig. 1.1. shows the typical dimensions of the these three laser geometries[4]. It is clear that the active volumes of the disk and the fiber are approximately the same and are three orders of magnitude smaller than that of a rod.

The fiber geometry finally stands out from other two competitors because the surface-to-volume-ratio in optical fiber is much higher than that of the other two geometries. This feature is especially important in high-power applications, since the larger this parameter is, the faster the heat generated in the active volume by pump absorption can be dissipated. Heat is one of the major power-limiting factors in high-power fiber lasers and will be discussed in the next section.

Another advantage of the fiber geometry is that it has high pump efficiency and

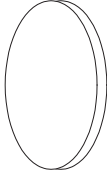

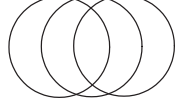
	Disk	Rod	Fiber
Geometry			
Diameter	4 mm	8 mm	12 micron
Length	0.03 cm	10 cm	2000 cm
Volume	0.004 cm^3	5 cm^3	0.004 cm^3
Surface/ Volume	66 cm^{-1}	5 cm^{-1}	2500 cm^{-1}

Figure 1.1: Typical dimensions of different laser geometries[4].

a diffraction-limited output beam. Most high-power fiber lasers use a double-clad structure. Unlike standard communication fiber, double-clad fiber has a three layer structure consisting of a core, an inner cladding, and an outer cladding. The laser beam propagates in the core and the pump light is confined in the inner cladding, as shown in Fig. 1.2 [2]. The pump light can be coupled into the inner cladding from the end or side of double-clad fiber. The double-clad structure is especially suitable for laser diode (LD) pumps which have poor beam quality and can not be coupled into the fiber core with high efficiency.

The pump light injected into the inner cladding passes the fiber core and interacts with doping ions repeatedly as it travels along the fiber. However, some of the pump light (in terms of optical rays) will not interact with the fiber core. Since these helical rays propagate near the inner/outer cladding surface without crossing the fiber core, the pump-absorption efficiency will inevitably be decreased. To solve this problem, researchers proposed various asymmetric inner cladding geometries, as shown in Fig. 1.3 [4]. In such waveguides, pump rays will propagate in an irregular or chaotic manner, thus increasing the overlap between the pump light

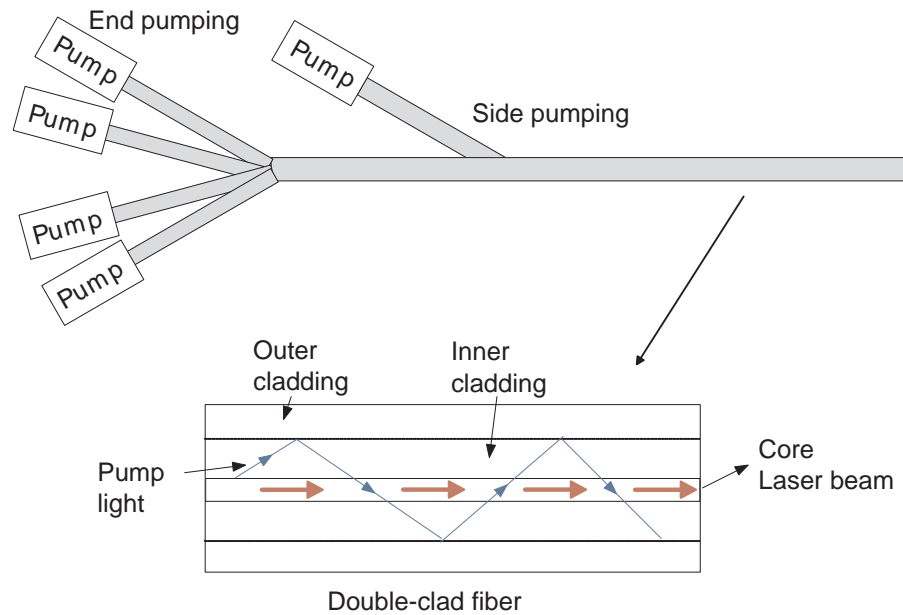


Figure 1.2: Double-clad fiber with end pumping and side pumping[2].

and the core. Snitzer and Po proposed an acentric core and a rectangular inner cladding shape in 1988 and 1989, respectively[12],[13]. Zellmer introduced a D-shaped double-clad fiber in 1995[14], [15]. Muendel proposed a polygon structure in 1996[16]. Digiovanni proposed both star and airhole structures in 1997[17], [18].

There are several popular host materials for optical fiber, such as silica, phosphate glass, and fluoride glass. Since the laser output power is inversely proportional to the loss[19], the fiber host material should have a low intrinsic loss. Owing to the rapid development of the optical communication industry, the loss of standard silica fiber has been reduced to less than 0.2 dB/km at $1.55 \mu\text{m}$. Furthermore, the cost of silica fiber is very low. For these reasons, most high-power fiber lasers use silica fiber. Phosphate glass can be advantageous when a high doping concentration of rare-earth ions is required. However, it has limited use in high-power fiber lasers because the high intrinsic loss will lead to excessive heating and will eventually melt the fiber[20], [21]. Fluoride glass has two advantages over silica. Fluoride glass is transparent in the mid-infrared region, whereas common silica fibers absorb light beyond $2 \mu\text{m}$. Since multi-phonon transitions in fluoride glass are suppressed, the upper-state lifetimes of various rare-earth dopants are greatly increased[22]. However, fluoride glass is expensive and very fragile. The

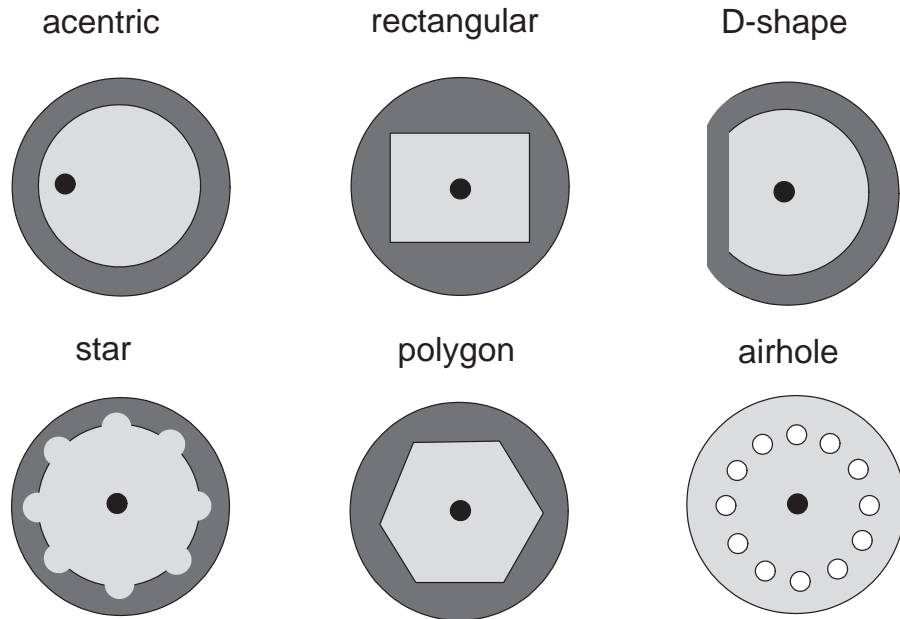


Figure 1.3: Examples of double-clad fiber structures[4].

glass transition temperatures of phosphate and fluoride glass are half that of silica, which makes these two glass generally incompatible with silica fiber.

Many rare-earth ions are used for fiber laser doping, for example praseodymium (Pr), neodymium (Nd), holmium (Ho), erbium (Er), thulium (Tm), and ytterbium (Yb)[23]. The most popular candidate is ytterbium, because it has broad absorption and emission spectra and very small quantum defect. The quantum defect is defined as the energy difference between pump and output photons, which is directly related to the laser efficiency and heating. The quantum defect is only about 6% when a 1035 nm Yb-doped fiber laser is pumped at 975 nm. In contrast, it is 20% for a 1064 nm Nd-doped fiber laser pumped at 808 nm. As a result of small quantum defect, the optical-to-optical pump-conversion efficiency, the electrical-to-optical conversion efficiency, and the wall-plug efficiency can reach 70%, 50% and 30%, respectively.

To avoid nonlinear effects in high-power fiber lasers, people often use large-mode-area (LMA) fibers [24]. Compared with the several- μm mode field diameter in standard single-mode fiber, the mode field diameter in LMA fibers is tens of μm . These large core (or mode area) structures are effective in reducing laser light intensity while maintaining high-power output. Although nonlinear and optical

damage thresholds are increased in LMA fiber, the output beam quality becomes worse, because it is very difficult to control the refractive index difference between the core and inner cladding to less than ~ 0.05 , which is required to maintain single-mode operation in LMA fibers. Fiber coiling and mode selection tapers are popular methods to solve this problem. When multimode fiber is coiled, higher-order modes experience larger loss than the fundamental mode. Therefore, only the fundamental mode can resonate in the laser cavity[25]. When multimode fiber is tapered into single-mode fiber, only the fundamental mode can propagate in the taper region. Higher-order modes are filtered out and the laser can operate in only a single-mode [26].

High-power fiber lasers are a fruitful field of research. There are many new techniques and technologies emerging in this field, such as beam combination, mode-locking, Q-switching, and specialty fibers[27]. Since the objective of this dissertation is not focused on developing high-power fiber lasers themselves, fundamental background will be introduced without covering these specific topics.

1.2 Power-Threshold Limits in High-Power Optical Fiber Lasers

Users of high-power fiber lasers need the output power as large as possible for applications such as industrial welding and soldering, and commercial LIDAR. The phenomenon limiting the scaling of high-power fiber lasers include nonlinear effects [Stimulated Raman Scattering (SRS), Stimulated Brillouin Scattering (SBS), and self-focusing], thermal effects (thermal fracture, melting, and thermal lensing), and optical damage[28], [29]. Beam filamentation induced by self-focusing is a nonlinear effect limiting the output power that will be discussed in detail in Chapter 7.

1.2.1 Nonlinear Effects

1.2.1.1 Stimulated Brillouin Scattering

In an intense laser beam, the electric field of the beam itself may produce acoustic vibrations in the medium via electrostriction[30]. Incident optical photons can be

inelastically scattered by these acoustic vibrations. The scattered photons have lower optical frequency than the incident photons with the energy difference equal to that of the acoustic phonon. The scattered light is shifted around 10 GHz and the Brillouin gain spectrum bandwidth is around 50-100 MHz, determined by the acoustic phonon lifetime. If the laser beam intensity is strong enough, a portion of laser beam will be reflected backwards in the optical fiber due to SBS, reducing the power at the output of the fiber and possibly causing catastrophic damage in the system. The threshold power level[31] for SBS in a passive fiber is estimated as

$$g_B P_{th} L_{eff} / A_{eff} \approx 21, \quad (1.1)$$

where P_{th} is the power threshold, g_B is the Brillouin gain, $A_{eff} = \pi w^2$ is the effective core area, w is the spot size, and L_{eff} is the effective interaction length defined as

$$L_{eff} = [1 - \exp(-\alpha L)] / \alpha. \quad (1.2)$$

α represents fiber loss, and L is the fiber length. If we assume a single-mode silica fiber, for example $\alpha = 0.2 \text{ dB/km}$, $g_B \approx 5 \times 10^{-11} \text{ m/W}$, $L = 1 \text{ m}$ and $w = 5 \text{ }\mu\text{m}$, then $P_{th} \approx 33 \text{ W}$. Clearly, SBS limits the laser power to tens of Watts in a short piece of silica fiber, such as a fiber amplifier.

Many methods have been exploited to increase the power threshold of SBS, such as, transverse variations of the acoustic phase velocity[32], [33] and longitudinal temperature variations[34], [35]. There have also been attempts to reduce the overlap of guided optical and acoustic waves, or to introduce significant propagation loss for the acoustic wave[36], [37]. Increasing the signal bandwidth to decrease the Brillouin gain[38] and using LMA fiber are also effective methods[39].

Although SBS is a limiting factor in high-power applications, it can be used to make Brillouin fiber lasers[40], [41], [42]. Due to the narrow Brillouin gain bandwidth and low resonator loss, Brillouin fiber lasers can have a relatively low pump threshold and a very narrow linewidth. Since the Brillouin shift is dependent on temperature, SBS is used in fiber-optic sensors for sensing temperature and pressure[43], [44].

1.2.1.2 Stimulated Raman Scattering

Similar to SBS, SRS is an inelastic scattering process. Incident photons are scattered by the silica molecules. The scattered photons have lower frequency with the remaining energy absorbed by the silica molecules, which end up in an excited vibrational state. An important difference between SBS and SRS is that optical phonons are involved in SRS whereas acoustic phonons are involved in SBS. The Raman frequency shift (called the Stokes shift) is around 13 THz and the Raman gain spectrum bandwidth is around 10 THz, determined by the optical phonon life time in silica. Different from SBS, SRS can occur in the forward direction. If an intense laser beam is incident in the optical fiber, another light beam with lower frequency will be generated propagating in the same direction. The power will transfer from pump beam (incident beam) to the Stokes beam. The threshold power, P_{th} , is defined as the incident power at which half of the pump power is transferred to the Stokes field at the output end of a fiber of length L , given by[31]

$$g_R P_{th} L_{eff} / A_{eff} \approx 16, \quad (1.3)$$

where g_R is the peak value of the Raman gain. If we assume single-mode silica fiber, for example $\alpha = 0.2 \text{ dB/km}$, $g_R \approx 6 \times 10^{-13} \text{ m/W}$, $L = 1 \text{ m}$ and $w = 5 \text{ }\mu\text{m}$, then $P_{th} \approx 2.7 \text{ kW}$. Although SRS power threshold is larger than that of SBS, it is a limiting factor for broadband light or pulsed light that do not experience significant SBS.

The SRS power threshold can be increased by using LMA fiber, where the light beam intensity is significantly reduced. But the mode-area in the fiber can not be infinitely increased, due to beam quality and thermal effects. Other suppression methods include chirped-pulsed amplification by reducing the pulse peak power by stretching the pulse in the time domain[45], and the use of specialty fiber designs that suppress Raman scattering by attenuating the Raman-shifted wavelength component[46].

Raman scattering is often used in spectroscopy to investigate the vibrational modes of various materials. In optical fiber communication systems, Raman fiber amplifiers can be used to compensate for fiber losses.

1.2.1.3 Self-Focusing

Self-focusing is a nonlinear effect induced by the refractive index change when the optical medium is placed in an intense electromagnetic field[47]. The origin of the self-focusing stems from the optical Kerr effect in which the refractive index, n , depends on the light intensity I , $n = n_0 + n_2 I$, where n_0 and n_2 are the linear and non-linear components of the refractive index. n_2 is positive in most materials. The refractive index becomes larger in the regions where the light intensity is higher, usually in the center of the light beam. A transverse light intensity gradient will induce a transverse refractive index gradient that works as a focusing lens. The light beam is focused by this lens and the peak intensity of the self-focused region increases which strengthens the focusing lens. The focused light beam will eventually induce beam filamentation or optical damage. The threshold of the self-focusing is given by[48]

$$P_{cr} = \alpha \frac{\lambda^2}{4\pi n_0 n_2}, \quad (1.4)$$

where λ is the radiation wavelength in vacuum and α is a constant which depends on the initial spatial distribution of the beam. Assume a Gaussian beam in silica fiber, $\alpha = 1.8962$, $n_0 = 1.45$, $n_2 = 2.6 \times 10^{-20} \text{ m}^2/W$, $\lambda = 1.06 \text{ } \mu\text{m}$, then $P_{cr} = 4.5 \text{ MW}$. Self-focusing needs to be considered in pulsed fiber lasers and will be addressed in Chapter 7.

1.2.2 Thermal Effects

1.2.2.1 Thermal Fracture

Solid-state materials are stronger in compression than in tension, making the surface particularly susceptible to fracture due to the presence of tangential forces. Thermal-induced stresses can make the fiber surface vulnerable to cracks, scratches, and voids. The output power of laser leading to thermal fracture due to tensile-limited stress is derived in Ref. [49],

$$P_{fracture} = \frac{\eta_{laser}}{\eta_{heat}} \frac{4\pi R_m}{1 - \frac{a^2}{2b^2}} L, \quad (1.5)$$

where η_{heat} is the fraction of the absorbed pump power that is converted to heat, η_{laser} is the optical-to-optical conversion efficiency, L is the length of the laser, $R_m = 2460 \text{ W/m}$ is the rupture modulus of the silica glass[50], and a and b are the core and cladding radius, respectively. If we assume $\eta_{laser} = 0.6$, $\eta_{heat} = 0.3$, $L = 1 \text{ m}$, $a = 6 \text{ }\mu\text{m}$, $b = 62.5 \text{ }\mu\text{m}$, then $P_{fracture} = 61 \text{ kW}$. This effect is not likely to be a limiting factor in the near future, although commercial fiber lasers have reached the 10 kW level.

1.2.2.2 Melting

When scaling up the power in conventional fiber lasers, the on-axis core temperature can exceed the melting temperature of fused silica. The output power leading to melting is given by[49]

$$P_{melting} = \frac{\eta_{laser}}{\eta_{heat}} \frac{4\pi k(T_m - T_c)}{1 + \frac{2k}{bh} + 2\ln(\frac{b}{a})} L, \quad (1.6)$$

where $k = 1.38 \text{ W/(m} \cdot \text{K)}$ is the thermal conductivity of silica[51], $T_m = 1983 \text{ K}$ is the melting temperature of silica[51], T_c is the coolant temperature, and h is the convection heat-transfer coefficient (or film coefficient or film conductance). The convection heat-transfer coefficient can vary significantly depending on the cooling mechanism[52]. It may be as low as $1000 \text{ W/(m}^2 \cdot \text{K)}$ for forced airflow cooling or has high as $10,000 \text{ W/(m}^2 \cdot \text{K)}$ for forced liquid flow of the coolant. If we assume $T_c = 300 \text{ K}$, $h = 1000 \text{ W/(m}^2 \cdot \text{K)}$ and other parameters as assumed in Sec. 1.2.2.1, then $P_{melting} = 1.2 \text{ kW}$. CW high-power fiber lasers can operate above this level, provided special attention is paid to system design and thermal management.

1.2.2.3 Thermal Lensing

Thermal lensing is induced by temperature gradients. Due to the cylindrical geometry, the fiber is hotter on the beam axis than in the outer regions, causing a transverse gradient of the refractive index through the thermo-optic effect. This thermal lens can cause aberrations and degrade the output beam quality. The

output power leading to thermal lensing is given by[49]

$$P_{lensing} = \frac{\eta_{laser}}{\eta_{heat}} \frac{\pi k \lambda^2}{2 \frac{dn}{dT} a^2} L, \quad (1.7)$$

where λ is the wavelength of the laser and $dn/dT = 11.8 \times 10^{-6} K^{-1}$ is the change in refractive index with the core temperature in silica[51]. If we assume $\lambda = 1.06 \mu m$, and other parameters are as assumed in Sec. 1.2.2.1, then $P_{lensing} = 11.5 kW$.

1.2.3 Optical Damage

The optical damage mechanism in bulk fused silica is poorly understood. Optical fiber damage is typically observed on the end facet. The bulk optical damage threshold is usually higher than surface optical damage threshold. In practice, the surface optical damage threshold is used for the optical damage threshold. In silica fiber, the surface damage intensity threshold I_{damage} is around $10 W/\mu m^2$ [53]. The output power of fiber laser leading to optical damage can be approximated by

$$P_{damage} = \Gamma^2 I_{damage} \pi a^2, \quad (1.8)$$

where Γ is the core confinement factor and $w = \Gamma a$ is the spot size radius. If we assume $w = 4 \mu m$ for single-mode fiber, then $P_{damage} = 500 W$. To extend performance to kW level, either LMA fibers or core-less fibers need to be used as the endcap to let the light freely expand before hitting the glass-air interface[54].

In practice, the glass-air interface (or fiber facet) is particularly vulnerable to high optical intensity due to dirt and defects. Facet damage is one of the reasons why the maximum power of pigtailed bulk-optic components is limited to a relative low ($< 1 W$) power. To solve this problem, all-fiber devices are required since they have no glass-air interfaces. We will discuss all-fiber Faraday components in detail in Chapters 3 through 5.

1.3 Thesis Objective

The major power-threshold limits of high-power fiber lasers have been briefly reviewed in Section 1.2. Among these limits, facet damage is a bottleneck for scaling

high-power lasers. All-fiber devices are required to solve this problem. In this dissertation, all-fiber Faraday components will be discussed in detail. Faraday components are important devices in high-power laser systems as isolators or Faraday mirrors. Currently, no all-fiber Faraday devices are available because of the small Verdet constant in silica fiber. Terbium is doped into optical fiber to increase the Verdet constant. The concept of an effective Verdet constant is proposed and experimentally verified. All-fiber Faraday isolators and Faraday mirrors are then demonstrated using terbium-doped fiber.

In strong electro-magnetic interference (EMI) environments, all-fiber (instead of electronic) sensors are required to measure magnetic fields. Currently, all-fiber magnet sensor techniques are based on material coatings and can not be mass manufactured. An all-fiber magnet sensor based on Faraday rotation using terbium fiber is demonstrated. This simply structured sensor is low cost and suitable for strong electro-magnetic interference environments.

Wavelength-tunable lasers are required in many optical systems. All-fiber wavelength-tunable lasers are especially desired due to the advantages of small size, low weight, and robustness. However, current all-fiber wavelength-tunable lasers based on fiber Bragg gratings and fiber tapers suffer from the mechanical fatigue and can not be used practically. A new all-fiber wavelength-tunable laser is proposed in this thesis. The tuning filter consists of a fiber polarizer and a fiber Faraday mirror that includes a fiber Faraday rotator and a chirped fiber Bragg grating (CFBG). The CFBG is directly written on the terbium-doped fiber where the Faraday rotation occurs. An all-fiber wavelength-tunable laser can be built by combining a linear laser cavity and this all-fiber tuning filter. Since the electro-magnetic field is used for tuning, high tuning speed can be achieved if a solenoid is used, while keeping the laser mechanically untouched.

The nonlinear effect of self-focusing places another power limit on fiber devices. Self-focusing can lead to beam filamentation and has not been thoroughly investigated. The power-threshold due to filamentation has only been estimated through numerical simulations, which are time-consuming, inconvenient, and prone to inaccuracy. In this dissertation, filamentation in fiber core will be discussed in detail. The power threshold due to filamentation will be derived analytically, which will reveal the parametric dependence of the phenomena.

1.4 Thesis Outline

The remainder of this thesis is organized as follows. Chapter 2 discusses the Faraday effect, magneto-optical materials, and magnet design. In chapter 3, the effective Verdet constant model is proposed and experimentally verified. Chapter 4 discusses the cleaving and splicing of terbium-doped fiber. Chapter 5 presents all-fiber Faraday components, including Faraday isolators, Faraday mirrors, and a magnetic field sensor. Chapter 6 proposes a wavelength-tunable all-fiber laser based on the Faraday effect. Chapter 7 analyzes spatial and temporal characteristics of beam filamentation in LMA fibers due to self-focusing. The conclusions of the thesis is presented in chapter 8.

Chapter 2

Faraday Effect, Magneto-optical Materials, and Magnet Design

2.1 Faraday Effect

The Faraday effect is a magneto-optical phenomenon in which light and a magnetic field interact. When linearly polarized light propagates through a magneto-optical medium that is exposed to a magnetic field aligned parallel to the direction of propagation of light, the plane of polarization (defined by the oscillations of the electric field vector) rotates by an amount proportional to the strength of the applied magnetic field, as shown in Fig.2.1.

The Faraday effect was discovered by Michael Faraday in 1845[55]. It was the

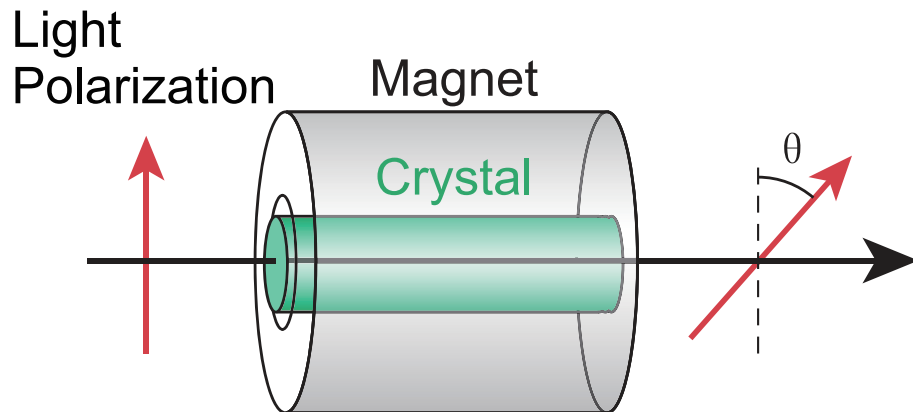


Figure 2.1: Faraday rotation in a magneto-optical crystal.

first time people connected light waves to static magnetic fields, and it led to the unification of electromagnetism by Maxwell in 1865. This effect occurs in most optically transparent dielectric materials (including gases, liquids and solids).

One of the most important properties of the Faraday effect is its nonreciprocal behavior. The rotation angle does not depend on the propagation direction of the light, but rather on the direction of the magnetic field applied parallel to the propagation direction of the light. If light passes a magneto-optical medium twice in opposite directions, the Faraday rotation does not cancel, but rather doubles. Some of important optical components, such as isolators and Faraday mirrors, are based on this property.

The quantum nature of the Faraday effect stems from the Zeeman effect[56], [57]. The ground and excited states split when the optical medium is placed in a magnetic field. This induces an inequality of the refractive indices of left- and right-circularly polarized light, which is known as circular birefringence. Since linearly polarized light can be decomposed into left- and right-circularly polarized light, circular birefringence induces polarization rotation of linear-polarized light when the two circular-polarized components are composed back into linear-polarized light. The rotation angle can be defined as,

$$\theta = \frac{\omega l}{2c}(n_- - n_+), \quad (2.1)$$

where c is the light velocity, l is the sample thickness, n_- and n_+ are the refractive index of the left and right-circularly polarized light with an angular frequency ω . The observed Faraday rotation angle is proportional to the magnetic flux density B and sample thickness l ,

$$\theta = VBl, \quad (2.2)$$

where V is the Verdet constant[58]. A positive Verdet constant corresponds to left-hand-rotation (anticlockwise) when the direction of propagation is parallel to the magnetic field, and a negative Verdet constant corresponds to right-hand-rotation (clockwise) when the direction of propagation is parallel to the magnetic field.

The expressions of n_- and n_+ can be obtained from Maxwell equations[59]. Substituting these expressions into Eq. 2.1. and comparing with Eq. 2.2, the

Verdet constant is,

$$V = \frac{Ne^3}{2nm^2} \frac{1}{c\epsilon_0} \frac{\omega^2}{(\omega^2 - \omega_0^2)^2}, \quad (2.3)$$

where N is the number of charge carriers per unit volume, e is the charge, m is the mass, n is refractive index of the material, ω_0 is the electronic resonance frequency, and ω is the the operating frequency.

Equation 2.3 is a general equation for all magneto-optic materials. Based on the concept of the newly discovered electron, Becquerel[60] found a simplified expression for diamagnetic materials. Although it did not include the idea of quantized energy states introduced by Planck in 1900 or the concept of light quanta developed by Einstein in 1905, it provides a simple solution for understanding the Faraday effect, and yields quantitative predictions for the Verdet constant that are very close to the measured values.

The Zeeman shift in a small magnetic field can be expressed as

$$\omega_Z = \pm \frac{eB}{2m}, \quad (2.4)$$

where B is the magnetic flux density. The \pm signs refer to the orientation of the magnetic field relative to the orbital angular momentum of the electron. The indices n_- and n_+ can be related to the Zeeman effect with the assumption that the frequency dependence of the refractive index is related to the frequency of the electron in the atom.

$$n_+ = n + \omega_Z \frac{dn}{d\omega} \quad (2.5)$$

$$n_- = n - \omega_Z \frac{dn}{d\omega}, \quad (2.6)$$

where n is the refractive index with no magnetic field. Combining equations 2.5 and 2.6 yields

$$n_- - n_+ = -2\omega_Z \frac{dn}{d\omega}. \quad (2.7)$$

When expressed in the wavelength domain,

$$n_- - n_+ = \frac{\omega_Z}{\pi c} \lambda^2 \frac{dn}{d\lambda}. \quad (2.8)$$

Combining Eqs. 2.1, 2.2, 2.4, and 2.8, the Verdet constant is

$$V = \frac{e}{2mc} \lambda \frac{dn}{d\lambda}. \quad (2.9)$$

Eq. 2.9. only holds for diamagnetic materials. When dealing with paramagnetic materials or materials with both diamagnetic and paramagnetic species, the contribution from paramagnetic ions must be accounted for. In these materials, the Verdet constant is proportional to [61], [62], [63]

$$V \propto \nu^2 \left[\sum_i \frac{A_i}{(\omega_i^2 - \omega^2)^2} + \sum_i \sum_j \frac{B_{ij}}{(\omega_i^2 - \omega^2)(\omega_j^2 - \omega^2)} \right] = \nu^2 (D + P) \quad (2.10)$$

where ν is the frequency of the light, D is the diamagnetic component that can be calculated from the Becquerel equation (Eq. 2.10), and P is the paramagnetic component that can be calculated from quantum mechanical considerations of the ground- and excited-state splitting [64].

2.2 Magneto-Optical Materials

The magneto-optical effect can occur in gases, liquids, and solids. Because solids exhibit much stronger magneto-optical effect than gases and liquids, solids are typically used for Faraday components. Solids can be classified into the classes of diamagnetic, paramagnetic, ferromagnetic, antiferromagnetic, and ferrimagnetic materials.

Ferromagnetic, antiferromagnetic, and ferrimagnetic materials are much more complex than the other two classes. These materials exhibit a saturation effect, which leads to a nonlinear magneto-optical response. Although the magneto-optical effects in these materials are usually much stronger than the other two classes, the large optical absorption limits their use in optical applications. Therefore, they will not be covered here (detailed information can be found in ref. [65]).

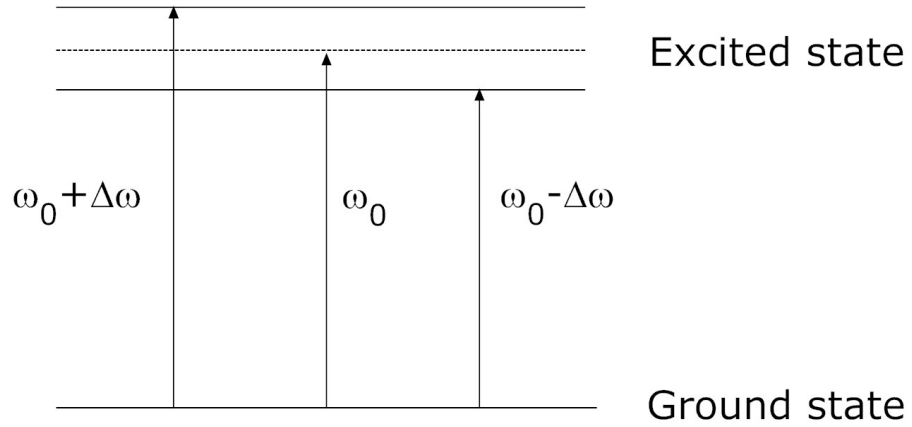


Figure 2.2: Excited-state splitting in diamagnetic materials.

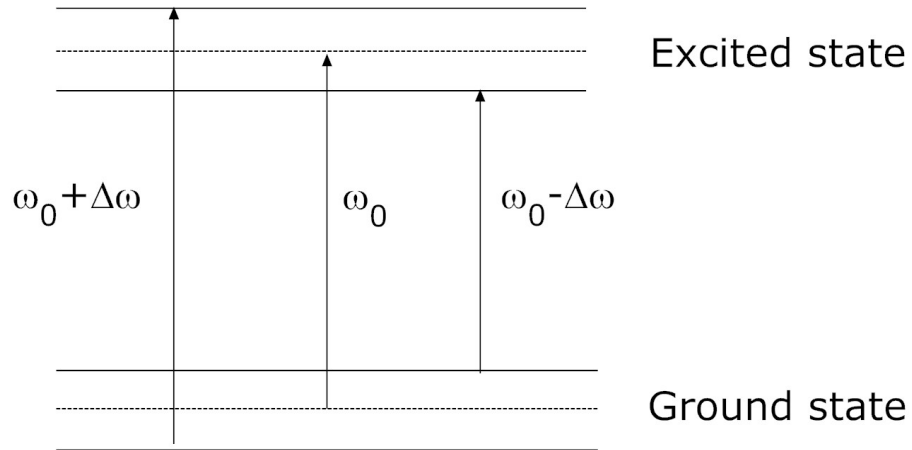


Figure 2.3: Excited-state and ground-state splitting in paramagnetic materials.

2.2.1 Diamagnetic Materials

In diamagnetic materials, there is no macroscopic or microscopic magnetization in the absence of an applied magnetic field. The Faraday effect arises from the excited-state splitting of this material, as shown in Fig. 2.2. The splitting is proportional to the applied magnetic field. Although more accurate formulas have been developed[62], the Verdet constant of diamagnetic materials can still be expressed with a classical atomic model[59], the Becquerel formula[60] as shown in Eq. 2.9, which is simple and has been verified experimentally[62].

The Verdet constant of diamagnetic material is weakly dependent on the temperature. But in some certain applications, such as accurate sensors, this temper-

ature dependence will be a significant problem. The temperature dependence can be written as

$$\frac{1}{(VL)_0} \frac{d(VL)}{dT} = \frac{1}{V_0} \frac{dV}{dT} + \alpha, \quad (2.11)$$

where $\alpha = (dL/dT)/L$ is the thermal expansion coefficient. In most fused silica glass, $(1/(VL)_0)(d(VL)/dT) = 0.69 \times 10^{-4} /K$, $\alpha = 0.55 \times 10^{-6} /K$. Diamagnetic materials generally exhibit a weaker Faraday effect than other classes, however, this drawback can be outweighed by the linear response of the Faraday effect to the applied magnetic field and the relative stability with respect to temperature.

2.2.2 Paramagnetic Materials

In paramagnetic materials, some or all of the individual atoms possess magnetic dipole moments. In the absence of an applied magnetic field, these moments are randomly aligned and there is no macroscopic magnetization. When an external magnetic field is applied, these dipole moments align, which is equivalent to the ground state splitting shown in Fig. 2.3. If there is no thermal energy, all the ground state ions will be in the lower of the two levels. At room temperature, some of the ions will be populated into the upper level of the ground state as well.

The Verdet constant of paramagnetic materials is usually expressed as the sum of a diamagnetic component V_{dia} and a paramagnetic component V_{par} ,

$$V = V_{dia} + V_{par}. \quad (2.12)$$

V_{dia} is normally positive and related to the excited state splitting. On the contrary, V_{par} is normally negative and related to the ground state splitting. If the concentration of paramagnetic ions is relatively large, V_{par} dominates. Otherwise, the materials will exhibit diamagnetic properties of diamagnetic materials.

The Faraday effect in paramagnetic materials can not be derived using classical analysis, but a quantum mechanical solution is available[66].

$$V_{par} \propto \frac{\nu^2 \chi_{par}}{g} \sum_{a,b} \left(\frac{C_{ab}}{\nu^2 - \nu_{ab}^2} \right), \quad (2.13)$$

where ν is the frequency of light, C_{ab} is a transition probability, ν_{ab} is the frequency

associated with the transition. The paramagnetic susceptibility χ_{par} is given by [61],

$$\chi_{par} = \frac{Ng^2[J(J+1)]\mu_B^2}{3kT}, \quad (2.14)$$

where N is the number of atoms or ions per unit volume, g is the Lande factor, J is the spin orbit quantum number, k is the Boltzmann constant, and T is the absolute temperature. The temperature term in the paramagnetic susceptibility is a reflection of the temperature dependence of the Verdet constant.

Among all paramagnetic materials, rare-earth ions are the most important class. Most materials with high Verdet constant are rare-earth doped glasses or crystals. In these glass systems, rare-earth ions and their concentration are the primary factors governing the magnitude of the paramagnetic part of the Verdet constant. The host glass is not important in defining the Verdet constant. Among all rare-earth ions, terbium, dysprosium, and praseodymium are most effective in generating a large magneto-optical effect. Samarium, gadolinium, erbium, and ytterbium have relatively small Verdet constant, as shown in Fig. 2.4 [67].

Due to its large Verdet constant and small absorption coefficient in the visible and IR regions, terbium is the most popular rare-earth ion for practical Faraday components. For example, FR-5 glass from Hoya, is about 50 wt% terbium-doped borosilicate glass, with a Verdet constant of -20.6 rad/(Tm) at 1064 nm [68], [65]. The terbium gallium garnet (TGG) crystal, which is widely used in bulk-optics based Faraday components, has a Verdet constant of -38 rad/(Tm) at 1064 nm [68].

2.3 Magnet Design

There are four common classes of permanent magnet materials: neodymium iron boron (NdFeB or NIB), samarium cobalt (SmCo), aluminium nickel cobalt (Alnico), and ceramic (or Ferrite). Among these materials, NdFeB is the most powerful magnetic material. This type of rare-earth magnet is made from an alloy of neodymium, iron, and boron to form the $Nd_2Fe_{14}B$ tetragonal crystalline structure.

Neodymium magnets are graded by the material they are made of. As a general rule, the higher the grade (the number following the 'N'), the stronger the magnet.

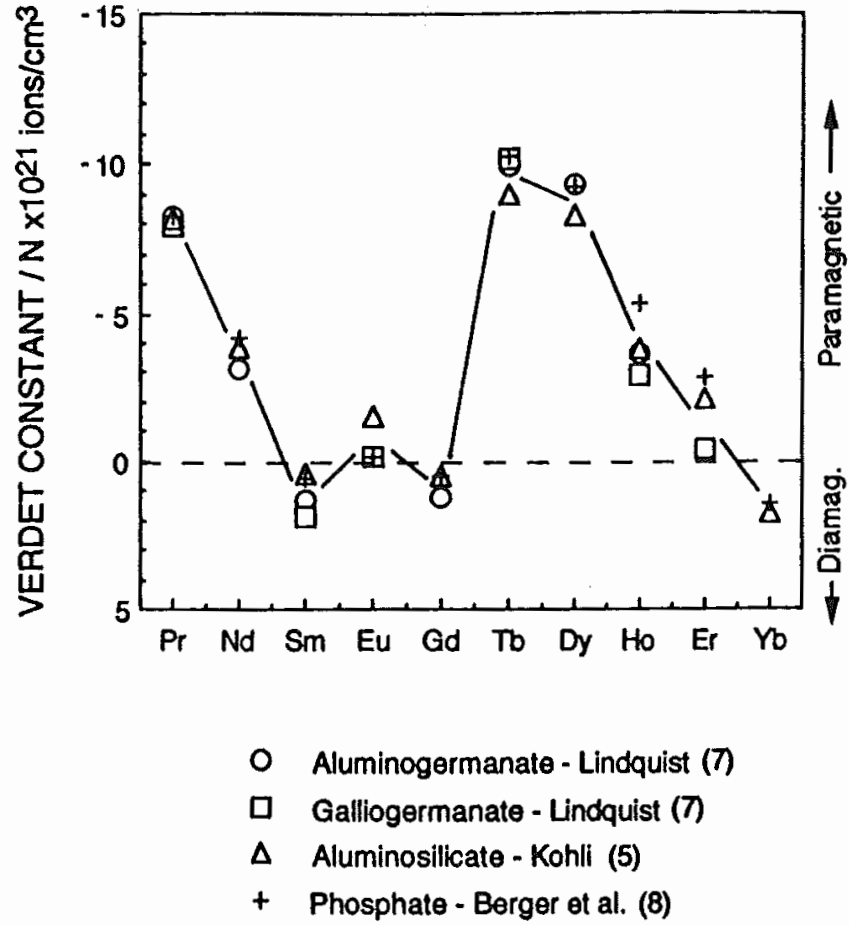


Figure 2.4: Comparison of Verdet constant in various rare-earth ions[67].

The highest grade of neodymium magnet currently available is N52. Another important parameter of magnets is the "residual flux density" B_r (polarization). B_r is the magnetic induction remaining in a saturated magnetic material after the magnetizing field has been removed.

The field of a magnet can be calculated from its poles[69]. Assuming there is a uniform distribution of poles on the ends of the magnet, the pole strength of area ΔA on a surface whose normal makes an angle ϕ to the direction of the polarization B_r , is $B_r \Delta A \cos(\phi)$. If $\phi = 0$, the potential at distance, r , from this small element is

$$\psi = B_r \Delta A / (4\pi\mu_0 r). \quad (2.15)$$

The magnetic field on the axis of a uniformly magnetized cylindrical magnet

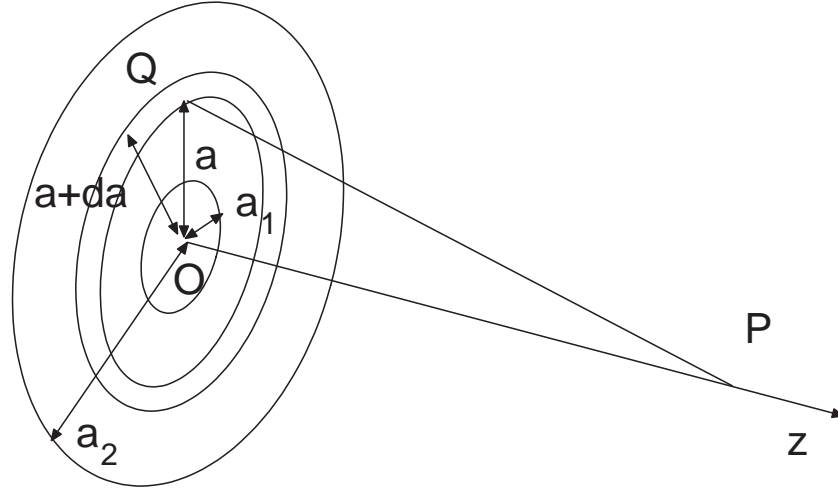


Figure 2.5: Annular plane used to calculate magnetic field.

tube can be treated as if produced by two annular surfaces at its ends. The surface pole method will be illustrated by calculating the field produced by placing the annular surface along a normal passing through its center.

As shown in Fig. 2.5, the surface is annular, with inner and outer radii, a_1 and a_2 , respectively, and center point, O . The line from point O to point P , OP , is normal to the annular plane, and this direction is defined as z . Consider an element of area ΔA around a point Q on the surface at radial distance, a , from O . The pole strength on ΔA is $B_r \Delta A$ and the distance OP is r , which follows the relation $r = (z^2 + a^2)^{1/2}$. This relation holds for any point on an annular area between radii a and $a+da$, so it is convenient to take such an area as our element of area as $\Delta A = 2\pi a da$. The potential at point P contributed by this annular area is

$$d\psi = \frac{2\pi a B_r da}{(a^2 + z^2)^{1/2} 4\pi \mu_0}. \quad (2.16)$$

Integrating the potential contribution from the whole surface yields

$$\begin{aligned} \psi(z) &= \frac{B_r}{2\mu_0} \int_{a_1}^{a_2} \frac{a da}{(a^2 + z^2)^{1/2}} = \frac{B_r}{2\mu_0} (a^2 + z^2)^{1/2} \Big|_{a_1}^{a_2}, \\ &= \frac{B_r}{2\mu_0} [(a_2^2 + z^2)^{1/2} - (a_1^2 + z^2)^{1/2}]. \end{aligned} \quad (2.17)$$

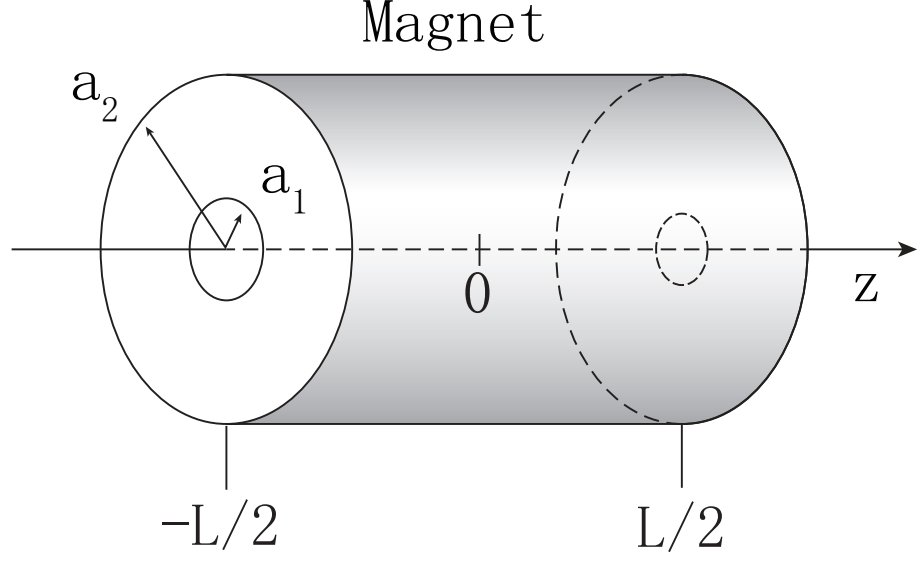


Figure 2.6: Dimensional configuration of a magnet tube.

By symmetry, the magnetic field, H , has no components perpendicular to z and the value of H in the direction of z is

$$H_z(z) = -\frac{d\psi}{dz} = -\frac{B_r}{2\mu_0} \left[\frac{z}{(a_2^2 + z^2)^{1/2}} - \frac{z}{(a_1^2 + z^2)^{1/2}} \right], \quad (2.18)$$

The magnetic flux density B can be obtained by multiplying μ_0 with H ,

$$B_z(z) = \mu_0 H_z = \frac{B_r}{2} \left[\frac{z}{(a_1^2 + z^2)^{1/2}} - \frac{z}{(a_2^2 + z^2)^{1/2}} \right]. \quad (2.19)$$

Eq. 2.19 is the solution in the case of one magnetic pole. If the magnet is a cylindrical tube as shown in Fig. 2.6, the magnetic field is the sum of the two poles.

$$B_z(z) = \frac{B_r}{2} \left\{ \frac{z + l/2}{[a_1^2 + (z + l/2)^2]^{1/2}} - \frac{z + l/2}{[a_2^2 + (z + l/2)^2]^{1/2}} \right. \\ \left. - \frac{z - l/2}{[a_1^2 + (z - l/2)^2]^{1/2}} + \frac{z - l/2}{[a_2^2 + (z - l/2)^2]^{1/2}} \right\}, \quad (2.20)$$

where two poles are located in the planes $z=-L/2$ and $z=L/2$ respectively, L is the length of the magnet tube. The magnetic field integration inside the magnet tube

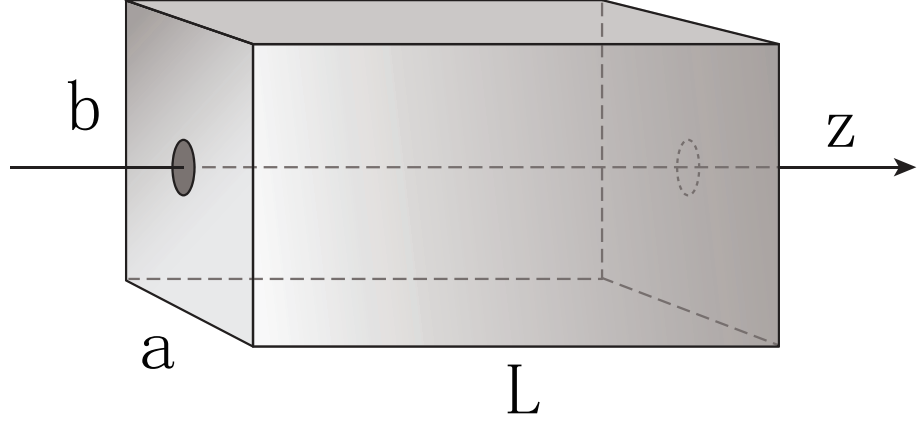


Figure 2.7: Dimensional configuration of a magnet cuboid.

along the z direction can be calculated from Eq. 2.20,

$$\int_{-l/2}^{l/2} B_z(z) dz = B_r \{ (a_1 - a_2) - [(a_1^2 + l^2)^{1/2} - (a_2^2 + l^2)^{1/2}] \}. \quad (2.21)$$

The magnetic field derivation of a magnet cuboid is much more complicated and only the solution is given here[69]

$$B_z(z) = \frac{B_r}{\pi} \left[\tan^{-1} \left(\frac{ab}{2(z + l/2)[4(z + l/2)^2 + a^2 + b^2]^{1/2}} \right) - \tan^{-1} \left(\frac{ab}{2(z - l/2)[4(z - l/2)^2 + a^2 + b^2]^{1/2}} \right) \right], \quad (2.22)$$

where a , b and L are the height, width and length of the cuboid, respectively. Its dimensional configuration is shown in Fig. 2.7. The magnetic field integration along the z direction can only be calculated numerically.

Two magnets have been used in this dissertation. One is an N35 NdFeB magnet cuboid, with dimension $15 \times 15 \times 25 \text{ cm}^3$ and a residual flux density $B_r = 0.95 \text{ T}$. There is a small hole in the center of this magnet for the optical fiber to go through and its effect on magnetic field can be neglected. Fig. 2.8 shows the calculated B_z for the N35 magnet used in the experiments along with the measured magnetic field outside the magnet. The physical ends of the magnet are also shown for reference. The magnetic field, measured only outside the magnet because the magnetic field probe size is larger than the hole diameter, agrees very well with the theoretical

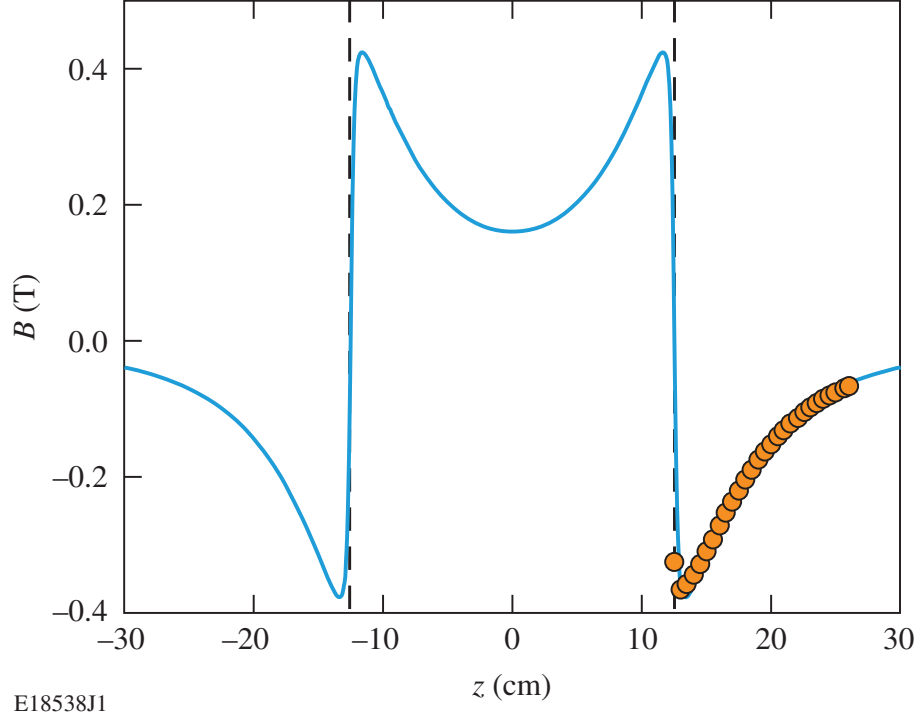


Figure 2.8: Theoretical (solid) and measured (circle) magnetic density flux distribution B_z along the center axis z of the N35 magnet cuboid, the dashed lines represent the physical ends of the magnet.

curve calculated from Eq. 2.22.

The other magnet is an N48 NdFeB magnet tube, which is 4-cm long with inner and outer diameters of 5 mm and 6 cm respectively. The residual flux density is $B_r = 1.35 T$. Fig. 2.9 shows the calculated and measured magnetic fields for the N48 magnet used in the experiments. Again, the measured magnetic field agrees very well with the theoretical curve calculated from Eq. 2.20.

Eq. 2.2 is only valid for a uniform magnetic field. If the magnetic field is not uniform, like the cases shown in Figs. 2.8 and 2.9, a modified equation should be used

$$\theta = V \int_l B(z) dz \quad (2.23)$$

where $\int_l B(z) dz$ is the magnetic density flux integration along the length L . For a given Verdet constant, the rotation angle θ depends on the integration $\int_l B(z) dz$.

Since most Faraday applications require 45° polarization rotation, the size of a magnet tube can be calculated from Eq. 2.21 for various Verdet constants.

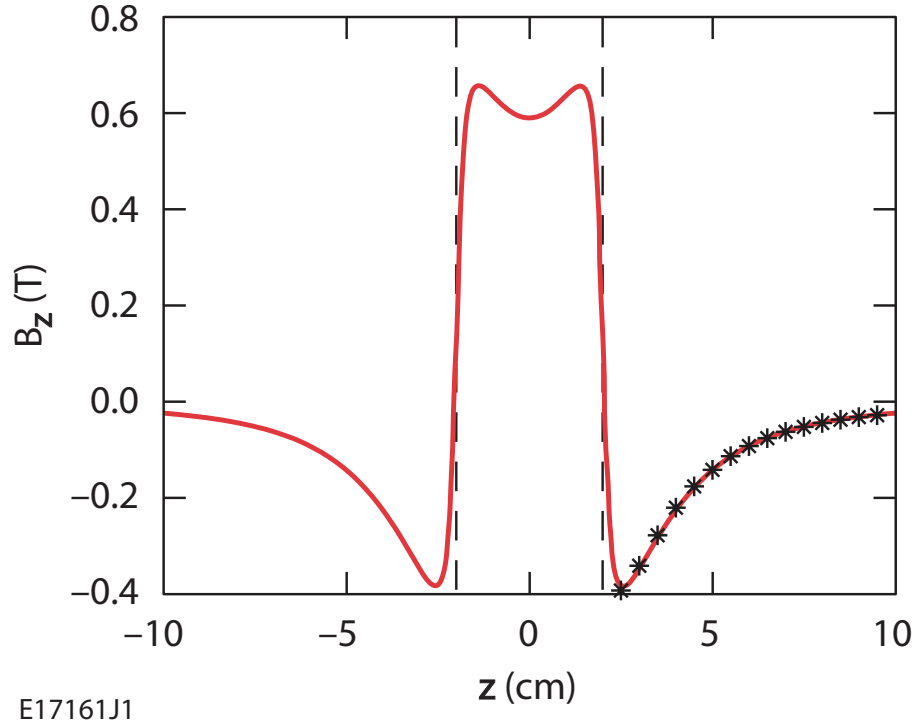


Figure 2.9: Theoretical (solid) and measured (star) magnetic density flux distribution B_z along the center axis z of the N48 magnet tube, the dashed lines represent the physical ends of the magnet.

Fig. 2.10 shows the contour plot of magnetic field integration inside the magnet tube as functions of magnet length, L , and outer radius, a_2 . $B_r = 1.35 T$ and $a_1 = 2.5 mm$ are assumed in the calculation. The contour lines represent the Verdet constant required to reach 45° polarization rotation level when integrated along the path through the magnet via Eq. 2.23. The figure shows that for a fixed Verdet constant, the length and outer radius can not be arbitrarily increased to reach the required 45° polarization rotation angle. There is an optimized value for L and a_2 to reach 45° rotation while maintaining a small magnet size. The larger the Verdet constant, the smaller the required magnet size. If $V=32 \text{ rad}/(\text{Tm})$, the optimized length and outer radius for a magnet tube are 3.2 cm and 3.3 cm respectively.

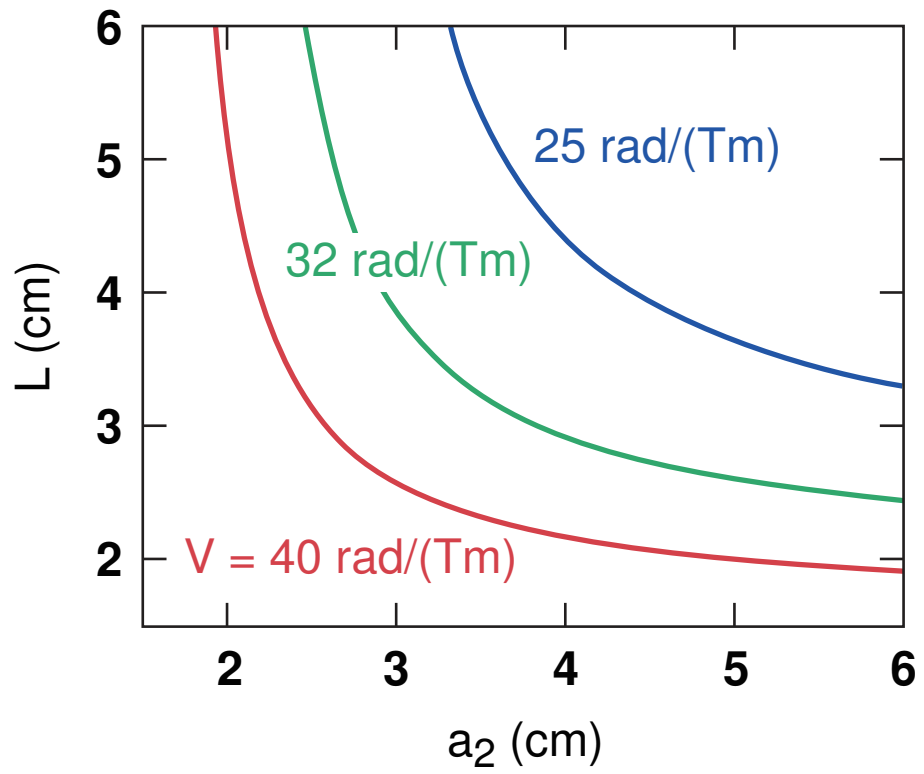


Figure 2.10: Contour plot of magnetic field integration to reach 45° polarization rotation as functions of magnet length l and outer radius a_2 .

Chapter 3

Effective Verdet Constant Model for Optical Fiber

3.1 Introduction

Faraday rotators are widely used in optical isolators, circulators, Faraday mirrors, and magnetic/current field sensors. Traditional Faraday rotators are based on bulk optics, which require optical coupling for use with fiber optic systems. All-fiber Faraday rotation components are highly desirable, particularly for high-power fiber laser systems, where fiber termination and small free space beams place restrictions on how much power can be transported through such components.

Several standard silica fiber Faraday rotators have been reported[70], [71], [72], [73], but are relatively impractical due to long fiber lengths. The bottleneck to realize all-fiber Faraday rotators is the small Verdet constant in silica which is only about 1.1 rad/(Tm) at 1064 nm, compared with -40 rad/(Tm) in TGG crystals often used in bulk optics[74], [75]. This low Verdet constant will require long fiber lengths in order to achieve the desired rotation. For example, if the magnetic field is 0.2 T, the silica fiber length required for a 45-degree rotation is around 4 meters. Due to the magnetic field distribution of the magnet, this long fiber can not be coiled, making such a system impractical.

To overcome this limitation, Shiraishi[76] reported the fabrication of a high Verdet constant (21 times greater than silica fiber) optical fiber using Hoya FR-5 (terbium borosilicate) glass, where both the core and the cladding were doped

with terbium. Ballato and Snitzer[77] also reported the fabrication of a 54 wt% terbium-doped optical fiber, measuring the Verdet constant on bulk samples to be 20 times higher than that of silica fiber.

Doping with high-Verdet-constant materials, such as terbium, can be an effective way to increase the total Verdet constant in optical fiber. However, the Verdet constant experienced by the optical field is different from the material Verdet constants in the core and cladding when they are made of different materials. The experiments described above did not measure or predict this effect. In this section, the first experimental proof of the effective Verdet constant model is presented. The effective Verdet constant in a phosphate fiber which is terbium-doped in the core only is measured. The experimental results agree well with the theory and describe how the effective Verdet constant differs from the value measured from the bulk samples.

3.2 Theory

The Verdet constant experienced by light in an optical fiber is different from that in bulk glass, where it is uniform everywhere. In an optical fiber, the core and cladding can have different Verdet constants since they can be made of different materials. Only a portion of the guided mode exists in the core of the fiber waveguide. Thus, the effective Verdet constant V_{eff} , is defined as the Verdet constant experienced by the optical mode in the fiber,

$$V_{eff} = V_{core}\Gamma + V_{clad}(1 - \Gamma), \quad (3.1)$$

where V_{core} and V_{clad} are the Verdet constants in the core and cladding respectively, and the confinement factor $\Gamma = P_{core}/P_{tot}$ represents the ratio of the power contained in the core, P_{core} , to total power, P_{tot} . The confinement factor, Γ , can be calculated directly by assuming that the fundamental mode profile is Gaussian, $\Gamma = 1 - exp(-2/\xi^2)$. The ratio of beam spot size to fiber radius, ξ , is usually approximated by

$$\xi \simeq 0.65 + 1.619v^{-3/2} + 2.879v^{-6}, \quad (3.2)$$

which is accurate to within 1% for $1.2 \leq v \leq 2.4$, where v is the normalized frequency (or V-number)[78]. Equation 3.1 for the effective Verdet constant has a straightforward physical meaning: the Verdet constant includes two parts contributing from the core and the cladding, weighted by the mode overlap in each region.

In recent theoretical work[79], the rotation of an optical field in a fiber was derived using Maxwell's equations with a magnetic field applied along the axial direction of the fiber. An empirical equation was used to approximate the propagation constant. Using these results, one can derive the effective Verdet constant directly from the circular birefringence of the propagation constant.

$$\theta = [\alpha n_c V_{core} + (1 - \alpha)n_{cl}V_{clad}]BL/[\gamma n_c^2 + (1 - \gamma)n_{cl}^2]^{1/2}. \quad (3.3)$$

Eq. 3.3 was given by Yoshino[79], where $\alpha = 1.306 - 1.138/v$, $\gamma = 1.306 - (2.277v - 0.992)/v^2$, n_c and n_{cl} are the refractive index for core and cladding, respectively. In most single-mode fibers, the difference between n_c and n_{cl} is very small. Assuming $n_c \approx n_{cl}$, Eq. 3.3 can be simplified to $\theta = [\alpha V_{core} + (1 - \alpha)V_{clad}]BL$. An effective Verdet constant can be derived as $V_{eff}^{Yoshino} = V_{core}\alpha + V_{clad}(1 - \alpha)$, although no physical meaning is given in Ref. [79]. Fig. 3.1 shows the relative difference $\Delta = (\alpha - \Gamma)/\alpha$ between factors Γ and α as a function of v . In the region $2 < v < 2.4$, where most single-mode fibers are designed, Δ is less than 4%. Considering that both models use empirical equations for their derivation, such difference is reasonable. Although not indicated in [79], α should have the same physical meaning as Γ , representing the light confinement in the core. This suggests that Equation 3.1 can be derived via rigorous electromagnetic calculations.

3.3 Experiment

The phosphate optical fiber used in these experiments was fabricated at *NP Photonics*[80]. It is 25-wt%-terbium doped in the single-mode core (N.A.=0.147) and 6-wt%-lanthanum doped in the cladding to provide the appropriate core N.A. The core and cladding diameters are 4.5 μm and 120 μm respectively, and the propagation loss is 0.12 dB/cm at 980 nm. The Verdet constant is measured at 1053

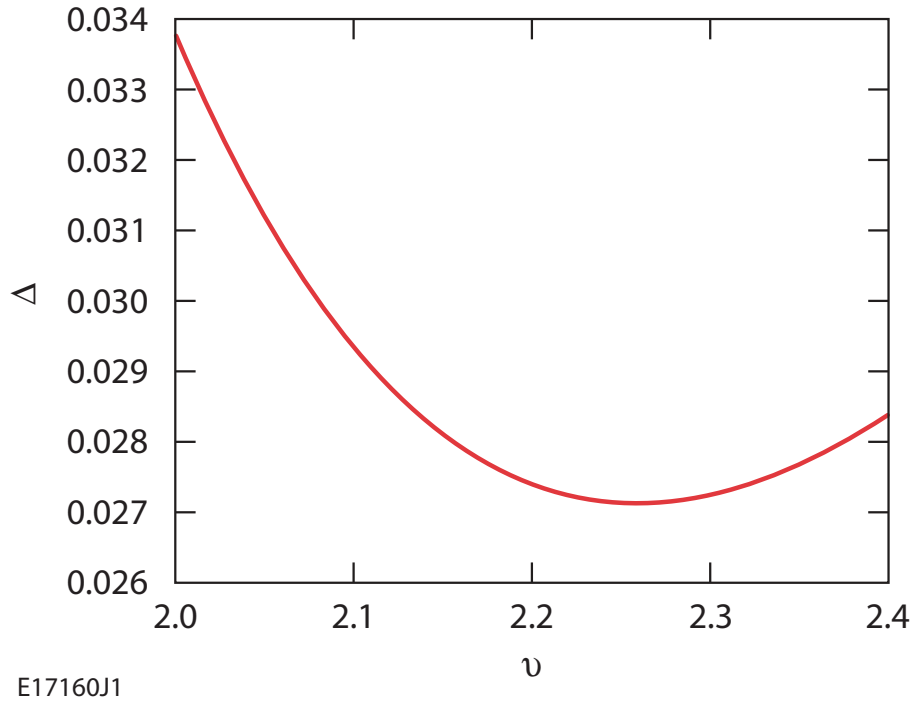


Figure 3.1: Normalized difference between factors Γ and α for single-mode fiber as a function of normalized frequency ν .

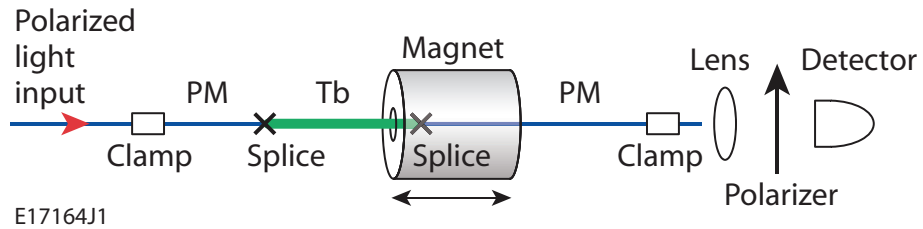


Figure 3.2: Experimental configuration of the Faraday rotation measurement.

nm and room temperature using the experimental configuration shown in Fig. 3.2. A 4-cm section of Tb-doped phosphate fiber, spliced between two polarization-maintaining (PM) fibers, goes through the N48 magnet tube described in Sec. 2.3. Linearly polarized 1053-nm light is launched into the fiber, and the polarization direction of the output light is monitored. As the magnet is translated along the fiber, the magnetic field imposed on the Tb fiber is changed. By measuring the rotation angle as a function of position of the magnet on the fiber axis, V_{eff} can be extracted provided the magnetic field is known.

As shown in Fig. 2.9, the magnetic field has different directions inside and

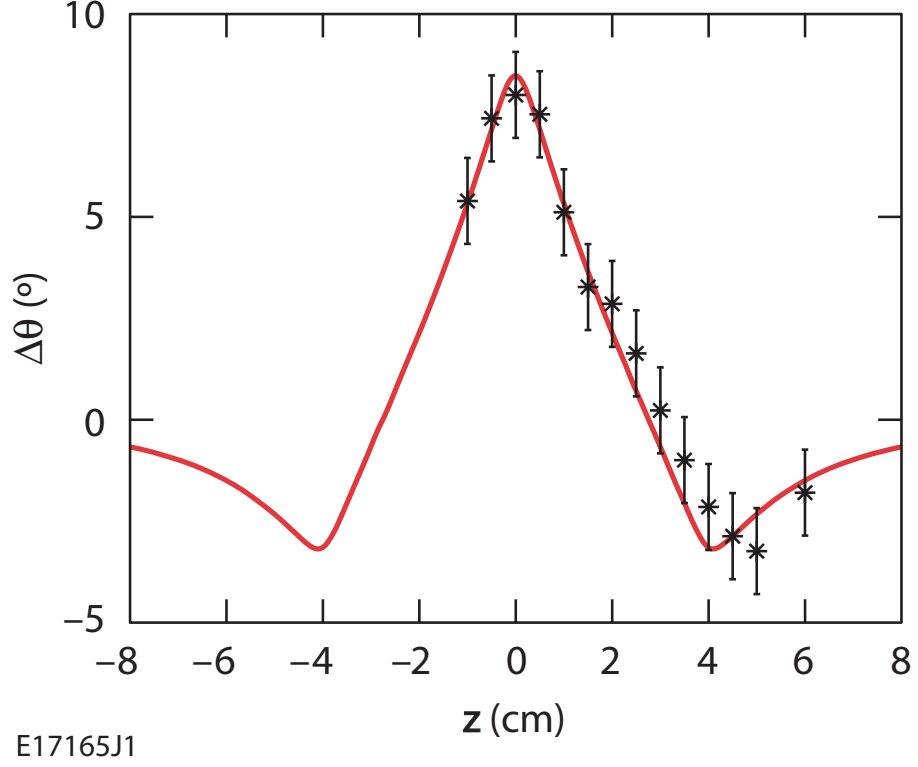


Figure 3.3: Measured (star) rotation angle and corresponding curve fit (solid) at 1053 nm along the center axis z .

outside the magnet, such that the total integrated field along the z axis is zero, i.e. $\int_{-\infty}^{+\infty} B_z dz = 0$. This means that if a piece of fiber with axially uniform V_{eff} goes through the magnet, the rotation angles inside and outside the magnet counteract each other and the total rotation angle is zero. If the fiber consists of i different sections of length L_i , the total rotation angle, $\Delta\theta_{tot}$, can be written as a sum of the rotation in each section $\Delta\theta_i$, given by

$$\Delta\theta_{tot} = \sum_i \Delta\theta_i = \sum_i V_{eff}^i \int_{L_i} B_z dz, \quad (3.4)$$

where V_{eff}^i and $\int_{L_i} B_z dz$ are the effective Verdet constant and the line integral of the magnetic field in each section, respectively. For the experimental configuration shown in Fig. 3.2, Eq. 3.4 can be simplified as

$$\Delta\theta_{tot} = V_{eff}^{Tb} \int_{Tb} B_z dz + V_{eff}^{PM} \int_{PM} B_z dz, \quad (3.5)$$

where the two terms represent the Verdet constant of and the integration over the Tb-doped and PM fibers respectively. V_{eff}^{PM} can be neglected in our experiment because the large linear birefringence in PM fiber effectively suppresses Faraday rotation.

In the experiment, the magnet is axially translated in 5 mm steps. At each step, the direction of the major polarization axis is measured; the power is measured as the polarizer in front of the detector is rotated, and the polarization direction is extracted by fitting this data to a cosine-squared function. Figure. 3.3. shows the measured rotation angle and the corresponding curve fit at 1053 nm along the central axis. The error in the measured angle is primarily caused by air flow and it is determined to be 1 degree by a polarization stability measurement. In the polarization stability measurement, same polarization direction was measured for several times and the root mean squared deviation was taken as error. The curve fit is obtained by adjusting V_{eff}^{Tb} , yielding a measured Verdet constant of $V_{measure} = -6.2 \pm 0.4 \text{ rad}/(Tm)$. This value is 6 times higher than that of the silica and demonstrates the potential for compact all-fiber Faraday rotators.

3.4 Discussion

The bulk value of the Tb-doped core is calculated from ref. [77] to be $V_{core} = -9.3 \text{ rad}/(Tm)$, assuming a linear dependence on the terbium-ion concentration. Since no Verdet constant data is available for the lanthanum phosphate glass in the near infrared region, the value is approximated based on two observations. First, the Verdet constant dispersion curve of the lanthanum phosphate glass is roughly 0.8 rad/(Tm) higher than the one for SiO_2 in the visible region[68], [65]. Assuming a similar trend in the near infrared region, the Verdet constant of the lanthanum phosphate glass should be 0.8 rad/(Tm) larger than that of the SiO_2 . Second, the rare-earth element present in the host material is the dominating factor in determining the Verdet constant. For example, the Verdet constant of the terbium aluminosilicate is similar to that of the terbium phosphate with similar concentration[65]. Therefore, the Verdet constant of the crystal LaF_3 measured at 1064 nm[68] should be also similar to that of lanthanum phosphate. These two observations independently lead to a value of $V_{clad} = 1.8 \text{ rad}/(Tm)$. Using

these values for the core and cladding Verdet constants, the theoretical models predict $V_{eff} = -6.0 \text{ rad}/(Tm)$ and $V_{eff}^{Yoshino} = -6.3 \text{ rad}/(Tm)$, the difference between the models is due to the approximations contained in each. They both agree well the experimental result, which differs substantially from the bulk core value $-9.3 \text{ rad}/(Tm)$ due to the mode confinement properties as described above. This measurement validates the theory of the effective Verdet constant.

Several methods can be used to increase the effective Verdet constant for compact all-fiber Faraday rotators. For example, the same high-Verdet-constant material can be doped in both the core and the cladding. In this case, the V_{eff} will be equal to the material Verdet constant. If the high-Verdet-constant material is doped only in the core, the N.A. and the core diameter can be increased (while maintaining the V-number less than 2.405) to confine more light in the core, therefore increasing V_{eff} . Other rare-earth elements besides terbium can also be doped. For example, praseodymium and dysprosium also have Verdet constants much higher than that of silica. The optical loss in the Tb-doped fiber could be decreased significantly with improvement in the fabrication process.

In conclusion, the first experimental validation of the effective Verdet constant theory is reported. The effective Verdet constant of light propagation in a fiber includes contributions from the materials in both the core and the cladding. It is measured in a 25 wt% terbium-core-doped phosphate fiber to be $-6.2 \pm 0.4 \text{ rad}/(Tm)$ at 1053 nm, which is 6 times larger than silica fiber. The result agrees well with Faraday rotation theory in optical fibers. This work has been published in reference [81].

Chapter 4

Cleaving and Splicing of Terbium Fiber

Because the mechanical and thermal properties of the highly terbium-doped fiber are much different than those of standard silica fiber, the fiber cleaver and the fusion splicer, which are designed for silica fiber, do not work for a terbium-doped fiber. This is a technical bottleneck to making all-fiber components. Customized programs for the electronic cleaver and the fusion splicer solved this problem in the lab.

4.1 Cleaving

A controlled break that is intended to create a smooth and flat fiber endface is called fiber cleave. The endface is usually perpendicular to the fiber longitudinal axis. If they are not perpendicular, it is called an angled cleave. When cleaving an optical fiber, a microscopic fracture ("nick") is introduced into the fiber with a cleaving tool. The cleaving tool usually has a sharp blade of some hard material such as diamond, sapphire, or tungsten carbide. Tension is introduced into the fiber as the nick is made, or immediately afterward, causing the fracture to propagate in the direction perpendicular to the fiber axis, resulting in an endface that is of sufficient flatness for fiber splicing.

There are two kinds of fiber cleavers. A mechanical cleaver first clamps the fiber. Then a diamond wheel or blade scribes the fiber. After that, a transverse

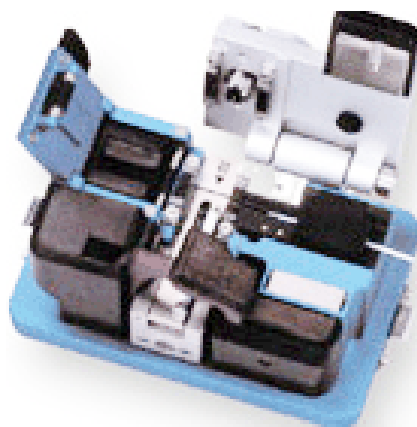


Figure 4.1: Fitel S323A Precision Cleaver

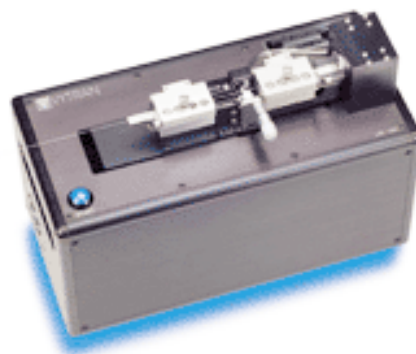


Figure 4.2: Vytran LDC-200 Cleaver

force is applied and the fiber yields a clean break at the scribe. This kind of cleaver is very popular in cleaving standard silica fiber due to its compact size and easy operation. For example, the Fitel S323A Precision Cleaver used in the lab is shown in Fig. 4.1. Such a cleaver can not be used to cleave terbium fiber because it is optimized for standard silica fiber and can not be modified.

The second kind of cleaver uses a "scratch and pull" technique. When cleaving, the fiber is scribed perpendicular to the fiber by a small blade while tension is being applied to the fiber. A clean break will then occur at the scribe point. Fig. 4.2 shows one such cleaver, the Vytran LDC-200 Cleaver which is used in our experiments. Although this kind of cleaver is more complex than the mechanical

Table 4.1: Optimized LDC-200 parameters for terbium fiber cleaving.

Parameter	Value
Cleave Tension	310 g
Tension Velocity	15 steps/sec
Rotation Angle	0 degree
Pre-Cleave Advance	660 steps
Cleave Osc. Counter	100
Cleave Forward Steps	21
Cleave Backward Steps	21
Scribe Delay	1 ms

cleaver, it is automated and fully programmable, which allows the unit to be modified for cleaving various types of fiber. Table 4.1 shows the parameters that are optimized for the LDC-200 to cleave the 65 wt% Tb fiber. The "Cleave Tension" is the load, in grams, applied axially to the fiber prior to initiating the scribe process. The optimal tension for cleaving is dependent upon the cross-sectional area of the fiber and the material properties of the glass. The "Tension Velocity" is the velocity of the tension motor, in steps per second, which applies the load to the fiber prior to initiating the scribe process. The "Rotation Angle" is the angle, in degrees, applied to the fiber prior to initiating the tension process. Zero degrees corresponds to a perpendicular cleave; angle cleaves can be intentionally made by using a non-zero Rotation Angle. The "Pre-Cleave Advance" is the distance, in steps, that the cleave blade moves forward prior to initiating the scribe process. It is dependent on the fiber parameters and must be reduced as the fiber diameter increases. The "Cleave Oscillation Counter" is the maximum number of oscillations that the cleave blade will make during the scribe process. For this particular cleave, the scribe process consists of multiple nicks of the fiber. The "Cleave Forward Steps" is the distance, in steps, that the cleave blade moves forward (toward the fiber) during each oscillation of the blade. The "Cleave Backward Steps" is the distance, in steps, that the cleave blade moves back (away from the fiber) during each oscillation of the blade. The "Scribe Delay" is the delay, in milliseconds, between each oscillation of the blade[82].

Figure 4.3 shows a microscope image of the end face of the 65 wt% Tb fiber after cleaving using the optimized parameters shown in Table 4.1. The dark crack at the upper right edge of the fiber is where the scribe blade nicked the fiber.

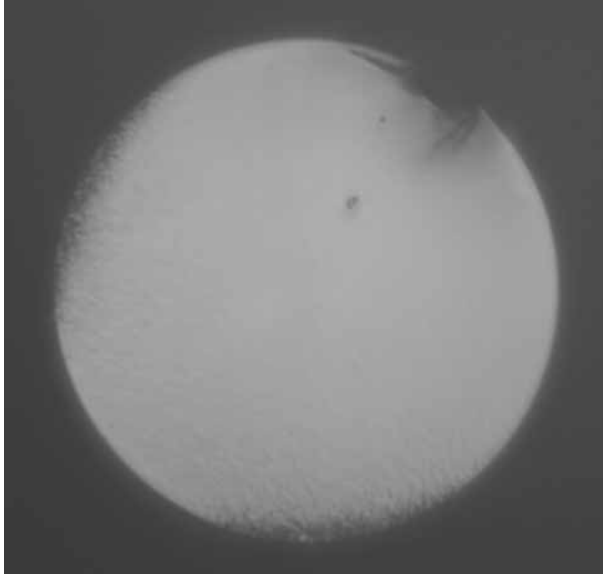


Figure 4.3: Endface image of cleaved 65 wt% Tb fiber

The "fuzzy" features at the left and bottom of the fiber are imperfections in the material interface. They appear because the propagation velocity of the fracture is too high. Either of these types of features can be independently eliminated at the price of increasing the other, which then reach more towards the center of the fiber. In practice, the cleave parameters are optimized to balance the two types of features, which keeps them confined to the edges of the fiber and minimizes their impact in the fusion splicing process.

Figure 4.4 shows an interferometric image of the same fiber cleave. Apart from the deformation caused by the impact of the scribe, the fiber endface is very flat (to within a few waves).

The cleave shown in Figures 4.3 and 4.4 is very repeatable and is in fact exceptionally clean compared to the type of cleave resulting from a mechanical cleaver, shown in Figure 4.5. Note that this image was taken using standard silica fiber as cleaving the terbium-doped fiber with this cleaver resulted in a catastrophic cleave. Although the fuzzy features are not present, the surface exhibits significant structure, particularly across the fiber core, which is located in the center of the fiber. However, even such a coarse mechanical cleave is acceptable for fusion splicing due to the nature of the process, described in the next section.

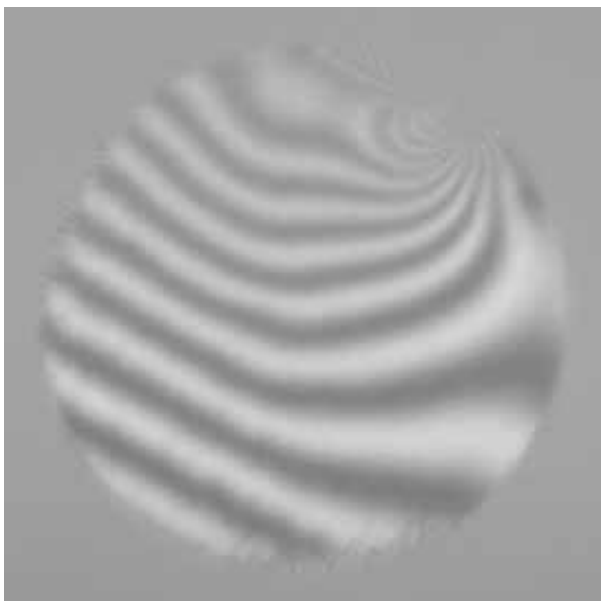


Figure 4.4: Endface interferogram of cleaved 65 wt% Tb fiber

4.2 Splicing

Fiber optic splicing is the act of joining two optical fibers together end-to-end. Light is coupled from one fiber to another fiber through such a junction. There are two kinds of splices: mechanical splice and fusion splice, as depicted in Fig. 4.6. In a mechanical splice, two fibers are aligned together through an alignment sleeve, which is normally filled with index matching gel to fill the space between the slightly separated fiber ends. Mechanical splices are temporary splices. If a permanent splice is required, a fusion splice should be used. In a fusion splice, two fibers are welded together using localized heat, as depicted in Fig. 4.6. The heat can be provided by an electric arc, a laser, a gas flame, or a tungsten filament through which current is passed. Both mechanical and fusion splices need well cleaved fiber ends to produce low-loss junctions.

Since the primary reason for all-fiber Faraday components is high-power applications, all material interfaces should be eliminated. Therefore, mechanical splices are not acceptable. In the experiments, the Fitel S183PM fusion splicer was used to fusion splice terbium fiber and silica fiber, as shown in Fig. 4.7. This splicer is fully automated and electronically controlled, with dozens of pre-set programs optimized for splicing various types of fiber together. However, the programs are

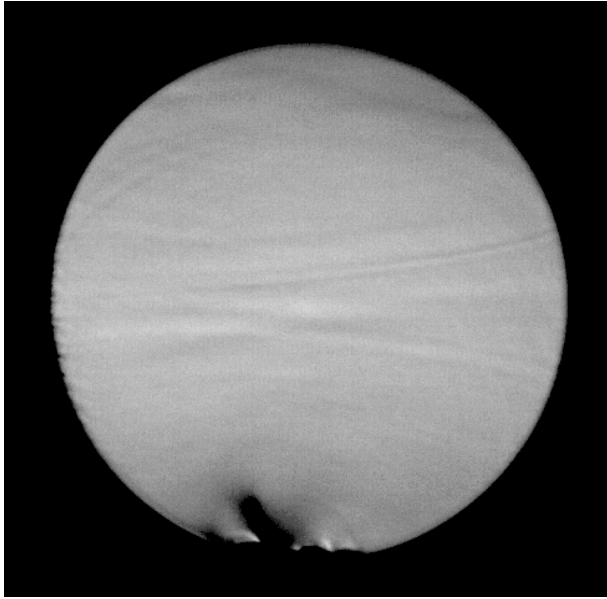


Figure 4.5: Endface image of mechanically cleaved standard silica fiber

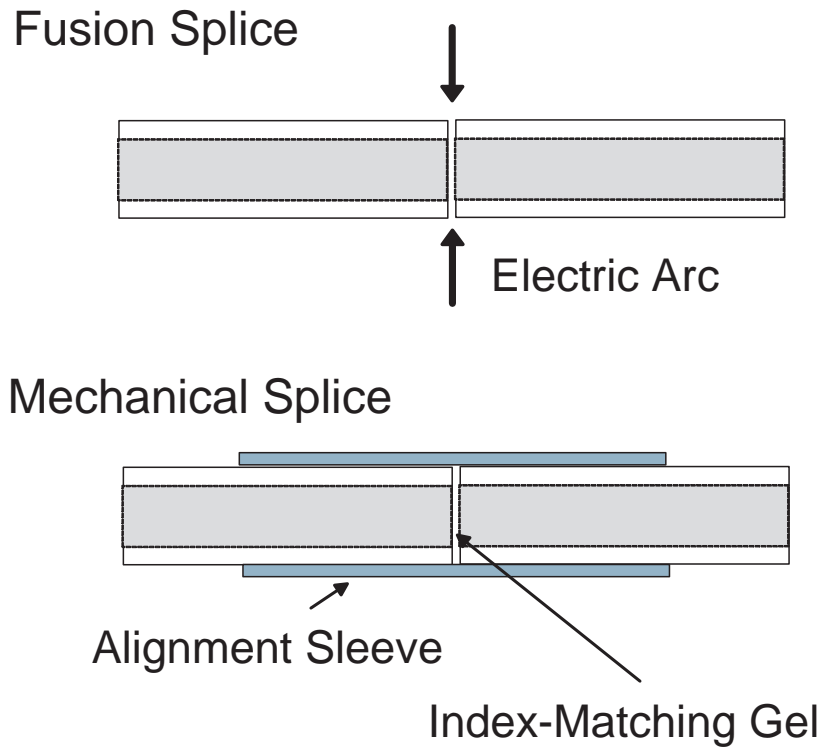


Figure 4.6: Schematic of fusion splice and mechanical splice



Figure 4.7: Fitel S183PM fusion splicer

optimized for silica fiber, primarily for telecommunication varieties (SMF-28, dispersion shifted fiber, erbium-doped fiber, etc.). Since the terbium fiber has a substantially different melting point than standard silica, none of the pre-set programs could produce a clean fusion splice. The problem of fusion splicing in our experiments was exacerbated by the fact that we needed to fuse the terbium fiber with silica fiber. By offsetting the location of the arc from the joint of the two fibers, the temperature profile can, in principle, be made to be hotter in the silica fiber than that of the terbium fiber, which allows each of the fibers to be brought close to their respective melting points. This was difficult to achieve in practice since the thermal profile generated by the arc could not be controlled.

The generalized fusion-splicing program for the S183PM contains three electric arcs. The preliminary arc is a low power arc designed to clean debris off the fiber ends that was not removed by prior ultrasonic chemical cleaning. The next two arcs are defined by their starting power, ending power, and duration. Table 4.2 shows the optimized Fitel S183PM parameters for 65 wt% Tb fiber splicing to silica fiber. The "Arc Power Compens." corrects the arc power based on the axis offset of the fibers. The "Pre-fuse Time" is the time between the fibers first butting and the arc starting. The "Z Push Distance" is amount that the fibers are pushed

Table 4.2: Optimized Fitel S183PM parameters for terbium fiber splicing.

Parameter	Value
Cleaning Arc Power Offset	-90
Cleaning Time	20 ms
Arc Pow. 1st Start	50
Arc Pow. 1st End	0
1st Arc Duration	100 ms
Arc Pow. 2nd Start	0
Arc Pow. 2nd End	0
2nd Arc Duration	0 ms
Arc Power Compens.	-125
Pre-fuse Time	160 ms
Z Push Distance	10 μm
Z Pull Distance	0 μm
Z Pull Start Time	0 ms
Arc Mid Offset	-200 μm
Gap	20 μm

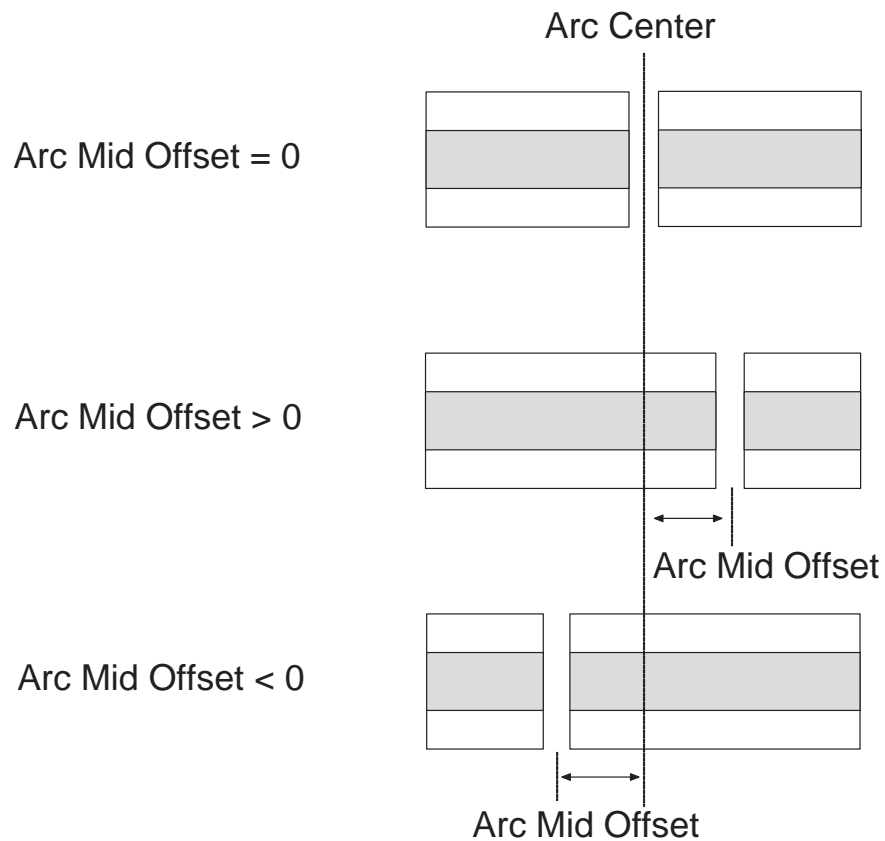


Figure 4.8: Pictorially explanation of the Arc Mid Offset

together during the first arc. The "Z Pull Distance" allows the fibers to be pulled during the process at a time defined by the "Z Pull Start Time". The "Arc Mid Offset" is the offset between fiber joint and the arc center. Fig. 4.8 pictorially explains the Arc Mid Offset. If the offset is greater than zero, the arc center is shifted to the left of the fiber joint. If offset is less than zero, the arc center is shifted to the right of the fiber joint. In this way, it is possible to offset the splice point from the arc center to achieve an optimized temperature profile using this parameter. The "Gap" is the gap spacing between fibers for final position tuning (core or clad alignment) before splicing[83].

Figure 4.9 shows fusion splice images using the S183PM splicer. Since the fusion splicer is designed for silica fiber splices, silica fiber can be perfectly fusion spliced with silica fiber, as shown in Fig. 4.9(a); there is no observed defect. Fig. 4.9(b) shows a good Tb-fiber to silica-fiber splice. There is a noticeable defect between Tb and silica fibers because the temperature at the splice point is the optimized temperature for the Tb fiber to melt. Since the melting temperature of silica fiber is higher than this temperature, the silica fiber does not reach the melting point. In the Z-Push process, the melted Tb fiber is adhered to the hot silica fiber. Because it is not a complete fusion splice, a small defect appears between the Tb fiber and the silica fiber. If the Tb fiber gets too hot, the core will diffuse into the cladding, as shown in Fig. 4.9(c). Since there is no waveguide in that section of fiber, the loss will be more than 1 dB.

4.3 Coupling Efficiency

Even with a perfect material splice, there can still be loss due to misalignment occurring in the splice process, and differences in fiber core diameters. The coupling efficiency, η , between two fibers is given by[84]

$$\eta = \frac{|t \int_0^\infty \psi_1 \psi_2 \exp(i\varphi) \rho d\rho|^2}{\int_0^\infty \psi_1^2 \rho d\rho \int_0^\infty \psi_2^2 \rho d\rho}, \quad (4.1)$$

where ψ_1 and ψ_2 are the optical fields in the two fibers. $\rho = \sqrt{x^2 + y^2}$ is the radial coordinate. φ is the phase error between two fiber modes. t is the Fresnel transmission factor. If the fibers are perfectly cleaved and spliced, there should be

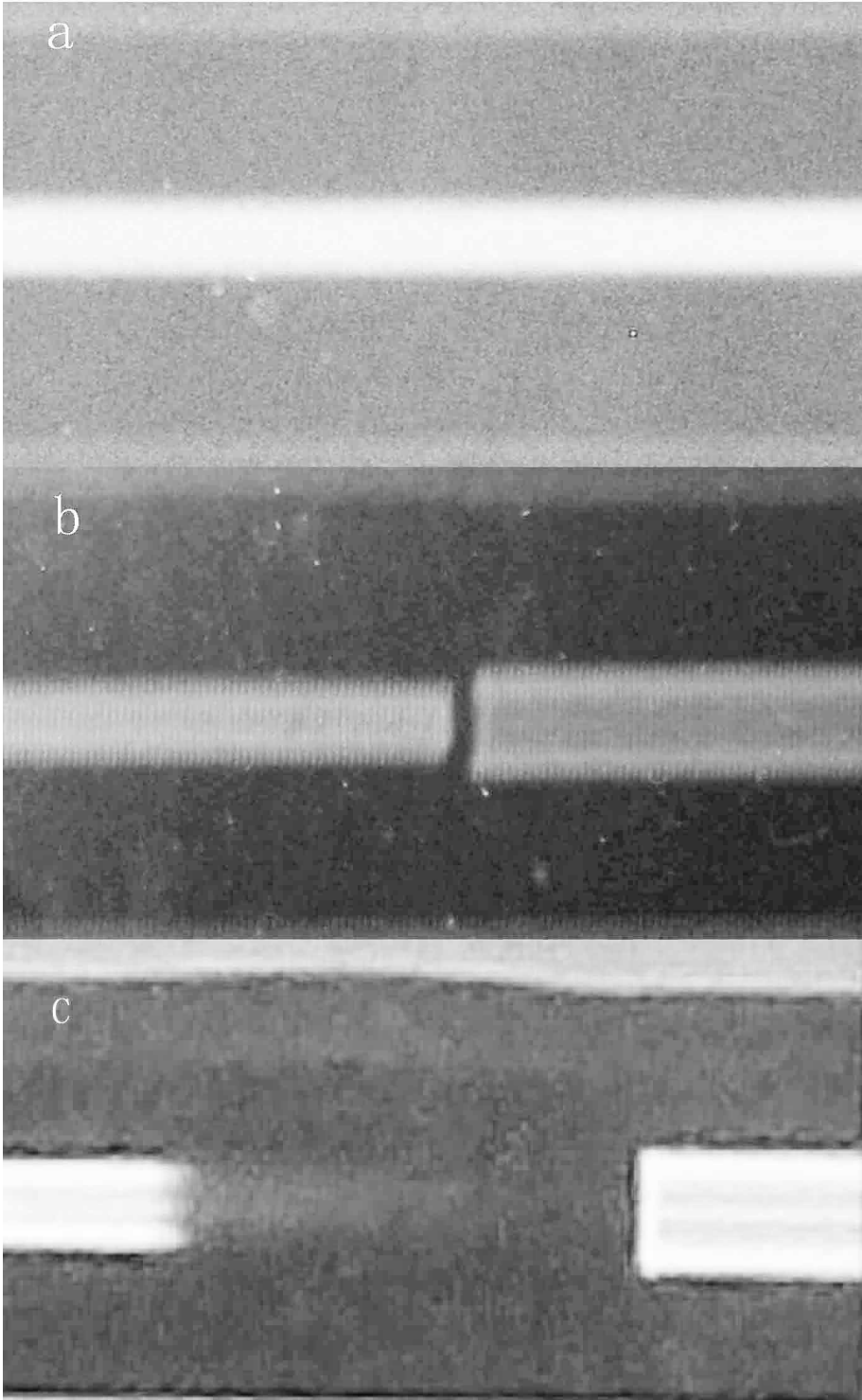


Figure 4.9: Fusion splice images of different fibers: (a) silica-to-silica, (b) Tb-to-silica (good), (c) Tb-to-silica (bad).

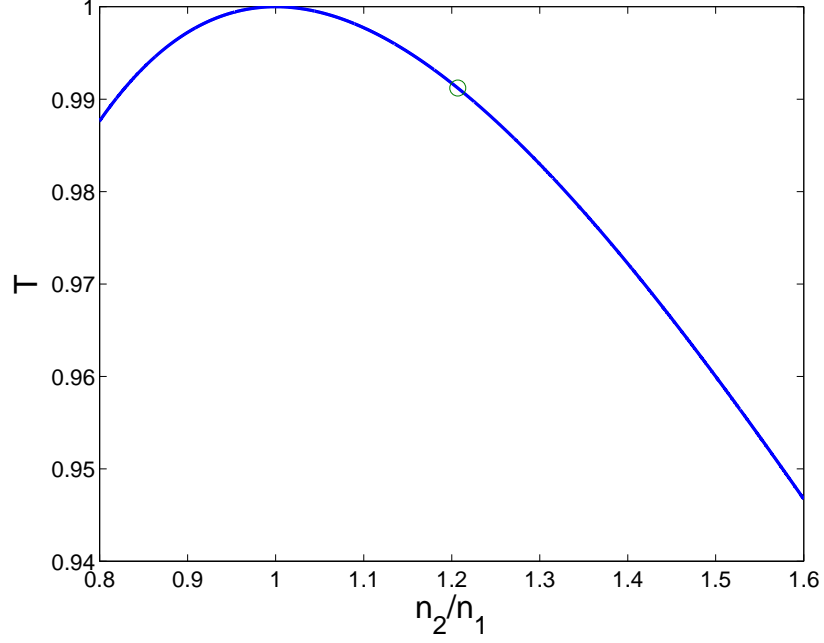


Figure 4.10: Fresnel transmittance as a function of n_2/n_1 . The circle represents the case of Tb and silica fibers.

no phase error ($\varphi = 0$) between the two optical fields. Substituting the Gaussian approximations $\psi_1 = \exp(-\rho^2/\omega_1^2)$ and $\psi_2 = \exp(-\rho^2/\omega_2^2)$ into Eq. 4.1, η can be simplified as

$$\eta = \frac{4T(\omega_2/\omega_1)^2}{[1 + (\omega_2/\omega_1)^2]^2}, \quad (4.2)$$

where ω_1 and ω_2 are the mode field radii in the two fibers, and $T = t^2 = \frac{4(n_2/n_1)}{[1+(n_2/n_1)]^2}$ is the Fresnel transmittance in the case of normal incidence. Fig. 4.10 shows the Fresnel transmittance as a function of n_2/n_1 . If the values of n_1 and n_2 are relatively close, T is around 1. For example, in the case of silica and terbium fibers, $n_1 = 1.45$, $n_2 = 1.75$, and $T = 0.99 \approx 1$. Therefore, the Fresnel transmittance T can be assumed to be unity in most cases, even when splicing dissimilar fibers.

Fig. 4.11 shows the coupling efficiency as a function of ω_2/ω_1 . η is equal to 1 only in the case of $\omega_1 = \omega_2$. Assuming $\omega_1 = 5.1 \mu\text{m}$ and $\omega_2 = 3.2 \mu\text{m}$, η is calculated to be 0.8, corresponding to 0.97 dB loss. Although both of these mode field radii correspond to single-mode waveguides, it is clearly not a sufficient condition to guarantee low loss coupling.

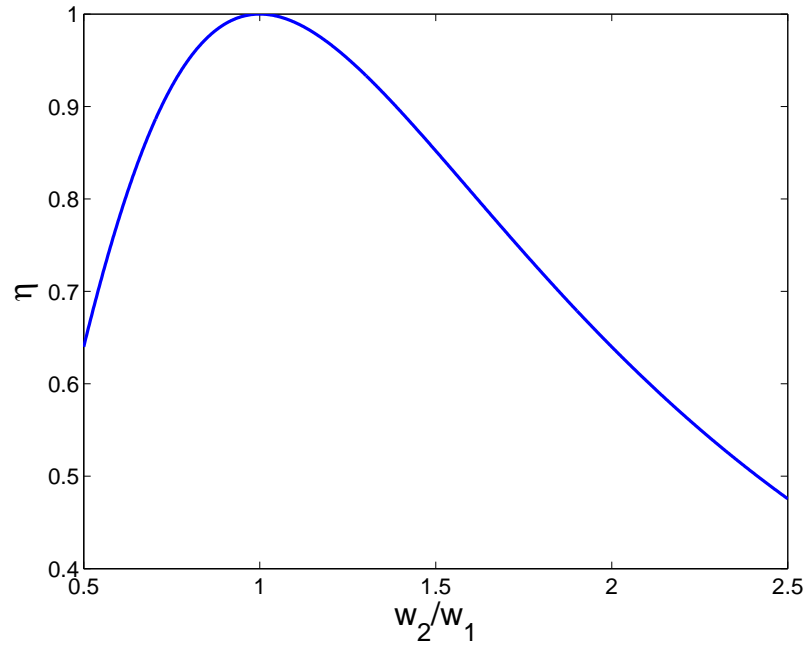


Figure 4.11: Coupling efficiency as a function of ω_2/ω_1 .

Chapter 5

All-Fiber Optical Faraday Components

5.1 All-Fiber Optical Faraday Isolator and Faraday Mirror

5.1.1 Introduction

Optical Faraday isolators and Faraday mirrors are important components in optical communication networks and laser systems. A Faraday isolator is an optical component that allows the transmission of light in only one direction. It is typically used to prevent unwanted feedback into an optical oscillator or amplifier. A Faraday isolator consists of a Faraday rotator and two polarizers, as shown in Fig. 5.1. The input light becomes linearly polarized after polarizer 1, and the polarization direction rotates 45° through the Faraday rotator. Since polarizer 2 is aligned at 45° with respect to polarizer 1, the light beam can pass through polarizer 2. If the light is instead input through polarizer 2, the linearly polarized light after polarizer 2 will again rotate 45° in the Faraday rotator. However the polarization direction of the light will be perpendicular to polarizer 1 due to the nonreciprocal property of the Faraday effect. Therefore, light propagating backward through the isolator is blocked.

Faraday mirrors are widely used in optical amplifiers and oscillators to avoid

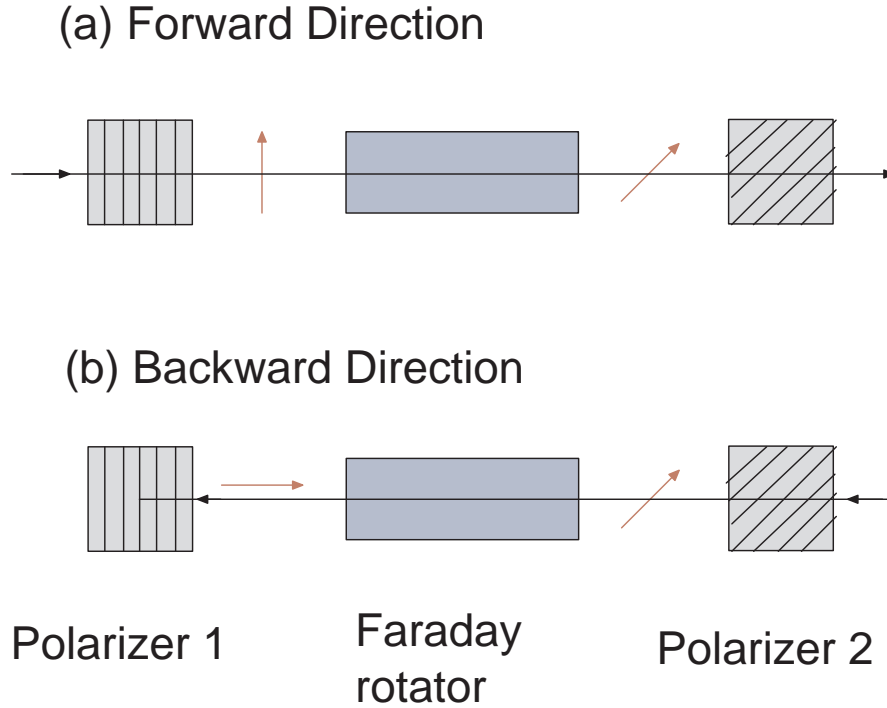


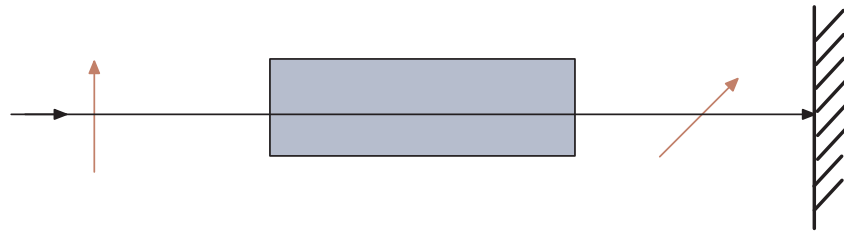
Figure 5.1: Operation of a Faraday isolator illustrated in (a) the forward direction and (b) the backward direction.

spatial hole burning[85], [86] and to stabilize the state of polarization by compensating linear birefringence[87], [88], [89]. A Faraday mirror consists of a 45° Faraday rotator and a mirror, as shown in Fig. 5.2. Linearly polarized light is input into the Faraday rotator and the polarization direction rotates 45° . After it is reflected back by the mirror, it goes through the Faraday rotator again and the polarization direction rotates another 45° , due to the nonreciprocal property of Faraday effect. Therefore, the polarization direction of the reflected light rotates 90° .

As mentioned in Sec. 1.2.3, bulk-optics-based Faraday components suffer from the facet damage, which limits their use in high-power applications. To solve this problem, all-fiber Faraday components are desired. However, there were no commercial all-fiber Faraday components until this thesis, as mentioned in Sec. 3.1.

Some research groups tried to build compact all-fiber Faraday components using standard silica fiber. In 1981, Findakly[90] first proposed a toroidal configuration.

(a) Input Direction



(b) Output Direction

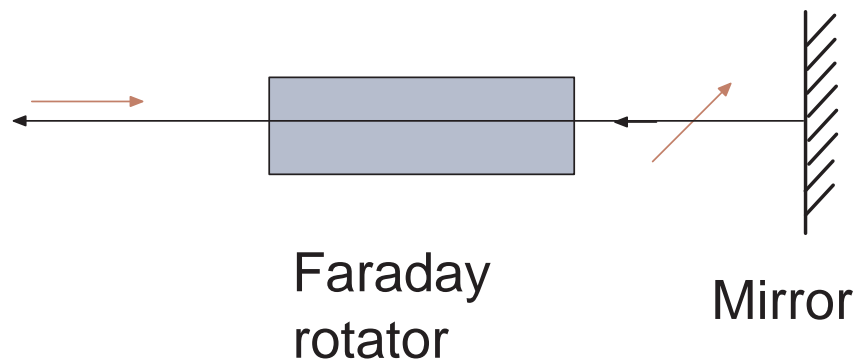


Figure 5.2: Operation of a Faraday mirror illustrated in (a) the forward direction and (b) the backward direction.

In their configuration, a 15-m length of standard silica fiber was coiled 55 turns inside a toroidal solenoid. The fiber was twisted at a rate of 124 rad/m yielding an elasto-optic-induced circular birefringence of the order of 17 rad/m. Since the twisting rate is far above the intrinsic and bending birefringence, the linear birefringence can be neglected[91]. 45° was reached with 2.5 A current input. This configuration only works for a solenoid, and can not applied to permanent magnets.

In 1980, a phase-matching method was proposed to build a compact Faraday rotator[92], [71]. In this method, several meters of fiber were coiled into a multiple-turn circle with several millimeter diameter, and placed in a magnetic field. The circumference of the coil was exactly equal to one beat length of the birefringence caused by the bending. The combined effect of Faraday rotation and birefringence made this configuration work. Annovazzi-Lodi[73] further developed this idea into

a figure-eight coil configuration to double the bending radius. One of the disadvantages of this method is that the bending diameter is very small: 7.5 mm at 633 nm, and less than 3 mm at 1550 nm. Such a small bending radius will induce a large bending loss and increase the failure rate in lifetime performance. The matching condition is precise for only one wavelength, so it can not be tuned for different wavelengths.

In 1991, Lafortune[72] made a 40-cm standard-silica-fiber based Faraday rotator at 633 nm. The magnet shape was optimized and phase retardation was introduced inside the fiber. Unfortunately, the fiber length still extended to more than one meter when used in the communication window at 1550 nm.

Although some all-silica-fiber Faraday components were realized, none of them were commercialized due to their various drawbacks. As mentioned in Sec. 3.1, researchers tried to dope terbium in optical fiber to increase the Verdet constant. Although this terbium-doping method is very effective in increasing the Verdet constant, progress in all-fiber Faraday devices has been limited due to the difficulties in cleaving the Tb fiber, splicing the Tb fiber with standard silica fiber, and developing other fiber components (such as fiber polarizers).

In this section, we demonstrate the first compact all-fiber Faraday isolator and Faraday mirror using terbium-doped fiber. Two kinds of terbium-doped fiber were fabricated. One is 56 wt% Tb-doped, with a Verdet constant of $-24.5 \text{ rad}/(\text{Tm})$. Another is 65 wt% Tb-doped with a record high Verdet constant of $-32.1 \text{ rad}/(\text{Tm})$. This value is 83% of that found in the commercially available crystal (TGG) used in bulk-optics-based isolators, and 27 times larger than that of standard silica fiber.

5.1.2 Terbium Doped Optical Fiber

Terbium doping is an effective way to increase the Verdet constant in the fiber, as described in Sec. 2.2. Highly terbium-doped silicate glasses were designed and fabricated. Boron oxide and aluminum oxide were added into the glass composition to improve the solubility of terbium oxide. Terbium-oxide-doped glass was used as the core glass. The rod-in-tube technique was used for single-mode fiber fabrication. The fiber pulling temperature was around $1000 \text{ }^\circ\text{C}$.

Two terbium-doped fibers were fabricated at AdValue Photonics Inc[93]. using

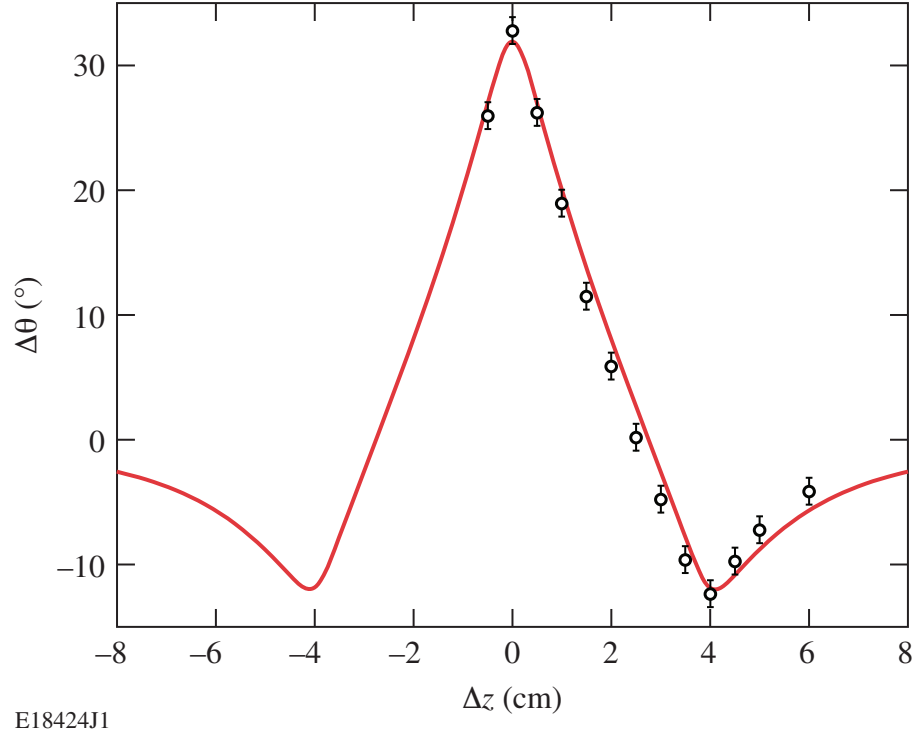


Figure 5.3: Measured rotation angle (circle) and corresponding curve fit (solid) of 56 wt% Tb-doped fiber at a wavelength of 1053 nm as a function of the magnet location along the fiber axis z .

in-house fiber drawing facilities. The first was 56 wt% terbium-doped. The NA and diameter of the core were 0.14 and $4 \mu\text{m}$, respectively, and cladding diameter of the fiber was $130 \mu\text{m}$. The propagation loss of the fiber was measured to be 0.11 dB/cm at 1310 nm using the cut-back technique. Using the measurement technique described in Sec. 3, Fig. 5.3. shows the measured rotation angle and the corresponding curve fit at the measurement wavelength of 1053 nm as the magnet was translated along the length of the fiber. The error in the measured angle was primarily caused by air flow and it is determined to be 1 degree by a polarization stability measurement.

In contrast to the experimental configuration in Sec. 3, two 15-cm pieces of straight single mode (SM) fiber were used on either side of the Tb doped fiber. All other experimental components were identical to Sec. 3. From Eq. 3.5, the total

rotation angle can be derived as

$$\begin{aligned}\Delta\theta_{tot} &= V_{meas} \int_{-l/2}^{l/2} B_z(z) dz \\ &= V_{Tb} \int_{-l/2}^{l/2} B_z(z) dz + V_{silica} \left(\int_{-\infty}^{-l/2} B_z(z) dz + \int_{l/2}^{+\infty} B_z(z) dz \right),\end{aligned}\quad (5.1)$$

where L , V_{meas} , V_{Tb} , and V_{Silica} are length of magnet, measured Verdet constant, and effective Verdet constants of the Tb and the silica fibers, respectively. As described in Sec. 3.3, the axially integrated magnetic field inside and outside the magnet tube have opposite signs but identical absolute values, $\int_{-l/2}^{l/2} B_z(z) dz = -(\int_{-\infty}^{-l/2} B_z(z) dz + \int_{l/2}^{+\infty} B_z(z) dz)$. Therefore, Eq. 5.1 can be simplified as

$$V_{meas} = V_{Tb} - V_{Silica}.\quad (5.2)$$

$V_{meas} = -25.7 \pm 1.0 \text{ rad}/(Tm)$ and $V_{Silica} = 1.2 \text{ rad}/(Tm)$ at 1053 nm [94], V_{Tb} was determined to be $-24.5 \pm 1.0 \text{ rad}/(Tm)$, which is 22% larger than previously reported results[77]. This measurement is in reasonable agreement with a 27% increase in Tb^{3+} concentration, from 0.66×10^{22} in ref. [77] to $0.84 \times 10^{22} \text{ ions}/cm^3$ in this Tb fiber.

Although the rotation angle of 56 wt% Tb-doped fiber in N48 magnet tube can not reach 45° , the rotation angle of a piece of 21 cm long of the same fiber in the N35 magnet cuboid can exceed 70° , as shown in Fig. 5.4. Due to physical geometry, the rotation angle can not be readily measured in a such large magnet. Therefore, only the theoretical result is shown here.

The second fiber is 65 wt% Tb-doped fiber. The NA and diameter of the core were 0.083 and $7.4 \mu m$, respectively, with the cladding diameter of the fiber $125 \mu m$. The propagation loss of the fiber was measured to be 0.024 dB/cm at 1310 nm using the cut-back technique. The polarization rotation angle in the Tb fiber was measured using the same method described above. A 4-cm Tb fiber was spliced with two short pieces of single-mode (SM) fiber at both ends in order to increase the total rotation angle. Figure 5.5 shows the measured rotation angle and the corresponding curve fit at the measurement wavelength of 1053 nm as the magnet was translated along the length of the fiber. The maximum rotation angle reached

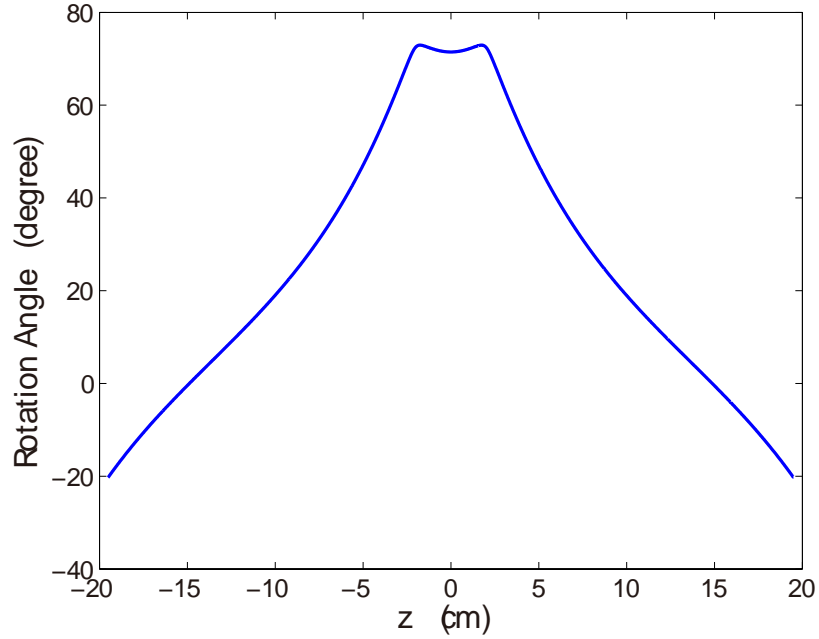
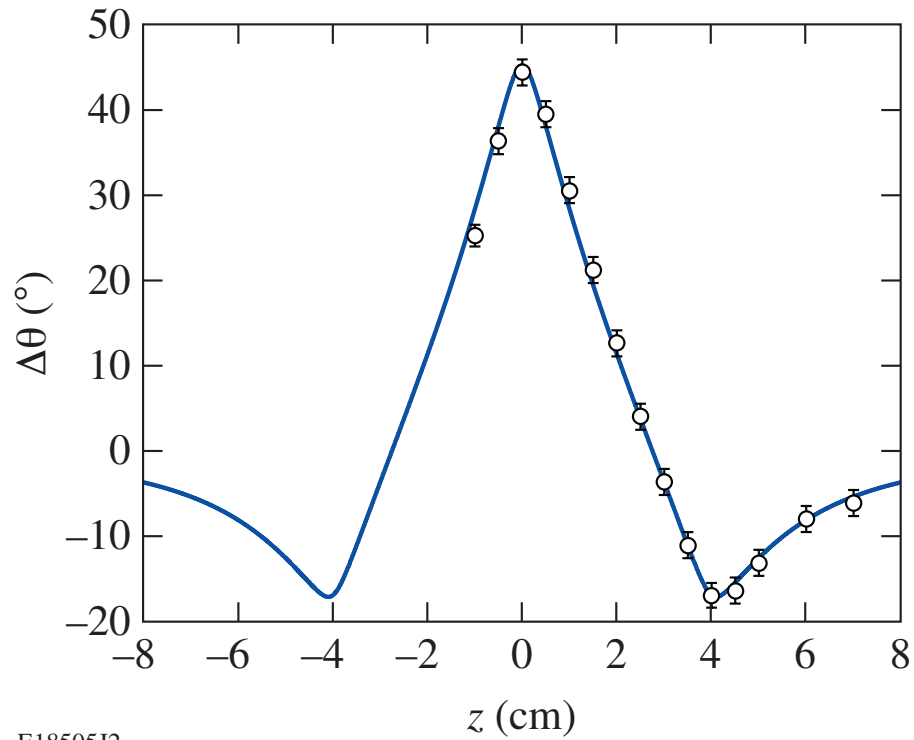


Figure 5.4: Theoretical rotation angle of 56 wt% Tb-doped fiber at a wavelength of 1053 nm as a function of the N35 magnet location along the fiber axis z .

45°. The error in the measured angle was primarily caused by air flow and it was determined to be 1 degree by a polarization stability measurement. The effective Verdet constant was determined to be $-32.1 \pm 0.8 \text{ rad}/(Tm)$, which is 27 times larger than that of silica fiber and the largest measured to date in any optical fiber.

Figure 5.6 shows the measured and curve-fit Verdet constants of the 54 wt% Tb fiber[77], 56 wt% Tb fiber, 65 wt% Tb fiber and TGG[77] as a function of Tb^{3+} concentration. From the figure, it is clear that the Verdet constant is proportional to the Tb^{3+} concentration, in agreement with Eqs. 2.13 and 2.14. The Verdet constant of the 65 wt% Tb fiber is 31% larger than that of 56 wt% Tb fiber, and reaches 83% of the Verdet constant of the commercially available crystal, terbium gallium garnet (TGG), used in bulk-optics-based isolators.



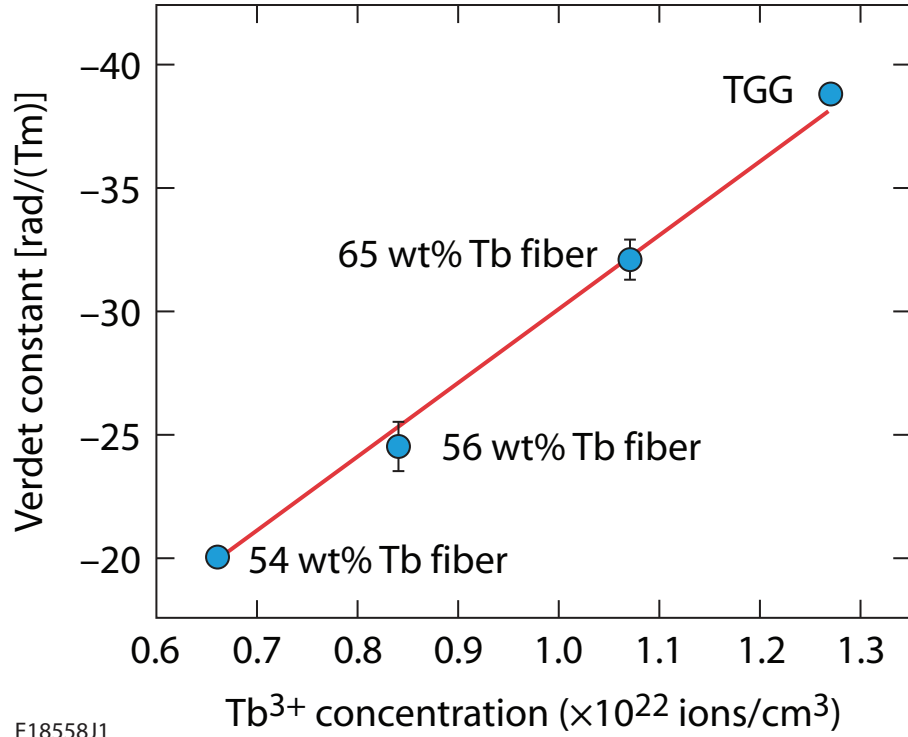
E18505J2

Figure 5.5: Measured rotation angle (circle) and corresponding curve fit (solid) of 65 wt% Tb-doped fiber at a wavelength of 1053 nm as a function of the magnet location along the fiber axis z .

5.1.3 All-Fiber Polarizers

Single-polarization fiber (PZ) is a specialty fiber, in which only one polarization mode can propagate [95], [96], [97], [98]. Generally, this kind of fiber has a large birefringence to separate the two orthogonal polarization modes so that each has a different cutoff wavelength. Therefore, within a certain wavelength region, one polarization mode is eliminated due to high loss and the other propagates. In this way, the fiber functions as an all-fiber polarizer. Birefringence is usually introduced via stress from boron-doped rods, elliptical core/cladding, and/or air holes.

There are two current commercial products using this technique. One is Corning SP1060 fiber [99], [100], [101], [102], which has been used in our experiments. The cross-section structure and image of this SP1060 fiber are shown in Figs. 5.7 and 5.8, respectively. With two air holes beside an elliptical core, a large birefringence and differential fundamental mode cutoff are achieved in the SP1060 fiber.



E18558J1

Figure 5.6: Measured (dot) and curve fit (line) Verdet constants of the 54 wt% Tb fiber, 56 wt% Tb fiber, 65 wt% Tb fiber and TGG as a function of Tb^{3+} concentration.

The core diameter along the major axis was $8 \mu m$, and the cladding diameter was $125 \mu m$, with a core N.A 0.14. The propagation loss was $0.1 dB/m$ at $1060 nm$. The measured transmission spectrum for two orthogonal polarization directions in a $0.3 m$ length of SP1060 fiber coiled with a 15-cm diameter is shown in Fig. 5.9. The center wavelength was $1065 nm$, and the bandwidth was $25 nm$. The extinction ratio was $> 16 dB$. The purpose of coiling the fiber was to shift the polarizing bandwidth towards shorter wavelengths, which will include the 1053-nm working wavelength. Since increasing the PZ fiber length increases the extinction ratio[99], 1-m of PZ fiber is used in the isolator experiment. Another polarizing fiber is Fibercore Zing fiber, which is high-birefringence bow-tie fiber. This kind of fiber is similar to the Corning SP1060 fiber and will not be discussed further.

Besides the two polarizing fibers mentioned above, there is another commercial product, called *Helica In-Fiber Polarizers* from Chiral Photonics, Inc, which uses different physics mechanism. This fiber polarizer is a chiral scattering grating

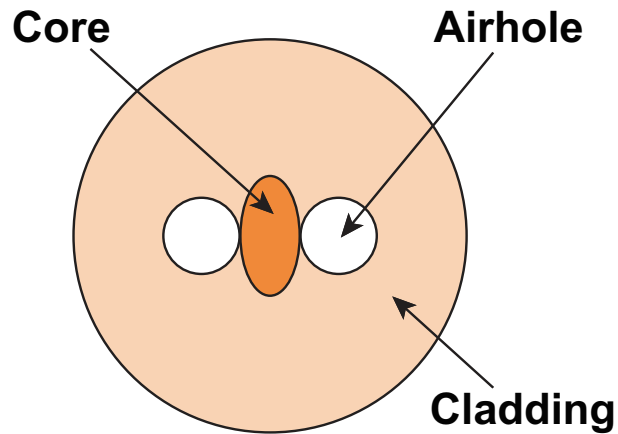


Figure 5.7: Cross-section structure of the SP1060 fiber.

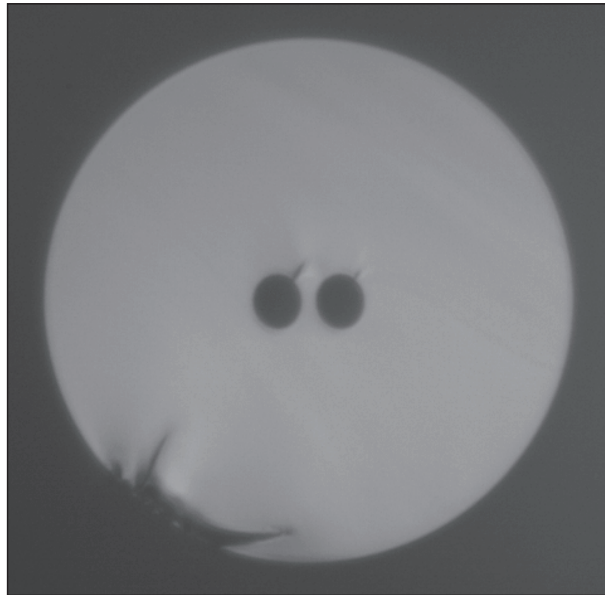


Figure 5.8: Cross-section image of the SP1060 fiber.

(CSG) made from a twisted birefringent fiber[103], as shown in Fig. 5.10 (Courtesy of Chiral Photonics). Two linear polarized modes from the input end can be converted into two circular polarized modes in the adiabatically twisted region. One circular polarized mode is blocked by the grating and the other propagates. The propagating circular polarized mode is then adiabatically converted back into a linear polarized mode. In this way, the CSG works as a fiber polarizer. The fiber polarizer, which was also used in the experiments, had a 4-cm long CSG with

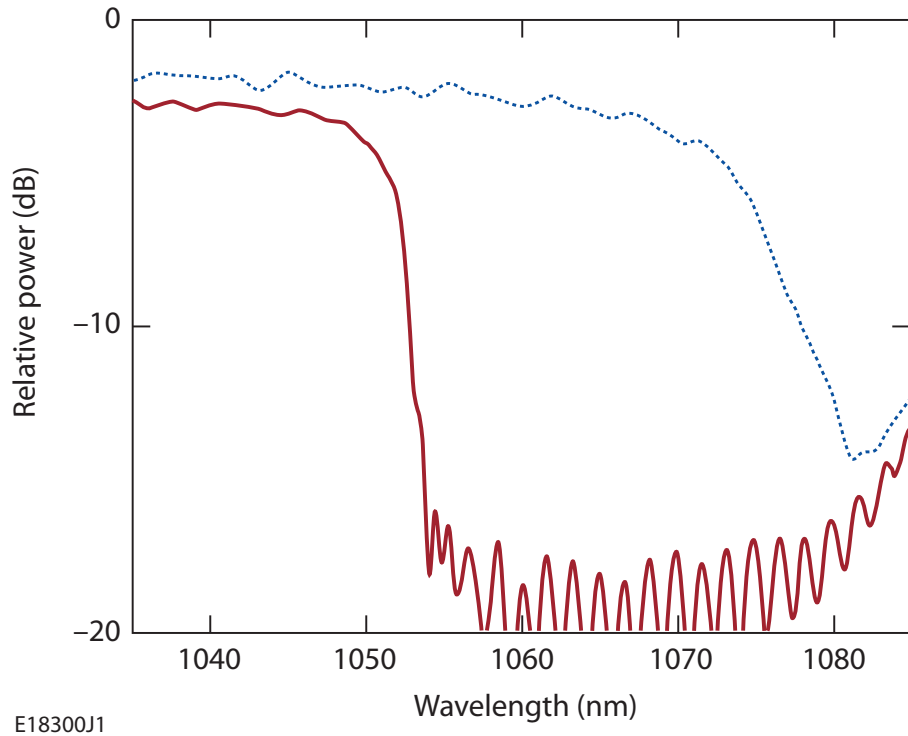


Figure 5.9: Measured transmission spectra for two orthogonal polarization directions in a 0.3-m-long SP1060 fiber coiled with a 15 cm diameter.



Figure 5.10: Longitudinal structure of the CSG (Courtesy of Chiral Photonics).

polarization-maintaining (PM) fiber pigtailed at both ends. The center wavelength was around 1064 nm, with a bandwidth greater than 50 nm. The polarization extinction ratio of the fiber polarizer was greater than 30 dB, and the insertion loss was less than 2 dB, as shown in Fig. 5.11 (Courtesy of Chiral Photonics).

A single-polarization fiber can also be realized in photonic crystal fibers[104], [105]. A suitable arrangement of microscopic air holes breaks the rotational symmetry and introduces polarization-dependent guiding properties. No commercial products are based on this technology so it will not be discussed here.

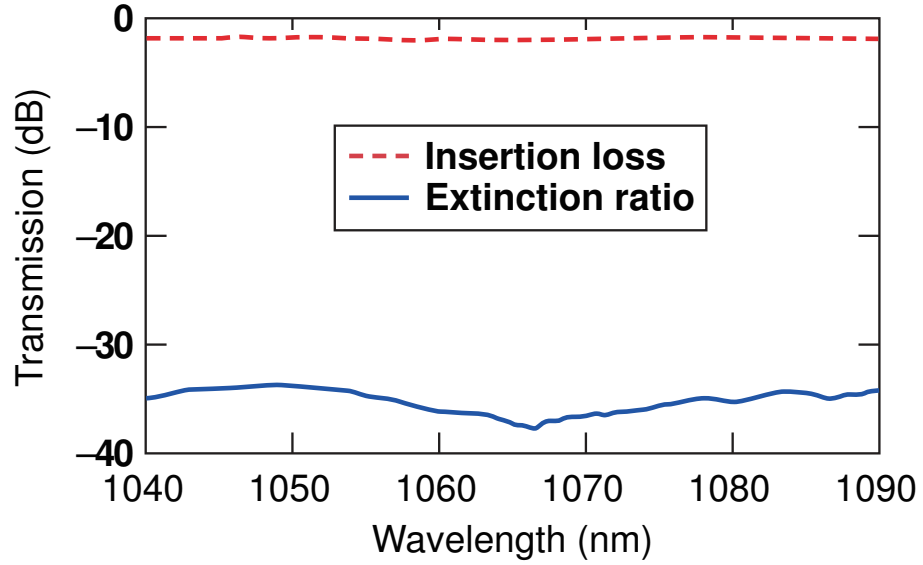


Figure 5.11: Measured insertion loss and extinction ratio for CSG (Courtesy of Chiral Photonics).

5.1.4 All-Fiber Optical Faraday Isolator

Two all-fiber optical Faraday isolators have been demonstrated. The first one is based on the 56 wt% Tb fiber, the Corning SP1060 PZ fiber polarizer, and the N35 NdFeB magnet (as shown in Sec. 2.3 and 5.1). This isolator was relatively heavy, large, and had a high optical propagation loss. After increasing the Tb-fiber doping concentration and optimizing the fusion splicing program, the second all-fiber optical Faraday isolator was built based on the 65 wt% Tb fiber, the Helica In-Fiber Polarizers, and the N48 NdFeB magnet, as shown in Sec. 2.3 and 5.1. This second isolator was light, compact and had much lower optical loss.

The experimental configuration of the first isolator is shown in Fig. 5.12. A 25-cm section of 56 wt% Tb-doped fiber, spliced between two 1-m sections of PZ fiber (with an extinction ratio of 18 dB at 1053 nm), went through the N35 NdFeB magnet. The 1-m long PZ fiber was coiled with a 15-cm diameter. The polarization directions of the two sections of the PZ fiber were aligned with a rotational difference of 45° . The location of the magnet was adjusted with respect to the Tb fiber to achieve the 45° rotation. The maximum possible polarization rotation angle in this configuration was larger than 70° .

The optical isolation of the first isolator at 1053 nm was measured to be 17

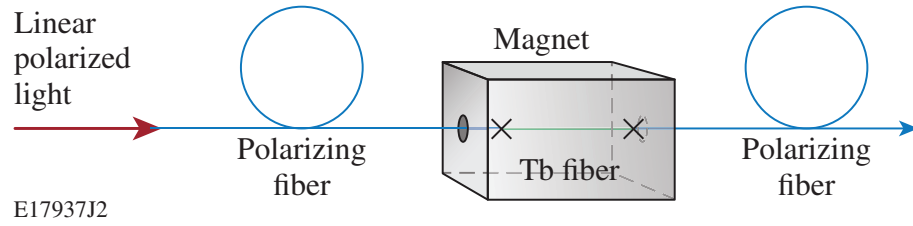


Figure 5.12: Experimental configuration of the first all-fiber Faraday isolator.

dB at room temperature. The loss of the isolator was 9 dB, including 0.2 dB of propagation loss in the total 2-m of PZ fiber, 2.8 dB of propagation loss in 56 wt% Tb-doped fiber, and 3 dB from each splicing point between the PZ and 56 wt% Tb-doped fiber. The loss contribution due to the Tb-doped fiber could be decreased to under 0.5 dB by using a higher grade magnet and a higher Tb-doping concentration. This configuration would require only a few centimeters of Tb-doped fiber, as will be demonstrated below. The loss induced by the mode mismatch between PZ and Tb-doped fiber is 1.8 dB per splicing point, which can be reduced via fiber mode converter. The remaining 1.2 dB loss per splice point is due to the splicing process. The melting points of the terbium-oxide-doped silicate fiber and silica fiber are 1200 °C and 1650 °C respectively, making it difficult to melt them together using a conventional fusion splicer. Although this splicing loss is high, it could be decreased further by using a custom setup, for example using a temperature controllable heating filament.

The experimental configuration of the second isolator is shown in Fig. 5.13. A much shorter 4-cm section of Tb-doped fiber, spliced between two short pieces of SM fiber, went through the higher grade N48 NdFeB magnet tube. The two other ends of the SM fibers were each spliced to a CSG fiber polarizer. The polarization directions of the two fiber polarizers were aligned with a rotational difference of 45°.

The reason for splicing two pieces of SM fiber is to increase the total Verdet constant. Since the axial magnetic field outside the magnet can be neglected beyond 4 cm past the end of the magnet, the effective length of the Faraday fiber is 12 cm, including 4-cm Tb fiber and two 4-cm pieces of SM fiber. The SM fiber could be eliminated by using a stronger magnet, for example, an N50 NdFeB magnet, or by increasing the outer diameter of the magnet tube by a few percent.

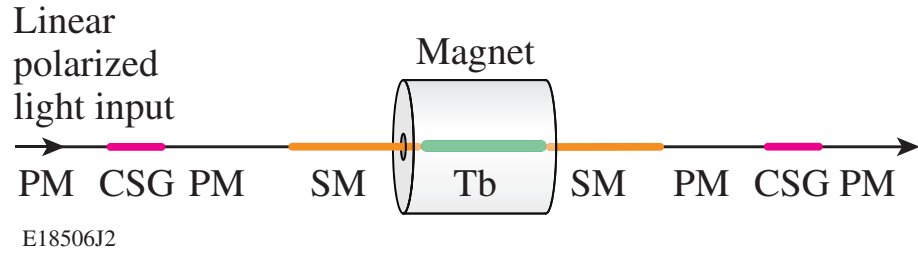


Figure 5.13: Experimental configuration of the second all-fiber Faraday isolator.

Then the effective length of the Faraday fiber could be only 4 cm.

The optical isolation of the second isolator at 1053 nm was measured to be 19 dB at room temperature. The loss of the isolator was 6.1 dB, including 2 dB insertion loss of each CSG, 0.1 dB of propagation loss in 65 wt% Tb-doped fiber, 1 dB from each splicing point between the SM and 65 wt% Tb-doped fiber. Recent progress in CSGs has demonstrated a reduction of insertion loss of the fiber polarizer to less than 0.5 dB [106]. The 1 dB loss per splice point occurs because the difference between the melting points of the terbium-oxide-doped silicate fiber and silica fiber, as mentioned above. By implementing these improvements, an all-fiber Faraday isolator could be made with less than 1 dB insertion loss.

Our collaborator, AdValue Photonics launched the first commercial all-fiber Faraday isolator in CLEO 2010, as shown in Fig. 5.14. This product, which is based on our research on all-fiber isolators, has an isolation of 20 dB, operating wavelength of 1060 nm, and an insertion loss of 1 dB. 4 isolators are integrated in one magnet package, which is a significant advantage of all-fiber isolators relative to their free-space counterparts.

5.1.5 All-Fiber Optical Faraday Mirror

Similar to the isolators, two all-fiber optical Faraday mirrors have been demonstrated here. The first one was based on the 56 wt% Tb fiber, a fiber Bragg grating and N35 NdFeB magnet (as shown in Sec. 2.3 and 5.1), which was also relative heavy, large, and had large optical propagation loss. After increasing the Tb-fiber doping concentration and optimizing the fusion splicing program, the second all-fiber optical Faraday mirror was built based on the 65 wt% Tb fiber, a fiber Bragg grating and the N48 NdFeB magnet, as shown in Sec. 2.3 and 5.1.



Figure 5.14: The commercial all-fiber Faraday isolator. Photo courtesy of AdValue Photonics.

The second Faraday mirror was light, compact, and had much smaller optical loss.

A fiber Bragg grating (FBG) is a periodic structure in the optical fiber that reflects light within a certain wavelength range. The principle and properties of FBGs have been discussed in detail elsewhere[107], [108], therefore they will not be covered here. An FBG with a center wavelength of 1053 nm, a reflectivity of 97% and a bandwidth of 1 nm was used in the experiment as an all-fiber mirror.

The experimental configuration used to test the first Faraday mirror is shown in Fig. 5.15. A 21-cm section of 56 wt% Tb-doped fiber, spliced between polarization maintaining (PM) fiber and a 30-cm section of single-mode (SM) fiber,

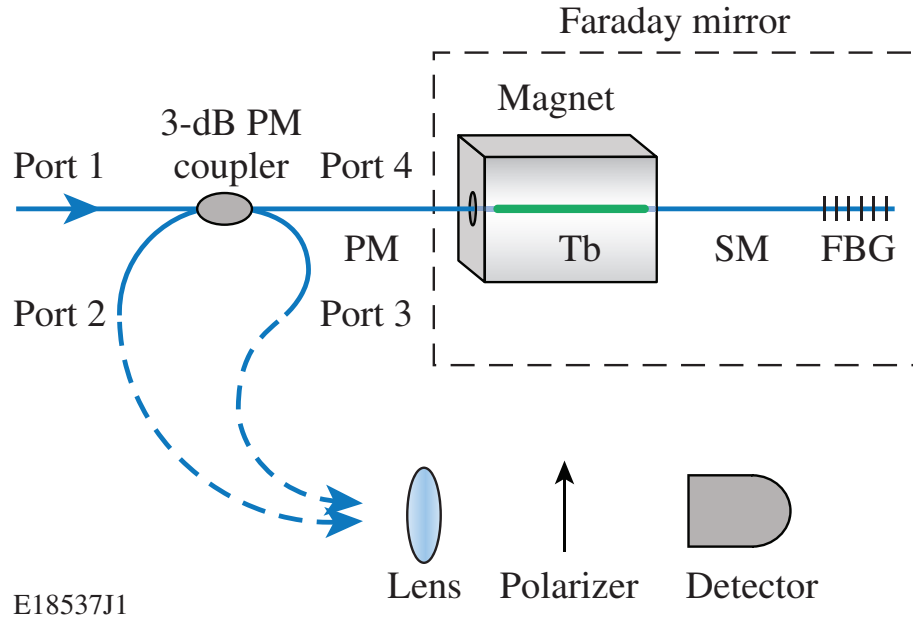


Figure 5.15: Experimental configuration of the first all-fiber Faraday mirror.

went through the N35 NdFeB magnet. The FBG was spliced to the other end of the SM fiber. The SM fiber is short and kept straight to avoid changes to the polarization state. A 4-port 3 dB PM coupler was spliced with the PM fiber for testing purposes. Linearly polarized 1053-nm light was launched into the PM fiber via port 1. Then it went through the Faraday rotator (Tb fiber), and the polarization state rotated 45° . After it was reflected back by the FBG, the polarization state rotated another 45° at the Faraday rotator and the total polarization rotation angle reached 90° . The polarization states of the output and input light were measured at ports 2 and 3 respectively. The location of the magnet was adjusted with respect to the Tb fiber to achieve the total 90° rotation.

When measuring the polarization state, the light went through a lens and a polarizer, and was finally collected by a detector. When the polarizer was rotated by an angle θ , the light intensity I at the detector was a cosine-square function $I/I_0 = \cos^2(\theta - \theta_0^i)$, which is the well-known Malus' Law[109]. I_0 is the maximum light intensity received by the detector, and θ_0^i represents the polarization state of the input and the output light (i=input, output). Fig. 5.16. shows the measurement results. The triangles and circles are measurement points of the input and output light, respectively. The dashed and solid lines are curve-fits of the input

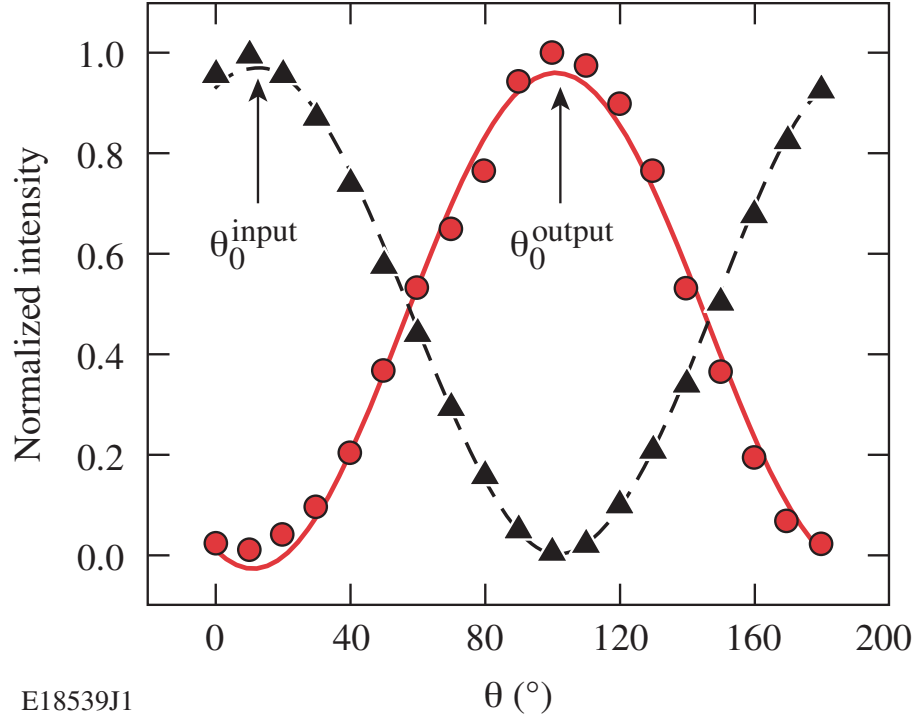


Figure 5.16: Polarization state measurement of the input and output light of the first Faraday mirror. Triangles and circles are measurement points of the input and output light, respectively. Dashed and solid lines are curve-fits of the input and output light, respectively.

and output light, respectively. The polarization rotation angle is calculated to be $\theta_0^{output} - \theta_0^{input} = 89 \pm 2^\circ$.

The insertion loss of the Faraday mirror was 13.7 dB, including 4.6 dB propagation loss of 56 wt% Tb fiber (round trip), 0.1 dB reflection loss from the FBG, and 2.3 dB splicing loss per slice point between 56 wt% Tb and silica fiber (PM and SM). The extinction ratios of the input and output light were 20 and 16 dB, respectively. If the length of SM fiber between Tb fiber and FBG was reduced, the extinction ratio of the output light could be increased close to 20 dB.

The experimental configuration used to test the second Faraday mirror is shown in Fig. 5.17. A 4-cm section of Tb-doped fiber, spliced between two short pieces of SM fiber, went through the N48 NdFeB magnet. The same FBG used in the first Faraday mirror was spliced to the other end of one of the SM fibers. The SM fiber was short and kept straight to avoid altering the polarization state. The same 4-port 3 dB PM coupler was spliced with the other SM fiber for testing purposes.

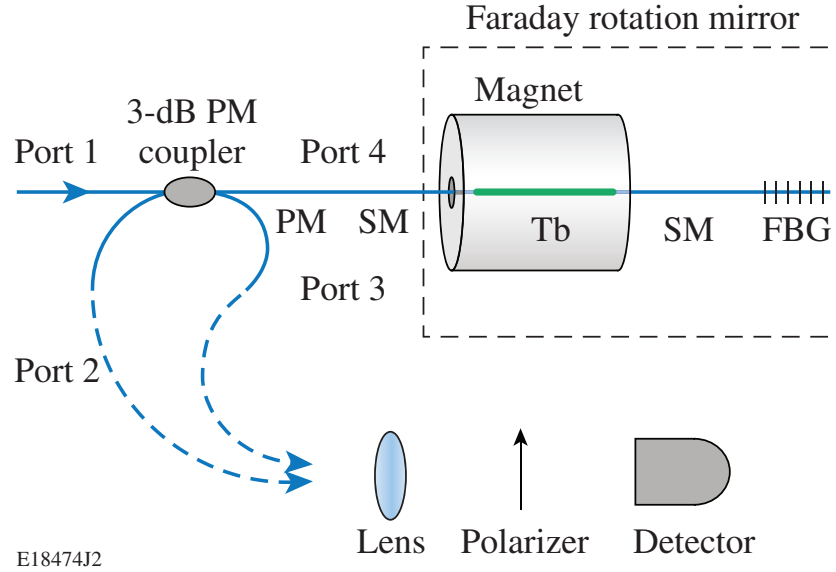


Figure 5.17: Experimental configuration of the second all-fiber Faraday mirror.

Fig. 5.18. shows the measurement results. Squares and circles are measurement points of the input and output light, respectively. The dashed and solid lines are curve-fits of the input and output light, respectively. The polarization rotation angle was calculated to be $\theta_0^{output} - \theta_0^{input} = 88 \pm 4^\circ$. The error was measured from the polarization stability measurement of the Faraday mirror configuration, which is different from the Verdet constant measurement configuration.

The insertion loss of the second Faraday mirror was 4.3 dB, including 0.2 dB propagation loss from 65 wt% Tb fiber (round trip), 0.1 dB reflection loss from the FBG and 1 dB splicing loss per splice point between 65 wt% Tb and SM fiber, which is counted four times. Similar to the isolator, the splicing loss could be decreased by using a temperature controllable heating filament, resulting in an all-fiber Faraday mirror with insertion loss of less than 0.5 dB. The FBG can also be written on Tb fiber directly, which would also reduce the splicing loss by half. The extinction ratios of the input and output light are 20 and 13 dB, respectively. The reason of a lower extinction ratio compared with the previous experiment is due to the defects in fiber connectors. If the SM fiber between the Tb fiber and FBG were shortened, and the fibers were fusion spliced, the extinction ratio of the output light could be increased to the 20 dB input level.

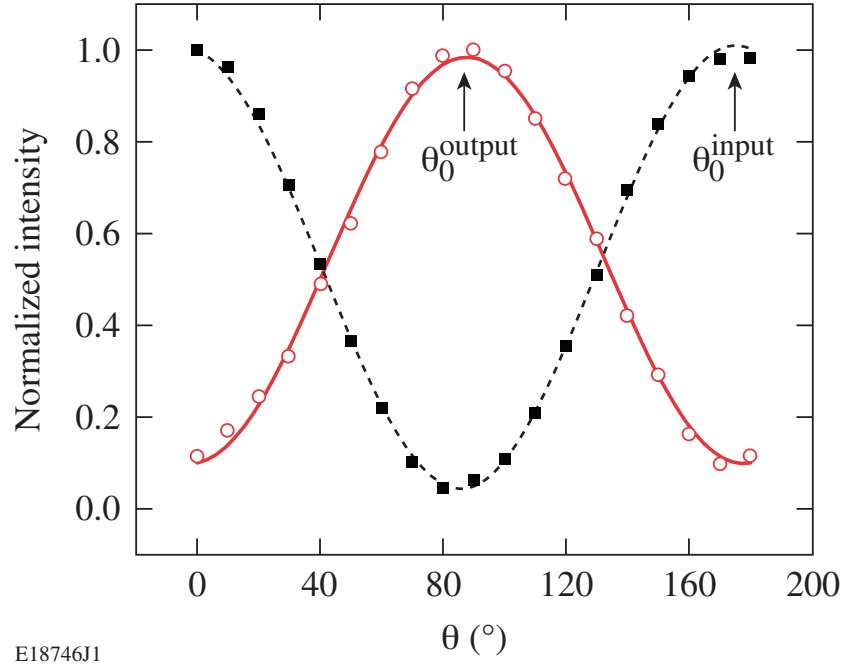


Figure 5.18: Polarization state measurement of the input and output light of the second Faraday mirror. Squares and circles are measurement points of the input and output light, respectively. Dashed and solid lines are curve-fits of the input and output light, respectively.

5.1.6 Discussion

The compact all-fiber Faraday isolator and Faraday mirror will have significant impact in high-power fiber laser systems. There are no material/air interfaces or epoxy problems found in bulk optics Faraday components, increasing the damage thresholds required for high power applications. Since hundreds of pieces of Tb fiber can go through one magnet tube at the same time, many Faraday components can be integrated into a single magnet, as shown in Fig. 5.19. This would reduce cost and size in large fiber array systems.

In conclusion, an all-fiber Faraday isolator and Faraday mirror are demonstrated. The isolator consists of two fiber polarizers and a fiber Faraday rotator. The latest fiber Faraday rotator was made of a 4-cm long 65 wt% terbium-doped silicate fiber. The effective Verdet constant of the 65 wt% terbium-doped fiber was measured to be $-32.1 \pm 0.8 \text{ rad}/(Tm)$, which is 27 times larger than that of silica fiber. This effective Verdet constant is the largest measured value to date in any

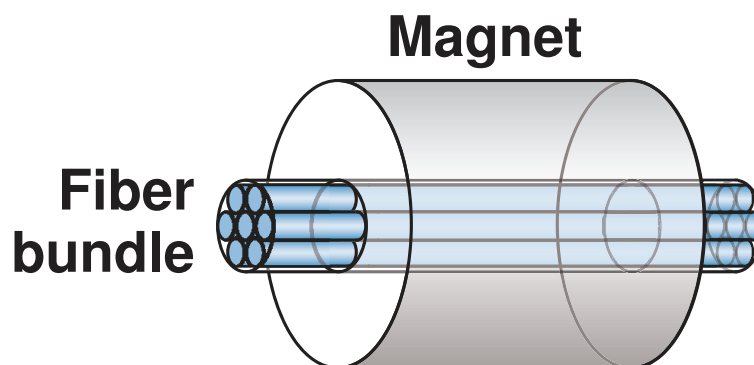


Figure 5.19: Integration of all-fiber Faraday components.

fiber, and is 83% of the Verdet constant of commercially available crystal (TGG) used in bulk optics based isolators. The isolation of this fully fusion-spliced all-fiber isolator was measured to be 19 dB. The Faraday mirror consists of an all-fiber Faraday rotator and a fiber Bragg grating as mirror. The polarization state of the reflected light is rotated $88 \pm 4^\circ$. The work in this section has been published in references [110], [111], and [112].

5.2 All-fiber Optical Magnetic Field Sensor

5.2.1 Introduction

Magnetic field sensors have been widely used for navigation, vehicle detection, current sensing, and spatial and geophysical research. Many techniques developed for magnetic field sensor are based on electronics, including Superconducting Quantum Interference Devices (SQUIDS), Search Coils, Fluxgates, Hall effect sensors and anisotropic magnetoresistive devices[113]. These magnet sensors can work in many applications. However, they are not suitable for strong Electro-Magnetic Interference (EMI) environments, because the presence of strong ancillary electromagnetic signals causes errors in such electronic sensors. All-fiber optical magnetic field sensors are desirable in strong EMI environment due to their immunity to electromagnetic interference, low weight, small size, and long distance signal transmission for remote operation.

Many all-fiber magnetic field sensors use material coatings. For example, if a

magnetostrictive or metal jacket is deposited on the fiber, the optical phase can be changed by strain or Lorentzian force, respectively, when immersed in a magnetic field[114], [115]. In another method, a fiber end is coated with a composite material and butt coupled to another fiber. The optical coupling between the fibers changes with the transverse displacement of the coated fiber in the magnetic field[116]. In yet another method, iron film is deposited on a side-polished fiber Bragg grating. The reflective wavelength of the fiber grating shifts with the strain induced by a magnetic field[117].

Faraday rotation can be used for magnetic field sensors. Because the Verdet constant of silica fiber is small [~ 1.1 rad/(Tm) at 1064 nm], the fiber is usually coiled multiple-turns to increase the polarization rotation angle. This kind of magnet sensor is often used for current sensing[71], [73]. However, bend-induced linear birefringence affects the state of polarization and quenches the desired Faraday effect. In this section, an all-fiber optical magnetic field sensor based on Faraday rotation is demonstrated. The device is made of a fiber Faraday rotator spliced to a fiber polarizer. The fiber Faraday rotator is a 2-cm long 56 wt% terbium-doped fiber, which is sufficiently short to avoid bending. The fiber polarizer is Corning SP1060 single polarization fiber (PZ).

5.2.2 Experiment

The magnetic sensing principle is shown in Fig. 5.20. Linearly polarized input light from the laser source is transmitted to the Tb fiber via polarization maintaining (PM) fiber. The polarization of the light rotates when the Tb fiber experiences a magnetic field along the axis of light propagation. The light then goes through the fiber polarizer, which extinguishes light whose polarization is not aligned to its principle axis. PM fiber transmits the remaining light to a detector. Due to the polarizer, the power received at the detector is a function of the polarization rotation angle given by Malus' Law[109]. Since the polarization rotation angle in the Tb fiber is related to the magnetic field strength by the Faraday effect, the magnetic field can be measured by monitoring the output power of the sensor.

The experimental configuration used to test the sensor is shown in Fig. 5.21. A 2-cm section of 56 wt% Tb-doped fiber, spliced between the PM fiber and 1-m sec-

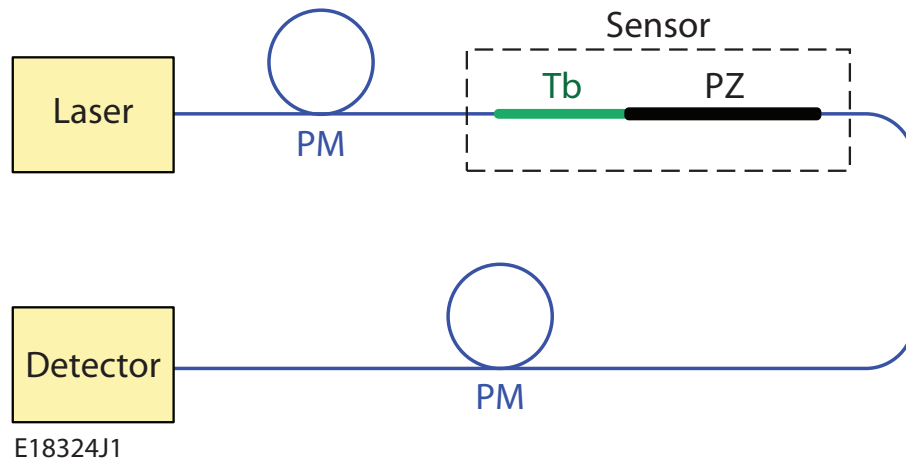


Figure 5.20: Sensing principle of the all-fiber Faraday magnet sensor.

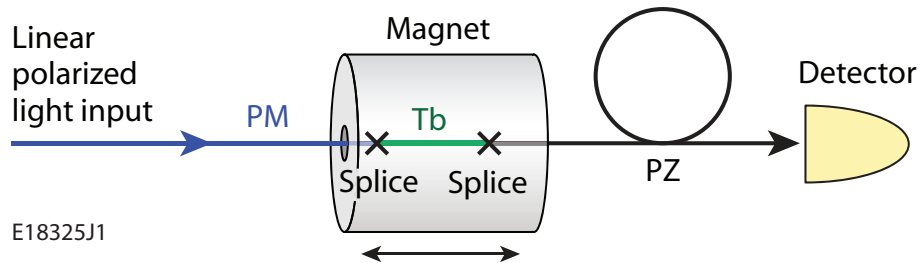
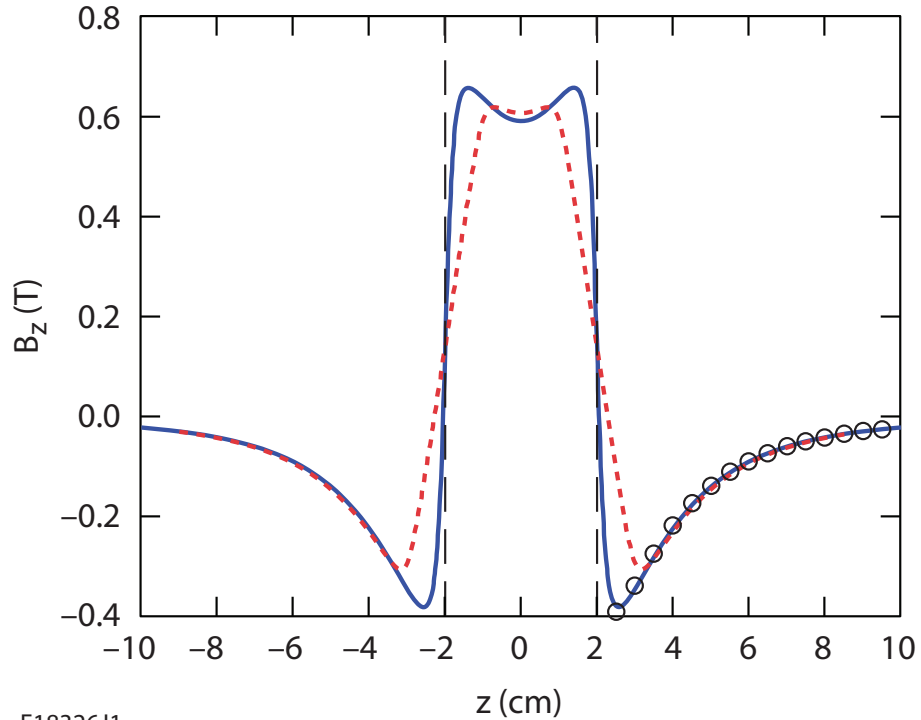


Figure 5.21: Experimental configuration of the all-fiber magnet sensor.

tion of SP1060 PZ fiber, went through the N48 NdFeB magnet. Linearly polarized 1053-nm light was launched into the PM fiber. The polarization directions of the PM and the PZ fibers were aligned with a rotational difference of θ_0 , which should be set between 20° to 70° to obtain a nearly linear response curve of magnetic field strength as a function of measured power. As the magnet was translated along the fiber, the magnetic field imposed on the Tb fiber changed. The averaged magnetic density flux B_{av} experienced by the 2-cm length of Tb fiber (calculated in the center of Tb fiber) is shown in the Fig. 5.22. This curve is nearly linear from -3 to -1 cm along the z axis. This region was used in the measurement.

After considering the extinction ratio of the polarizing fiber, E_x , the relative transmission through the SP1060 PZ fiber is derived as [118].

$$I/I_0 = \cos^2(\theta_0 + \theta) + \sin^2(\theta_0 + \theta)10^{(-E_x/10)} \quad (5.3)$$



E18326J1

Figure 5.22: Theoretical (solid) and measured (circle) magnetic density flux distribution B_z along the center axis z . Dashed lines represent the magnet ends, and the dotted line represents B_{av} , the magnetic density flux averaged over a 2-cm length along the axis z .

I/I_0 is the measured output power normalized to its maximum I_0 . $\theta = VB_{av}L$ is the Faraday rotation angle in the Tb fiber. V and L are the effective Verdet constant and the length of the Tb fiber respectively. In the experiment, $\text{Ex}=18$ dB and $\theta_0 = 50^\circ$. The experimental and theoretical curves of the relative transmission are shown in Fig. 5.23. The error was determined to be 0.01 by a polarization stability measurement. The experimental data agrees well with the theoretical curve, both of which show a nearly linear response. The nominal transmission loss through the device is 10 dB, mainly induced by the mode mismatch between PZ fiber and 56 wt% Tb fiber, and splicing loss between the Tb fiber and silica fiber.

Using Eq. 5.3, the measured Verdet constant of the device and the relation $\theta = VB_{av}L$, B_{av} was measured in the linear response region using the all-fiber sensor. Figure 5.24 shows that the measurement agrees exceptionally well with the theoretical curve, derived from the solid curve in Fig. 5.22.

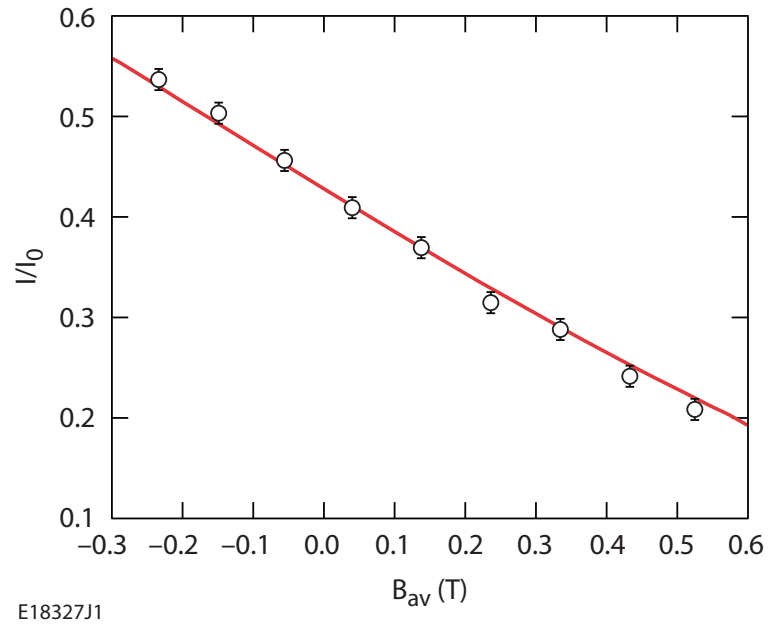


Figure 5.23: Measured (circle) and calculated (solid) relative transmission of the all-fiber magnet sensor.

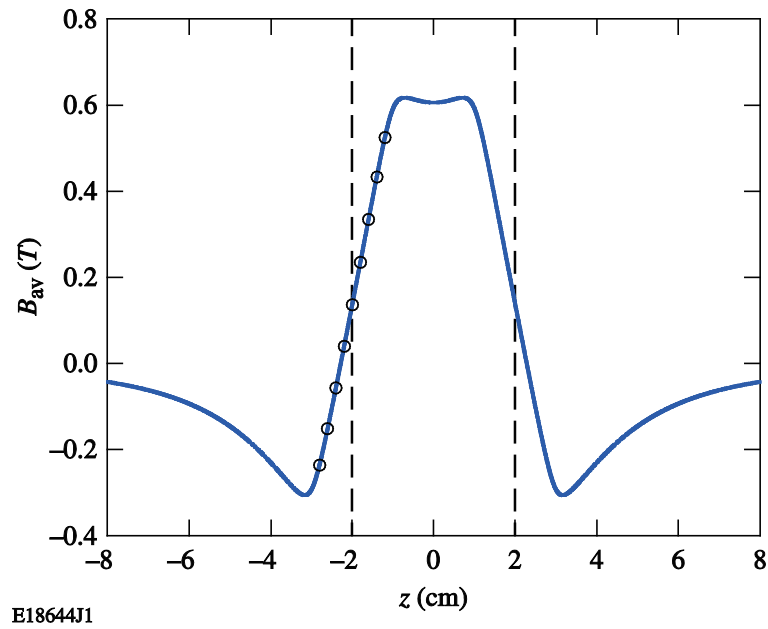


Figure 5.24: Measured (circles) and theoretical (solid) B_{av} as a function of the z axis. The dashed lines represent the end of the magnet.

5.2.3 Discussion

The sensitivity of the all-fiber sensor is given $d\theta/dB_{av} = VL = 0.49 \text{ rad/T}$. This can be increased by increasing the effective Verdet constant and/or length of the Tb fiber. If the 65 wt% Tb-doped fiber described in Sec. 5.1.2 was used here, the sensitivity would increase by 31%. Since the polarization rotation may go beyond 90° , a maximum detected magnetic field $B_{max} = \frac{\pi/2}{VL}$ of 3.2 T can be measured in this configuration without ambiguity. A larger magnetic field could be measured by decreasing the effective Verdet constant or the length of the Tb fiber.

The resolution of the magnetic sensor is obtained by taking the derivative and absolute value of both sides of Eq. 5.3,

$$\begin{aligned} \Delta B &= \frac{\Delta I}{I_0 VL \sin[2(\theta_0 + \theta)](1 - 10^{-Ex/10})} = \frac{\Delta I}{I_0} \frac{2B_{max}}{\pi \sin[2(\theta_0 + \theta)](1 - 10^{-Ex/10})} \\ &\approx \frac{\Delta I}{I_0} \frac{2B_{max}}{\pi \sin[2(\theta_0 + \theta)]}. \end{aligned} \quad (5.4)$$

In the approximate form of this equation, the effect of the extinction ratio is neglected, which is appropriate for $Ex \geq 18$. Increasing the effective Verdet constant and the length of the Tb fiber could increase the resolution, at the expense of reducing B_{max} . In the experiment, the length of the 56 wt% Tb fiber was set to 2 cm to act as a point sensor. The factor I/I_0 is limited by the laser source noise. If the noise is assumed to around 1%, the minimum measurable magnetic field is 0.02 T. This number can be substantially reduced by providing a reference measurement for the laser source, eliminating the intensity fluctuations of the source from the measurements. In this case, detection at the nW level (with I_0 at the mW level) yields a sensor resolution of 2×10^{-6} T. If higher resolution and higher B_{max} are both required, two all-fiber magnetic field sensors could be co-located. In this scenario, one sensor would have a large VL product to obtain the desired resolution; the other would have a small VL product to obtain the desired maximum detected magnetic field by removing the ambiguity of the other sensor.

The Verdet constant of the Tb fiber depends on temperature; for example, $(1/V)dV/dT$ is around $10^{-4} /K$ for silica[119]. To mitigate the impact of temperature on measurement results, for example, in an environment with temperature fluctuations, a fiber-grating temperature sensor could be cascaded or co-located

with the magnetic field sensor to monitor the temperature near the magnetic field sensor. In this way, the sensor could give accurate results, providing the device has been calibrated as a function of temperature. If the sensor is used in a controllable laboratory environment, there is no need for a temperature sensor.

Although the resolution of this intensity-based sensor cannot exceed that of interference-based sensors, this all-fiber magnetic-field sensor is suitable for environments containing strong electromagnetic fields, such as nuclear facilities, magnetic resonance imaging (MRI), magnetic levitation (e.g., high-speed trains) and some military harsh environments. For example, the maximum magnetic field strength in MRI systems is around 3 T, which is a good match with this sensor. Apart from the sensing element (i.e. the Tb-doped fiber), the rest of the proposed sensing system is silica fiber, which is immune to perturbations by electromagnetic fields, unlike electronic-based sensors. The proposed sensor is compact and robust compared with bulk optics-based sensors. Additionally, it has a simple structure and does not need material coatings, which will result in a low-cost device.

Since the all-fiber magnetic field sensor can only measure magnetic fields parallel to its axis, three orthogonally oriented sensors could be combined to provide a complete three-dimensional magnetic field sensor. However, in most cases, an applied magnetic field is to be measured requiring only a single axis sensor.

In conclusion, an all-fiber optical magnetic field sensor has been demonstrated. It consisted of a fiber Faraday rotator and a fiber polarizer. The fiber Faraday rotator used a 2-cm-long section of 56-wt%-terbium-doped silica fiber with a Verdet constant of $-24.5 \text{ rad}/(\text{Tm})$ at 1053 nm. The fiber polarizer was Corning SP1060 single-polarization fiber. The sensor had a sensitivity of $0.49 \text{ rad}/\text{T}$ and can measure magnetic fields from 0.02 T to 3.2 T. This work has been published in reference [120].

Chapter 6

All-Fiber Wavelength-Tunable Continuous-Wave Laser

6.1 Introduction

Wavelength-tunable lasers are desired in wavelength-scanning systems, such as optical coherent tomography (OCT), optical instrument testing systems, sensor array systems, and spectroscopy. They can reduce the inventory cost of fixed-wavelength lasers in multi-wavelength systems, such as WDM telecommunications. A wavelength-tunable fiber laser usually consists of a conventional fiber laser with an intra-cavity wavelength-tunable filter, as shown in Fig. 6.1. Various filters have been investigated in the last two decades. These filters include Fabry-Perot cavities[121], [122], [123], [124], free-space wavelength-selective gratings[125], [126], [127], [128], Mach-Zehnder filters[129], fiber couplers[130], liquid crystal mirrors[131], [132], MEMS[133], thin films[134], acousto-optic modulators[135], [136], multimode interferometers[137], fiber tapers[138] and fiber Bragg gratings [139], [140], [141], [142], [143]. Tuning ranges span several nm to tens of nm depending on which filter is used.

Although tunable diode lasers are small, robust, and low cost, tunable fiber lasers have narrower linewidth, lower noise floor, and are capable of much higher power levels. Among all the wavelength-tunable lasers mentioned above, only the fiber Bragg grating and the fiber taper filters are suitable for integrating into all-fiber lasers. The fiber Bragg grating and fiber taper are mechanically stretched to

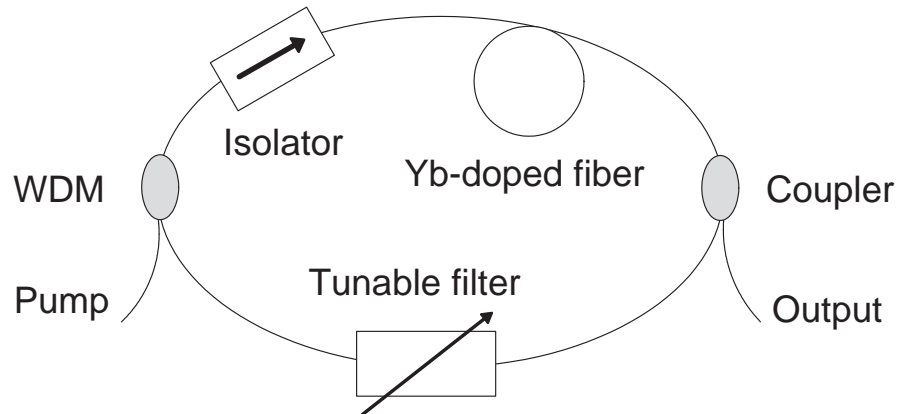


Figure 6.1: Configuration of a general wavelength-tunable fiber laser.

provide tunability over a 20-nm range. These tuning-methods suffer from mechanical fatigue, which prohibits their use in commercial systems.

In this chapter, a new tuning mechanism based on Faraday rotation is proposed. The tuning filter consists of a fiber polarizer and a fiber Faraday mirror that includes a fiber faraday rotator and a chirped fiber Bragg grating (CFBG). The CFBG is directly written on the terbium-doped fiber in the Faraday rotator. An all-fiber wavelength-tunable laser can be built by combining this filter with a linear laser cavity. Since the electromagnetic field is used for tuning, high tuning speeds can be achieved if a solenoid is used, while keeping the laser mechanically untouched. Such an arrangement allows for electrical tuning in an all-fiber laser without the long-term problems associated with mechanical fatigue.

6.2 Working Principle

The configuration of the all-fiber wavelength-tunable filter is shown in Fig. 6.2. It consists of a fiber polarizer and a special fiber Faraday mirror. The fiber Faraday mirror is different to the one shown in Sec. 5.1.5 in that a CFBG is directly written into the terbium fiber. It has been demonstrated that terbium-doped silicate fiber has photosensitivity after hydrogen loading[144]. Therefore, it is possible to write a CFBG directly into the terbium fiber.

In the proposed filter, linearly polarized light, E_0 , is input into the fiber polarizer. The light polarization is rotated in the Tb-doped fiber while being reflected

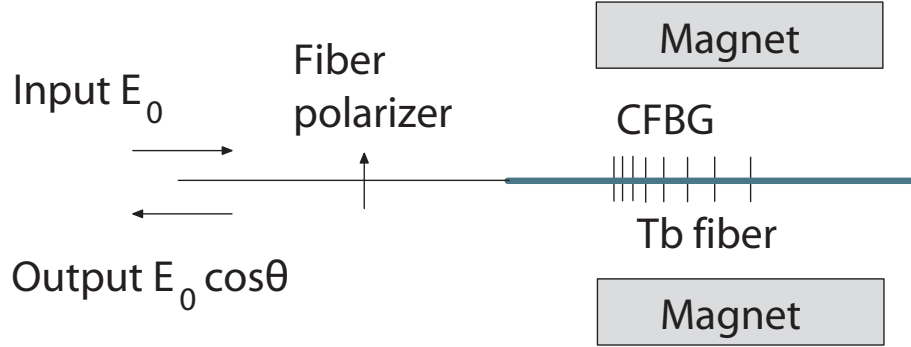


Figure 6.2: Configuration of the all-fiber wavelength-tunable filter.

by the CFBG. Since different wavelengths are reflected at different locations in the CFBG, they will propagate different lengths in the Tb fiber, and their polarizations will rotate different angles θ via the Faraday effect. The polarization rotation of different wavelengths are shown in Fig. 6.3. The Y direction is the passing direction of the fiber polarizer. The polarization angle with respect to the Y axis is θ . Only light with a polarization direction parallel to the fiber polarizer can pass through it. Suppose the CFBG can reflect wavelengths from λ_1 to λ_3 , where λ_2 is a wavelength in between them, i.e. $\lambda_1 < \lambda_2 < \lambda_3$. After the light is reflected back and goes through the fiber polarizer again, its amplitude becomes $E_0 \cos(\theta)$. The optical power loss, α , is $\alpha = -10 \log_{10} \cos^2(\theta)$. Fig. 5.5 shows that the rotation angle, θ , can vary from negative to positive, depending on the magnetic field distribution (i.e. the location or strength of the magnet). Therefore, it is possible to select a certain wavelength for which $\theta = 0$ by changing the magnetic field applied on the Tb:CFBG. Then only one wavelength has 0 dB loss and all other wavelengths have non-zero loss, as long as $-\pi/2 < \theta < \pi/2$ within the bandwidth of the gain medium.

In a laser cavity, the net gain $g_{net} = g - \alpha$ determines which wavelength will resonate, where g is the gain of the gain medium. α has a small dispersion due to the \cos^2 dependence, while g has a large dispersion due to the ytterbium emission bandwidth. This large discrepancy in the dispersions make such a laser difficult to tune. Fig. 6.4 shows the experimental configuration used to measure the Yb-doped-fiber gain spectrum. A 5-m length of PM Yb-doped fiber is spliced with a 976/1030 nm WDM. The pump is input from the 976 nm port, and the spectrum is

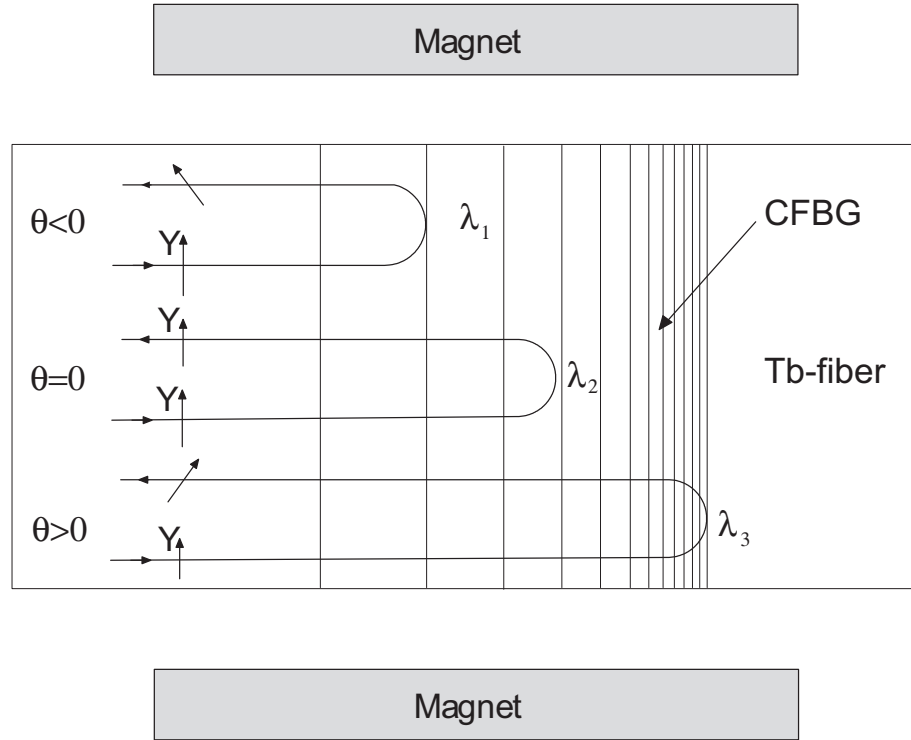


Figure 6.3: Rotation of polarization states of different wavelengths in the all-fiber filter.

measured through the 1030 nm port on an optical spectrum analyzer (OSA). Fig. 6.5 shows the gain spectrum of this Yb fiber at different pump currents. There are no flat regions that are required for our dispersion tuning mechanism.

To solve this problem, the gain can be flattened using a fused-fiber WDM, whose transmission spectrum can be approximated as a cosine-squared function[145]. Fig. 6.6 shows the experimental configuration used to flatten the Yb-doped fiber gain spectrum. The difference from Fig. 6.4 is that a 1030/1090 nm WDM is inserted as a filter into the cavity. The 1090 nm port is used as transmission port and the 1030 nm port is unused. Fig. 6.7 shows the gain-flattened spectrum of the 5-m long PM Yb fiber together with this 1030/1090 nm WDM at 200 mA pump current. Since WDMs exhibit a cosine-squared transmission, the 1090 nm port also was a transmission port at the 976 nm pump wavelength, allowing nearly all of the pump power to pass through to the Yb-doped fiber. The resulting net gain is flattened to less than 0.2 dB from 1047-1060 nm.

Fig. 6.8 shows the proposed configuration of the all-fiber wavelength-tunable

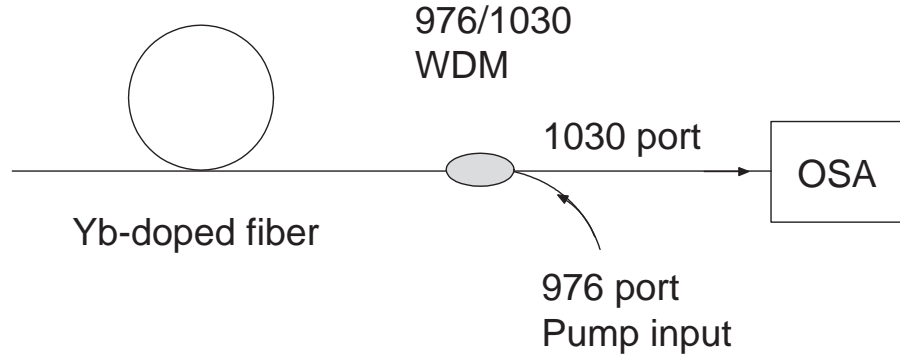


Figure 6.4: Experimental configuration to measure the Yb-doped fiber gain spectrum.

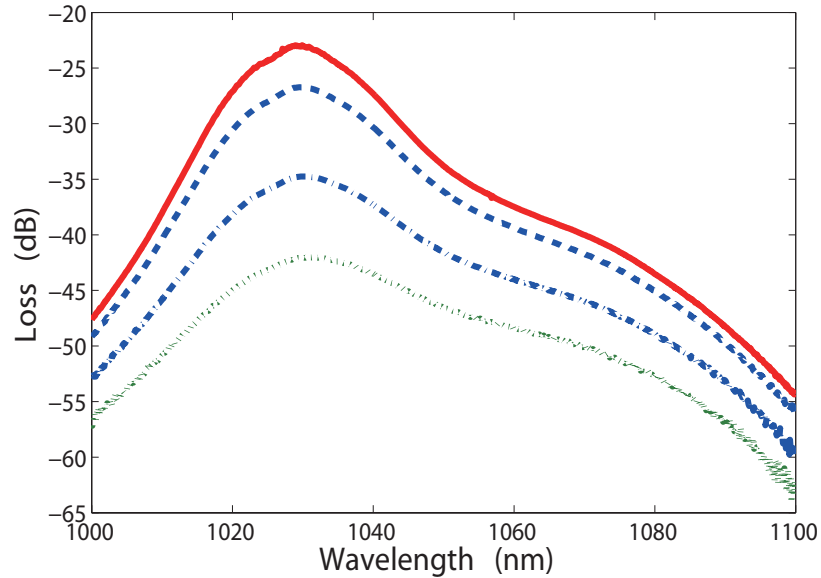


Figure 6.5: Measured ASE spectra of the Yb-doped fiber at different pump currents: 800 mA (solid), 300 mA (dashed), 150 mA (dashed-dot) and 100 mA (dot).

filter. The splice point between the PM and Tb fiber is defined as the zero point of the z axis, and z is the distance from the splice to the center of the magnet. The length of the CFBG is $z_2 = 2$ cm. The distance between the PM fiber and the CFBG is $z_1 = 5$ cm. Most of the polarization rotation occurs in this section of Tb-fiber. The CFBG does the final rotation, with the location (or strength) of the magnet determining the wavelength that is rotated a net zero degree.

Fig. 6.9 shows the proposed configuration of the all-fiber wavelength-tunable

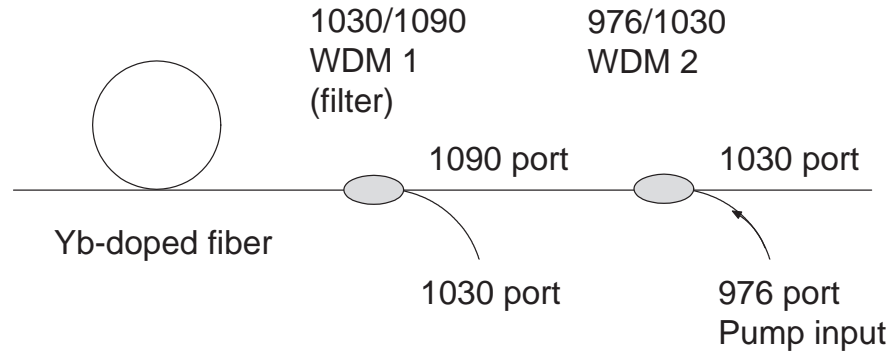


Figure 6.6: Experimental configuration used to flatten the Yb-doped fiber gain spectrum.

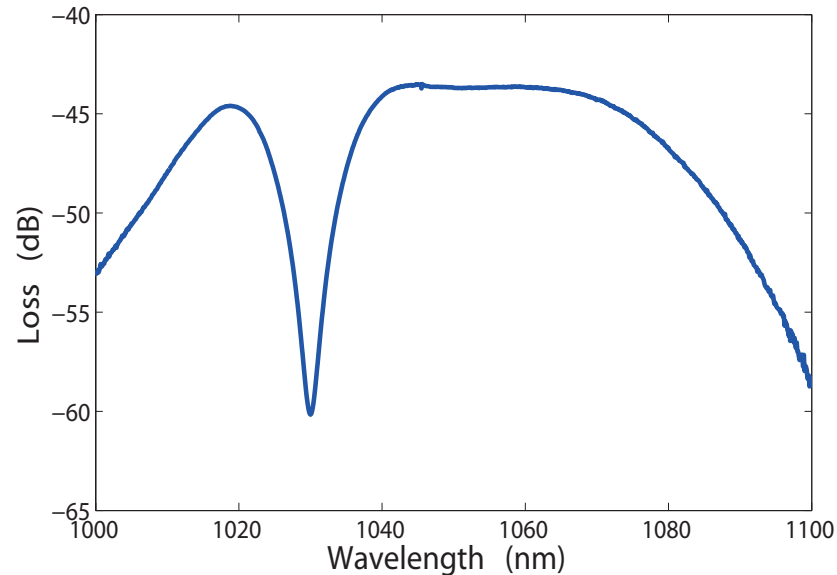


Figure 6.7: Gain-flattened ASE spectrum of the Yb-doped fiber at 200 mA pump current.

laser. The all-fiber reflective filter is used as one end mirror of the cavity. The 4% reflection at the cleaved output end is the other end mirror, although a partially reflective broadband FBG could also be used. A polarizing fiber or a CSG can be used for the fiber polarizer. If the magnet is translated along the fiber axis, the output wavelength of such a demonstration laser would be tuned correspondingly. The theoretical calculation of the wavelength tuning as a function of z axis (magnet position) is shown in Fig. 6.10. This calculation uses the flattened gain spectrum

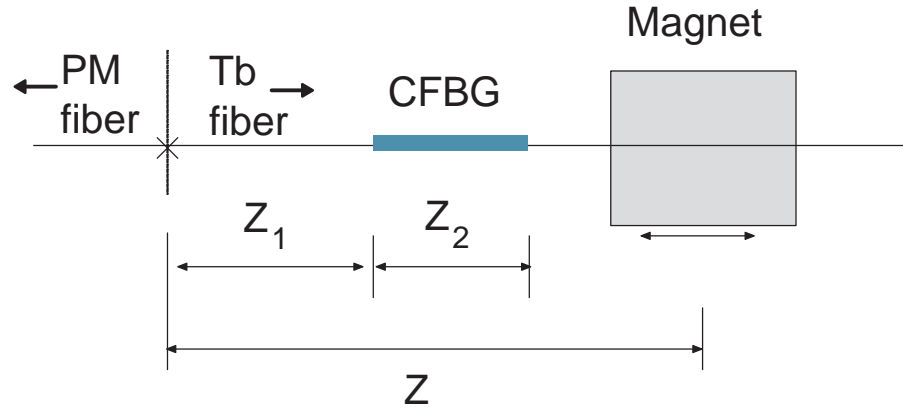


Figure 6.8: Experimental configuration of the reflective all-fiber wavelength-tunable filter using Tb fiber.

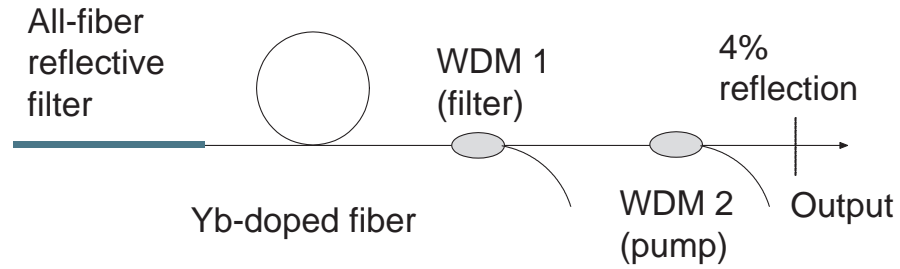


Figure 6.9: Experimental configuration of the all-fiber wavelength-tunable laser.

measured in Fig. 6.7 and the polarization rotation measured for the 65 wt.% Tb-doped fiber to calculate the wavelength with the maximum gain as a function of the magnet position. The CFBG is assumed to have a reflection bandwidth from 1047 to 1060 nm with a linear chirp. Fig. 6.10 shows that the wavelength can be linearly tuned by translating the magnet along the z axis. If a solenoid is used instead of a permanent magnet, this tuning can be accomplished electronically with no mechanical stress or moving parts.

6.3 Conclusion

In this chapter, an all-fiber wavelength-tunable fiber laser is proposed. The tuning filter consists of a fiber polarizer and a fiber Faraday mirror which includes a fiber Faraday rotator and a chirped fiber Bragg grating (CFBG). The CFBG is directly

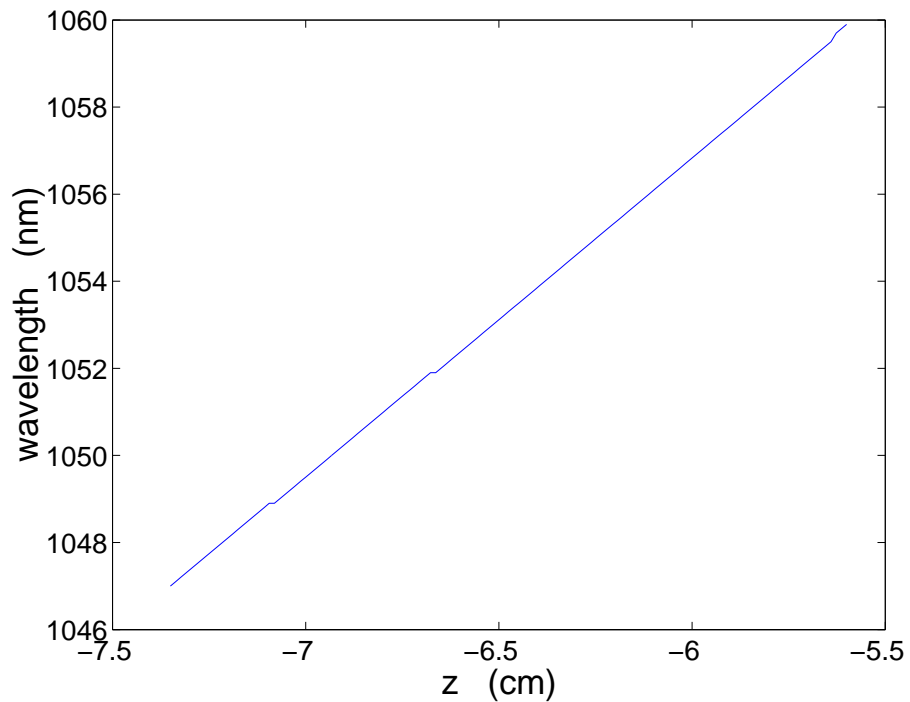


Figure 6.10: Theoretical calculation of the wavelength tuning as a function of the magnet location.

written on the terbium-doped fiber in the Faraday rotator. An all-fiber wavelength-tunable laser can be built by combining a linear laser cavity and this all-fiber tuning filter. Gain flattening is demonstrated, providing 13-nm of available tuning range. Calculations shows that linear tuning can be achieved over this range. Since the electromagnetic field is used for tuning, the all-fiber laser is free from stress and mechanical fatigue, and can be tuned at high speeds by using a solenoid.

Chapter 7

Filamentation Analysis in Large-Mode-Area Fiber Lasers

7.1 Introduction

Fiber lasers have developed rapidly in recent years[146], [147] with output powers above the kilowatt level[148], [149]. With increasing output power, nonlinear effects become important and can ultimately limit the power scalability in the fiber. Two well-known nonlinear effects that have limited the output power of fiber lasers are stimulated Brillouin scattering (SBS) and stimulated Raman scattering (SRS). As mentioned in Sec. 1.2, several methods can be used to increase the SBS threshold, including increasing the signal bandwidth to decrease the Brillouin gain[38], using new fiber designs to decrease the overlap between acoustic and optics modes[150], varying the temperature along the cavity[151], [152] and using low-numerical-aperture, large-mode-area (LMA) fibers[39]. Spectral filtering and LMA fibers are used to mitigate SRS. In LMA fibers, the large mode area decreases the optical intensity, therefore increasing the nonlinear threshold.

While many methods are being investigated to suppress SBS and SRS, other nonlinear effects have an impact, such as self-focusing. Self-focusing can lead to beam-quality degradation through a process called filamentation, which has been studied extensively in semiconductor lasers over the past two decades[153], [154], [155]. The physical nature of filamentation arises from self-focusing through the nonlinear refractive index. When the light intensity is strong enough for self-

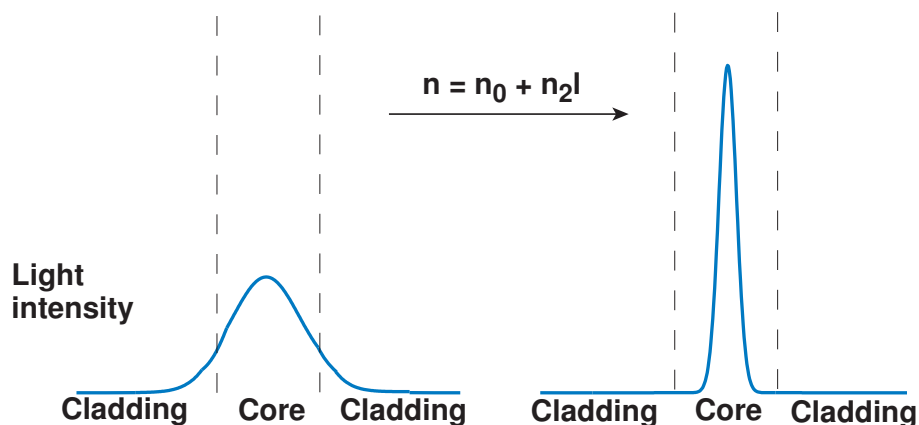


Figure 7.1: An intense laser beam is focused due to the nonlinear refractive index.

focusing to occur, the beam in the laser cavity is focused, as shown in Fig. 7.1. As a result, the laser beam is limited in a small region in the center of the core. In a semiconductor laser, the corresponding population inversion is depleted in the center of the core but undepleted in other areas of the core, i.e., spatial hole burning. With spontaneous emission occurring throughout the core, it is easy to generate other lasing beams, finally resulting in filamentation, as depicted in Fig. 7.2. Figure 7.3 shows an infrared image of the top of a broad-area gain region in a semiconductor laser, illustrating the effect of filamentation[156]. A similar effect could occur in optical fiber lasers. In 1987, Baldeck et al.[157], [158] observed the self-focusing effect in an optical fiber with picosecond laser pulses. Self-focusing has been studied in hollow waveguides[159], [48] and more recently in fiber amplifiers[160]. Although filamentation has not yet been observed in fiber lasers, a theoretical analysis that can predict its threshold in fiber lasers is lacking.

In this chapter, a theoretical model for filamentation in LMA fiber lasers is presented. Solving the paraxial wave equation and population rate equation in three dimensions, an expression for the filament gain is derived using a perturbation method. This expression includes both spatial and temporal characteristics, the filament spacing, and the oscillation frequency. The filament gain also depends on the physical parameters of the optical fiber, the nonlinear refractive index, the pump power, and the signal power. This model can predict the output-power thresholds at which the filamentation will occur for a given set of optical fiber parameters, in particular the core diameter. A simplified threshold expression is

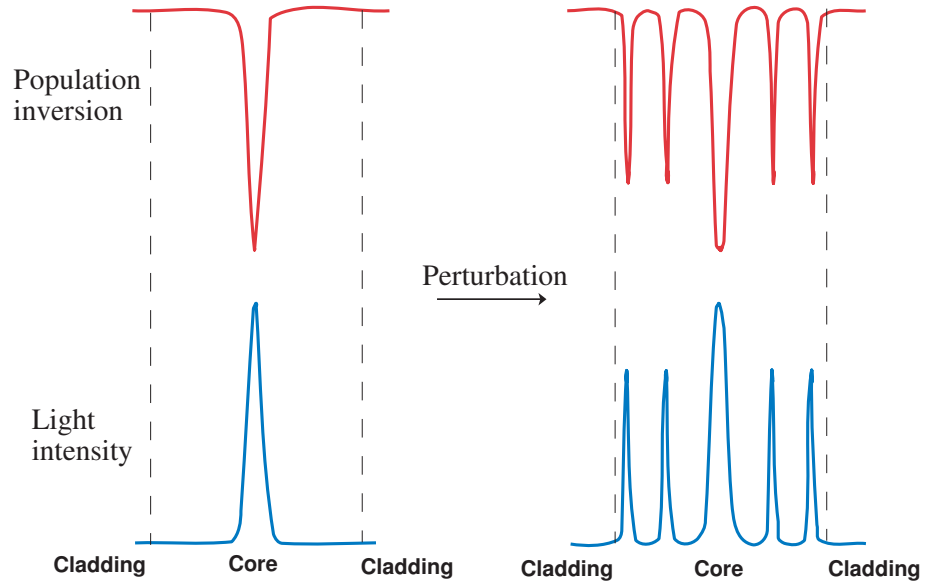


Figure 7.2: Filamentation is induced by perturbations in a self-focused beam condition.

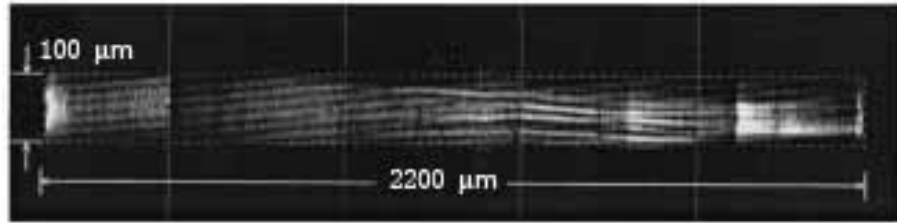


Figure 7.3: Infrared image of the top of a broad-area gain region in a semiconductor laser, illustrating the effect of filamentation[156]

provided. The results are shown to be consistent with previous experiments and models.

7.2 Theoretical Model and Steady-State Solution

Starting with Maxwell's equations in a dielectric medium, a wave equation is obtained, assuming an optical field of the form $\tilde{A} = A_s(r, \phi, z, t)e^{i(kz - \omega t)}$, and using the slowly varying envelope approximation to neglect the second derivatives of time t and axial coordinate z . After considering the gain, loss, nonlinear refractive

index, and the coupling of pump and signal light in the optical fiber, the optical field of the signal light satisfies the paraxial wave equation

$$\frac{\partial A_s}{\partial z} + \frac{1}{v_g} \frac{\partial A_s}{\partial t} = \frac{i}{2k_s} \nabla_T^2 A_s + \left[\frac{1}{2} g'_s + i(2\gamma_p P_p + \gamma_s P_s) \right] A_s, \quad (7.1)$$

where A_s is the slowly varying amplitude of the signal light along z and t , v_g is the group velocity, $k_s = n_{eff} k_0$ is the mode propagation constant of the signal light, n_{eff} is the effective index of the refraction, and k_0 is the free-space propagation constant. $\nabla_T^2 = \frac{1}{r} \frac{\partial}{\partial r} + \frac{\partial^2}{\partial r^2} + \frac{1}{r^2} \frac{\partial^2}{\partial \phi^2}$ is the transverse Laplacian operator, representing diffraction. $g'_s = g_s - \alpha_{cav}$ is the net gain of the signal light, where $g_s = N_2 \sigma_s^e - N_1 \sigma_s^a$ is the local gain of the signal light. The energy-level system of the excitation ions is assumed to be two-level system[161], where N_2 , N_1 are the upper and lower state population densities, respectively. σ_j^a , σ_j^e are the absorption and emission cross sections at the frequency ω_j with $j = p, s$ representing pump and signal light. To analyze the optical fiber laser, the mirror losses are distributed throughout the cavity, $\alpha_{cav} = \alpha_{int} - \ln(R_1 R_2)/2L$, where α_{int} is the internal loss, L is the cavity length, and R_1 and R_2 are the reflectivities of the mirrors. For the case of a fiber amplifier, the cavity loss is the same as the internal loss, $\alpha_{cav} = \alpha_{int}$. $\gamma_j = \bar{n}_2 k_0 / A_{effj}$ is the nonlinear parameter at frequency ω_j , \bar{n}_2 is the Kerr coefficient, and A_{effj} is the effective cross section area at frequency ω_j . The nonlinear parameter γ_j represents self-focusing in optical fibers, for $\gamma_j > 0$, $P_j = |A_j|^2$ is the optical power in the core at frequency ω_j .

With the assumption of a two-level system, the rate equation of the excited state is given by[161]

$$\frac{\partial N_2}{\partial t} = -\frac{N_2}{\tau} - (N_2 \sigma_s^e - N_1 \sigma_s^a) \phi_s - (N_2 \sigma_p^e - N_1 \sigma_p^a) \phi_p, \quad (7.2)$$

where $\phi_j = P_j / (A_{effj} h \nu_j)$ is the photon flux at the frequency ν_j , τ is the spontaneous lifetime of the excited state, and $N_t = N_1 + N_2$ is the total population density.

Eq. 7.1. is a nonlinear equation without an exact solution. The waveguide mode is first solved in the absence of gain and loss for low intensity levels (i.e. no

nonlinear effects). The solution in the core can be found[78]

$$\tilde{A} = A_s \exp[i(k_s z - \omega_s t)] = A_{s_0} J_m(p_s r) \exp(im\phi) \exp[i(k_s z - \omega_s t)], \quad (7.3)$$

where A_{s_0} is a constant, $p_s^2 = n_1^2 k_0^2 - k_s^2$, and n_1 is the refractive index in the core. The index m can only take integer values, with $m = 0$ for fundamental mode. The optical field in the Eq. 7.1. should have the form $A_s = A_{s1}(z) J_m(p_s r) \exp(im\phi)$. Substituting the Laplacian term with $\nabla_T^2 A_s = -p_s^2 A_s$, Eq. 7.1. can be rewritten in the steady state as

$$\frac{\partial A_s}{\partial z} = \left[\frac{1}{2} g'_s - \frac{i p_s^2}{2 k_s} + i(2\gamma_p P_p + \gamma_s P_s) \right] A_s. \quad (7.4)$$

For simplicity, bi-directional pumping is assumed, so the pump power P_p can be regarded as nearly constant along the cavity, which leads to a constant gain along the cavity. When a laser is above threshold, the gain is clamped to the value of cavity loss at threshold. Since the loss is distributed along the cavity in this unfolded cavity model[155], the net gain, g'_s , is zero and the signal power $P_s = |A_s|^2$ must therefore be independent of z ($|A_{s1}(z)| = A_{s0}$). The solution of Eq. 7.4. has the form $A_s = A_{s0} J_m(p_s r) \exp(im\phi) \exp(i\Delta k_s z)$, where Δk_s is given by

$$\Delta k_s = \frac{1}{2} g'_s - \frac{i p_s^2}{2 k_s} + i(2\gamma_p P_p + \gamma_s P_s). \quad (7.5)$$

Eq. 7.5. shows the change of the complex propagation constant due to the gain, loss, nonlinearity and the waveguide mode.

The modal gain $g_s = \Gamma_s g$ includes the transverse confinement factor $\Gamma_s = \frac{A_{effs}}{A_{core}}$ to account for the fact that excited ions are doped only in the core. Substituting the relation $N_1 = N_t - N_2$ into Eq. 7.2, the upper state population can be found in the steady state as

$$N_2 = \frac{N_t \left(\frac{\sigma_s^a}{\sigma_s^e + \sigma_s^a} \frac{P_s}{P_s^{sat}} + \frac{\sigma_p^a}{\sigma_p^e + \sigma_p^a} \frac{P_p}{P_p^{sat}} \right)}{1 + \frac{P_s}{P_s^{sat}} + \frac{P_p}{P_p^{sat}}}, \quad (7.6)$$

where $P_j = |A_j|^2$, $P_j^{sat} = \frac{A_{effj} h \nu_j}{(\sigma_j^e + \sigma_j^a) \tau}$ is defined as saturation power with $j = p, s$. For the case of the fiber laser, with the threshold condition of $g_s = \alpha_{cav}$ and

the assumption of constant pump power, the signal power is constant along the z direction in the cavity as determined by Eq. 7.6,

$$P_s = \left[- \left(N_t \sigma_s^a + \frac{\alpha_{cav}}{\Gamma_s} \right) - \left(\frac{N_t (\sigma_p^e \sigma_s^a - \sigma_p^a \sigma_s^e)}{\sigma_p^e + \sigma_p^a} + \frac{\alpha_{cav}}{\Gamma_s} \right) \frac{P_p}{P_s^{sat}} \right] \frac{\alpha_{cav} P_s^{sat}}{\Gamma_s}. \quad (7.7)$$

7.3 Linear Stability Analysis and Filament Gain

The stability of the single-mode solution against nonlinear spatial perturbations must be determined under what condition beam filamentation will occur. If small perturbations grow with propagation, then the steady state solution is unstable, and the beam can break up under propagation through the fiber. Small perturbations a and n are introduced in the optical field $A_s = [\sqrt{P_s} + a(r, \phi, z, t)] \exp(i\Delta k_s z)$ and upper state population density $N_2' = N_2 + n(r, \phi, z, t)$. Linearizing Eqs. 7.1 and 7.2 in a and n , while using the steady-state solutions, leads to two coupled linear equations,

$$\frac{\partial a}{\partial z} + \frac{1}{v_g} \frac{\partial a}{\partial t} = \frac{i}{2k_s} (p_s^2 a + \nabla_T^2 a) + \frac{1}{2} g_s' a \quad (7.8)$$

$$+ \frac{1}{2} \Gamma_s n \sqrt{P_s} (\sigma_s^e + \sigma_s^a) + i\gamma_s P_s (a + a^*), \text{ and}$$

$$-\tau \frac{\partial n}{\partial t} = n \left(1 + \frac{P_s}{P_s^{sat}} + \frac{P_p}{P_p^{sat}} \right) + \left(N_2 - N_t \frac{\sigma_s^a}{\sigma_s^e + \sigma_s^a} \right) \frac{\sqrt{P_s}}{P_s^{sat}} (a + a^*). \quad (7.9)$$

Due to the cylindrical geometry, the perturbation is assumed to have the form of Bessel solution,

$$a = a_1 J_{k_\phi}(pr) \exp[i(k_\phi \phi + k_z z - \Omega t)] \quad (7.10)$$

$$+ a_2 J_{k_\phi}(pr) \exp[-i(k_\phi \phi + k_z z - \Omega t)]$$

$$n = n_0 J_{k_\phi}(pr) \exp[i(k_\phi \phi + k_z z - \Omega t)] \quad (7.11)$$

$$+ n_0^* J_{k_\phi}(pr) \exp[-i(k_\phi \phi + k_z z - \Omega t)],$$

where p is a Bessel parameter and k_ϕ has integer value. k_z is the propagation constant of the perturbation and Ω is its oscillation frequency. n_0 , a_1 and a_2 are

constants. The two field perturbation parameters originate from the fact that a represents a complex field, which is determined by two independent variables[162]. The perturbation in population density, n , is a real number, which can be determined by one variable. Substituting Eqs. 7.10 and 7.11 into the coupled equations leads to linear equations about a_1 and a_2^* . In the condition that they have nontrivial solutions, k_z needs to satisfy

$$k_z = \frac{\Omega}{v_g} + i\frac{1}{2}[G(1 + i\xi) - g'_s] \pm \sqrt{\frac{p'^2}{2k_s} \left(\frac{p'^2}{2k_s} - 2\gamma_s P_s \right) - \frac{1}{4}[G^2(1 + i\xi)^2 + g_s'^2]}, \quad (7.12)$$

where $p'^2 = p^2 - p_s^2$. The factor ξ and the saturated power gain G are defined respectively as

$$\xi = \frac{\Omega\tau}{1 + \frac{P_s}{P_{sat}} + \frac{P_p}{P_{sat}}}, \text{ and} \quad (7.13)$$

$$G = \Gamma_s g'_s \frac{\frac{P_s}{P_{sat}} \left(1 + \frac{P_s}{P_{sat}} + \frac{P_p}{P_{sat}} \right)}{\left(1 + \frac{P_s}{P_{sat}} + \frac{P_p}{P_{sat}} \right)^2 + (\Omega\tau)^2}. \quad (7.14)$$

The steady state solution is stable provided the perturbation gain (which is the imaginary part of the k_z) is less than the cavity loss, a reflection of the growth of the laser field in the cavity. With the relation $g = -2Im(k_z)$, the perturbation gain can be extracted from Eq. 7.14, where the factor 2 is added to define the power gain,

$$g = Re \sqrt{\frac{2p'^2}{k_s} \left(2\gamma_s P_s - \frac{p'^2}{2k_s} \right) + [G^2(1 + i\xi)^2 + g_s'^2]} - (G - g'_s). \quad (7.15)$$

The negative root from Eq. 7.12. is selected because the gain needs to be positive for filamentation to occur. Eq. 7.15. gives a general expression for the filament gain. In a fiber laser, when the population inversion is clamped to the threshold, the net gain g'_s is zero. The filament spacing is defined as $w = \pi/p$, with an oscillation frequency, $f = |\Omega|/2\pi$.

It is proposed that the solution of perturbation must have the form of Bessel solution due to the cylindrical geometry of the fiber. Because the perturbation is an electromagnetic field, it needs to satisfy the boundary condition on the inter-

face between the core and cladding, which means for every k_ϕ the Bessel parameter p or filament spacing w only has discrete values. In another words, the perturbation has mode structure that is similar to the well-known mode properties of the electromagnetic field in fibers. The filament gain shown in Eq. 7.15. has no dependence of k_ϕ because all terms in k_ϕ cancel out during the derivation. But that does not imply that all the modes can resonate. Mathematically, lower order modes, especially fundamental mode of the perturbation do not have dense enough mode structure for filamentation to occur. Physically, the largest amplitude of the fundamental mode is in the center of the core, where the population is depleted. The amplitudes of higher order modes are zero at center and large at margin where the population is undepleted. Therefore higher order modes of perturbation are more likely to occur than lower order modes. The peak-to-peak period of squared higher order Bessel solutions approximately equals to π , which accounts for the factor π in the definition of filament spacing. The squared second-order Bessel solution J_2^2 and peak-to-peak period w are shown in Fig. 7.4.

7.4 Spatio-Temporal Analysis of Filament Gain in Optical Fiber Laser

Most high-power fiber lasers are Yb-doped due to high quantum efficiency, high doping density, the absence of excited-state absorption, and a long upper-state lifetime. Therefore the parameters used in this section, shown in Table 7.1, are for typical Yb-doped fiber lasers. Since high-beam-quality fiber lasers are of the most practical interest, the analysis focuses on the destabilization of single-mode operation by filamentation; the steady-state solution is assumed to be the fundamental fiber mode.

Fig. 7.5. shows a 3-D plot of normalized filament gain v.s. normalized filament spacing and oscillation frequency for the signal peak power $P_s = 10 \text{ kW}$ and core diameter $d_{core} = 100 \text{ }\mu\text{m}$. The figure is symmetric in frequency space, therefore only the positive frequency is plotted. To facilitate understanding of the figure, normalized gain $g_{norm} = g/\alpha_{cav}$ and normalized filament spacing $w_{norm} = w/a_{core}$ are used, where a_{core} is the radius of the fiber core. If perturbation gain is larger

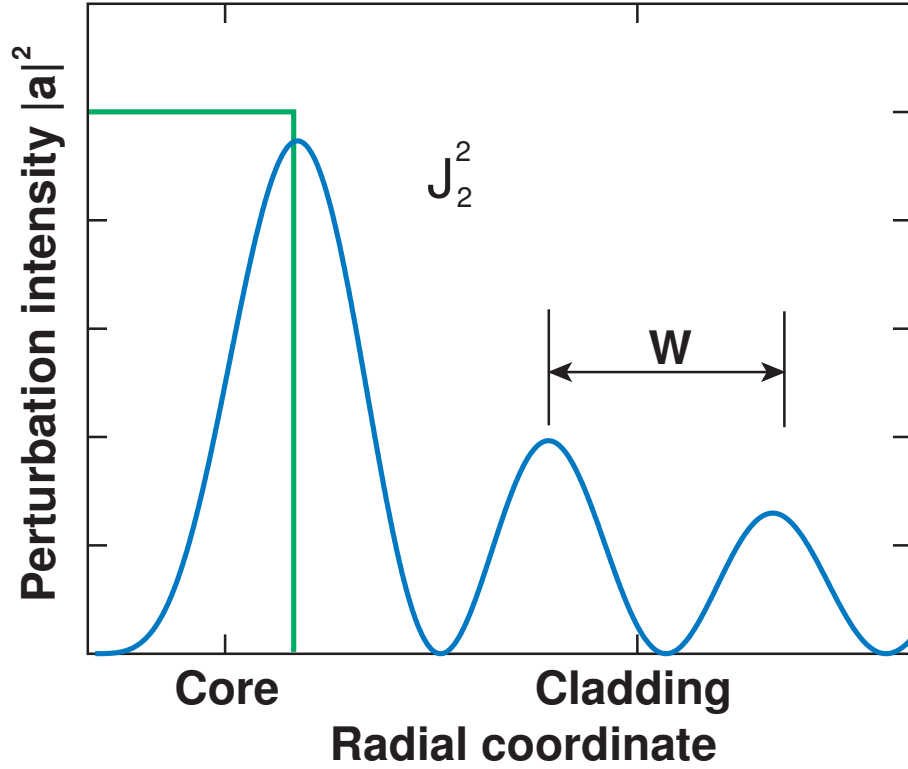
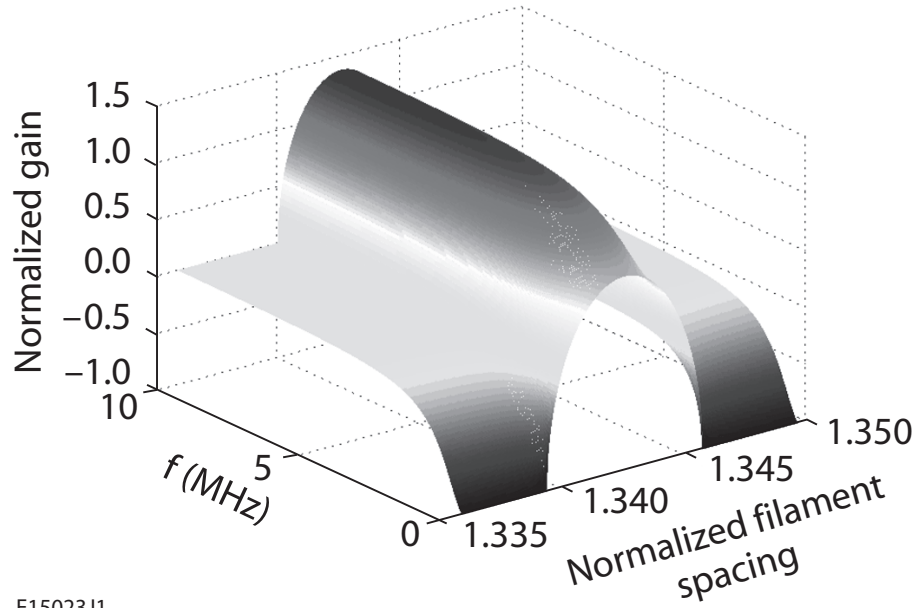


Figure 7.4: The squared second-order Bessel solution J_2^2 as a function of fiber radius.

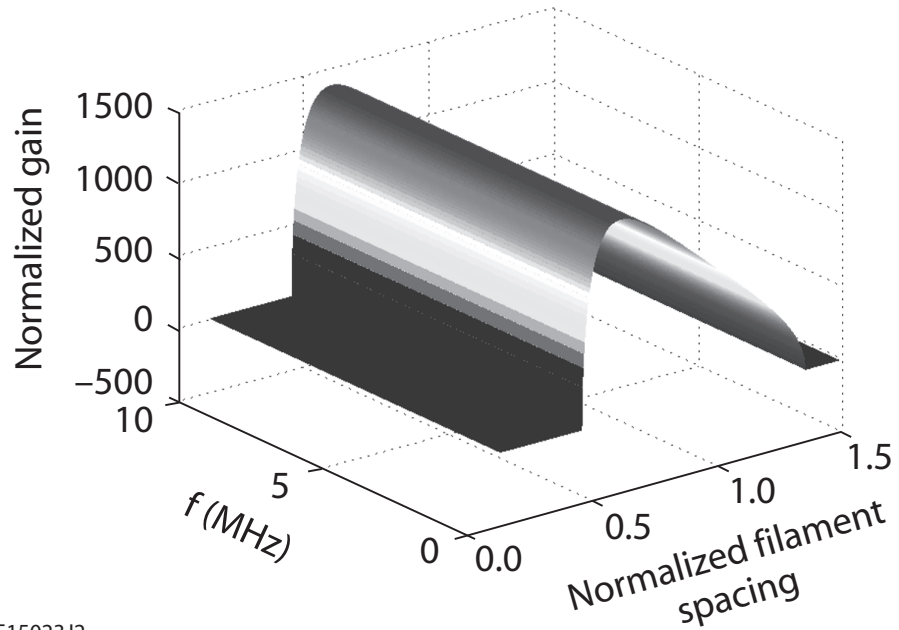
Table 7.1: Parameters for ytterbium-doped fiber laser calculations.

Parameter	Value
λ_p	$0.976 \mu m$
λ_s	$1.053 \mu m$
σ_p^a	$2476 \times 10^{-27} m^2$
σ_p^e	$2483 \times 10^{-27} m^2$
σ_s^a	$20.65 \times 10^{-27} m^2$
σ_s^e	$343.0 \times 10^{-27} m^2$
N_t	$9.4 \times 10^{24} m^{-3}$
τ	$0.84 ms$
Γ_p	0.01
n_{core}	1.46
n_{clad}	1.45562
\bar{n}_2	$2.6 \times 10^{-20} m^2/W$
R_1	1
R_2	0.5
L	$0.5 m$
α_{int}	$0.003 m^{-1}$



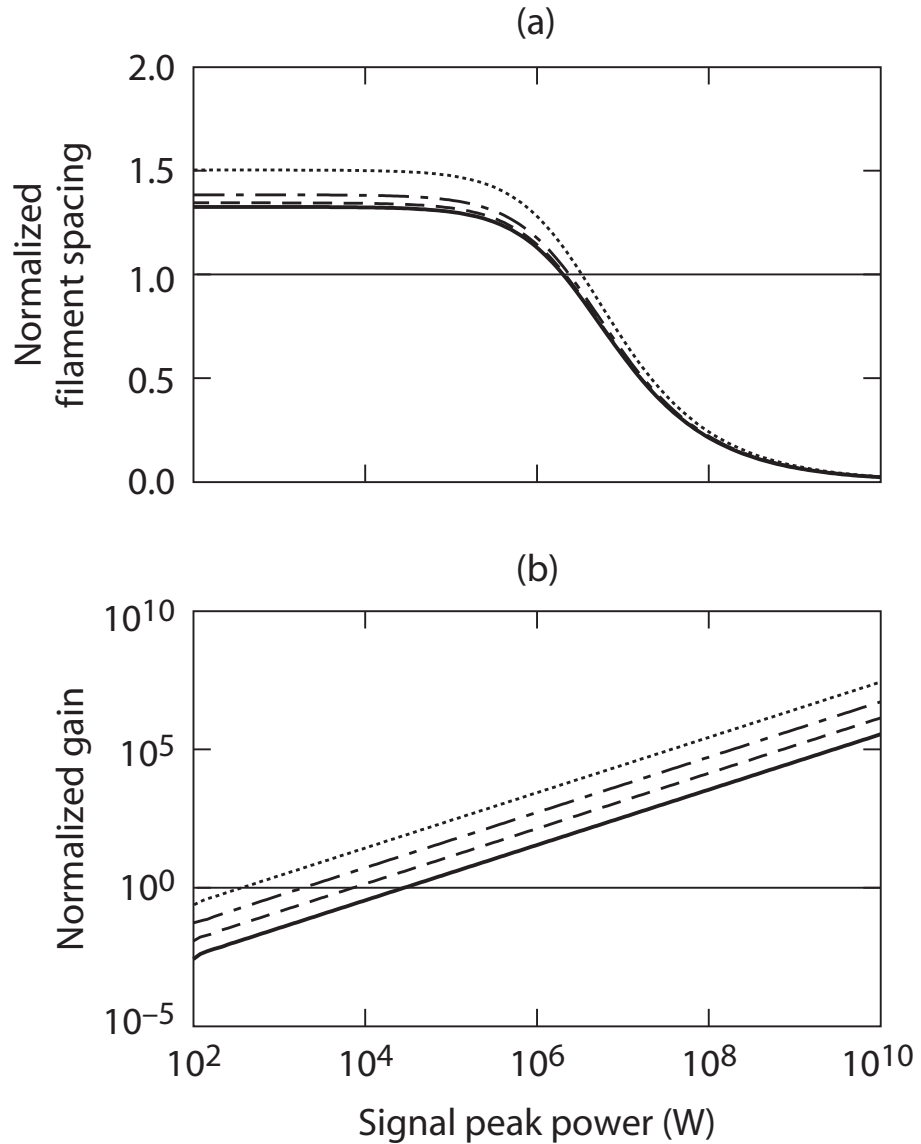
E15023J1

Figure 7.5: Normalized filament gain versus normalized filament spacing and frequency for $d_{core} = 100 \mu m$, $P_s = 10 \text{ KW}$.



E15023J2

Figure 7.6: Normalized filament gain versus normalized filament spacing and frequency for $d_{core} = 100 \mu m$, $P_s = 10 \text{ MW}$.



E15024J1

Figure 7.7: (a) Normalized filament spacing and (b) normalized gain as a function of the signal peak power for various core diameters: 20 μm (dotted), 50 μm (dashed-dotted), 100 μm (dashed) and 200 μm (solid) ($f = 10 \text{ GHz}$).

than cavity loss ($g_{norm} > 1$), the filament can grow in the cavity; if filament spacing is less than core radius ($w_{norm} < 1$), a filament can appear in the core. Both of these conditions need to be satisfied for a filament to occur, since the gain only exists within the fiber core. In Fig. 7.5 there is a peak in the spatial dimension that defines the filament spacing at which the perturbation will grow most rapidly,

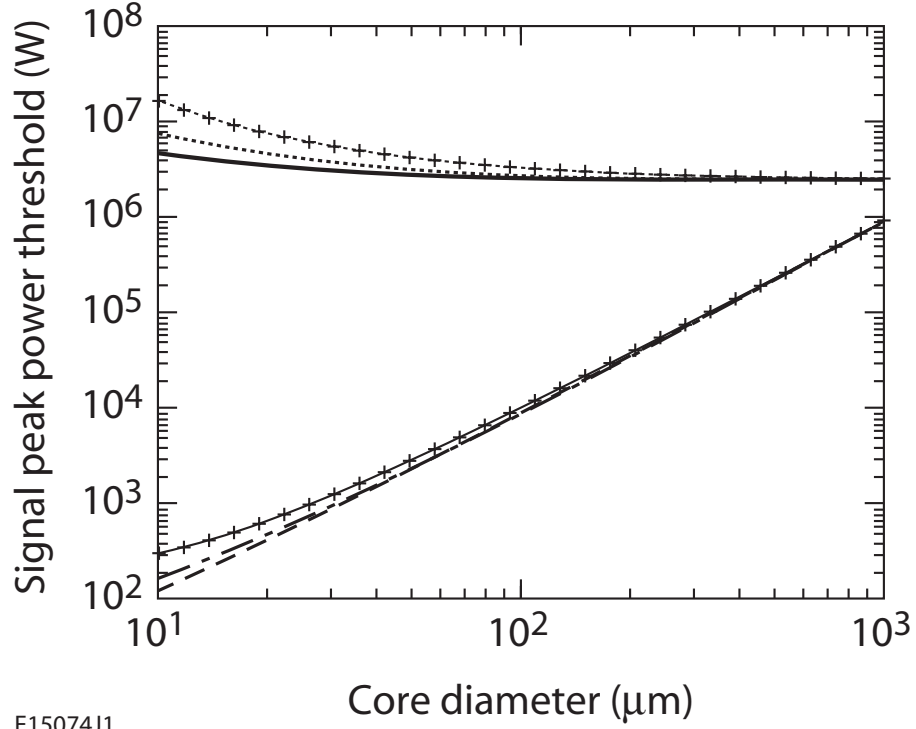
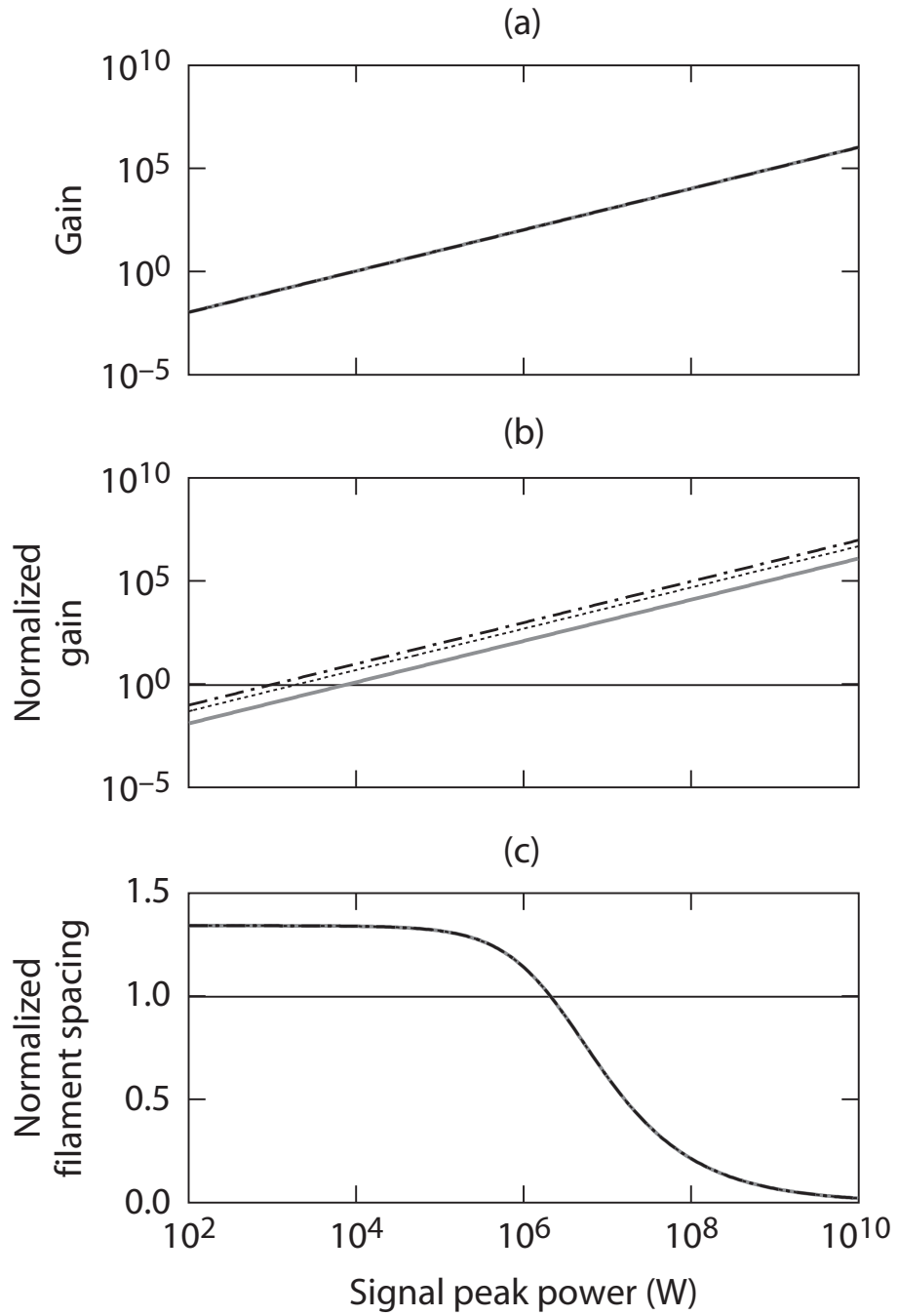


Figure 7.8: Gain threshold power [NA=0.2 (dashed), NA=0.1 (dashed-dotted), and NA=0.05 (solid with "+" symbol)] and spatial threshold power [NA=0.2 (solid), NA=0.1 (dotted), and NA=0.05 (dotted with "+" symbol)] as functions of core diameter for three numerical apertures ($f = 10 \text{ GHz}$).

where $g > \alpha_{cav}$. The normalized filament spacing corresponding to the peak region is larger than unity, which means the filament is outside the core, and filamentation can not occur. In the temporal dimension, the curve is constant with a dip at low frequencies. Since the noise perturbation is dynamic, there is less possibility for filament to growth statically or in low frequency.

In Fig. 7.6., the signal peak power P_s is increased to 10 MW. The gain peak becomes much larger, and the corresponding filament spacing falls into the core. Because both the thresholds are reached ($g_{norm} > 1$ and $w_{norm} < 1$), filamentation can occur. There is no observable feature in the temporal dimension. Thus for signal peak power high above the gain threshold, the temporal modulation of the filamentation can occur at any frequency.

Fig. 7.7. shows normalized filament spacing and normalized filament gain corresponding to the gain peak as a function of signal peak power for the core



E15405J1

Figure 7.9: (a) non-normalized (b) normalized filament gain and (c) normalized filament spacing as a function of the signal peak power for three different cavity length: 0.5 m (solid), 2 m (dotted) and 4 m (dashed-dotted) ($d_{core} = 100 \mu m$, $f = 10 GHz$).

diameters ranging from 20 μm to 200 μm when $f = 10 \text{ GHz}$. With the increase of the signal peak power, the filament gain peak will move towards the small filament spacing and the filament gain will increase. This agrees with conventional understanding: the higher the power, the denser the filaments and the larger possibility for filamentation to occur. From Fig. 7.7. the gain threshold for the filamentation to occur ($g = \alpha_{cav}$) can be determined. It is from magnitude of 100 W to 10 kW for core diameters ranging from 20 μm to 200 μm . The filament spacing threshold, however, is around a few MW, which then determines the filamentation threshold. Self-focusing and thus filamentation is only determined by the peak power(highest power) in fiber lasers, regardless of different average powers. Correspondingly, CW (continuous-wave) operation, is represented by the same curves in Fig. 7.7.

The gain peak with respect to the normalized filament spacing can be obtained by solving $\frac{\partial g}{\partial w} = 0$. Correspondingly, the filament spacing and signal peak power have the relation $\frac{\pi^2}{w^2} = 2\gamma_s k_s P_s + p_s^2$. At spatial threshold, $w = a_{core}$, the spatial threshold power is,

$$P_{th}^{spatial} = \frac{\frac{\pi^2}{a_{core}^2} - p_s^2}{2\gamma_s k_s}. \quad (7.16)$$

At high frequency, the saturation gain G and factor ξ can be neglected from Eq. 7.15, and the filament gain can be simplified at the gain peak as $g = 2\gamma_s P_s$. At gain threshold, $g = \alpha_{cav}$, the gain threshold power is

$$P_{th}^{gain} = \frac{\alpha_{cav}}{2\gamma_s}. \quad (7.17)$$

Figure 7.8 shows the spatial and gain threshold powers as a function of core diameter for three numerical apertures(NA). A smaller NA will reduce the waveguide confinement and result in a larger mode diameter. As would be expected from an intensity-dependent process, the gain threshold power increases when the core diameter (and thus mode diameter) increases and the NA decreases. Conversely, the spatial threshold power decreases with increasing core diameter and decreasing NA. For larger modes (larger core diameter and smaller NA), the effects of diffraction and waveguiding are weaker, and thus the mode becomes more susceptible to filamentation. For all core diameters below 1000 μm , the spatial threshold

dominates.

Figure 7.9 shows the normalized and non-normalized filament gain as a function of the signal peak power for three cavity lengths, from 0.5 m to 4 m when $d_{core} = 100 \mu m$ and $f = 10 GHz$. It is instructive to see that the normalized gain, changes with cavity length, since the cavity length relates to the cavity loss in the unfolded cavity model. The non-normalized gain is not affected by the fiber length since it only depends on the signal peak power. In the laser cavity, light propagates back and forth, and the optical path is effectively infinitely long. Thus filamentation can occur as long as the filament gain is larger than cavity loss and it does not depend on cavity length. Figure 7.9(c) shows the corresponding normalized filament spacing versus signal peak power. The filament spatial properties also do not change with cavity length, since they have the same transverse spatial structure. Because spatial threshold determines total threshold here, total threshold is independent of cavity length.

7.5 Discussion and Conclusion

Since perturbation theory is used in this paper, our model cannot be used to accurately describe the filament properties once they dominate the behavior of the system; however, the thresholds obtained in this paper can be compared to previous work. The self-focusing threshold power in bulk media has already been studied extensively[48],[30], and is given by

$$P_{cr} = \alpha \frac{\lambda^2}{4\pi n_0 \bar{n}_2}, \quad (7.18)$$

where n_0 is the refractive index in bulk media, and α is a constant, while Boyd[30] gives $\alpha \approx 1.8362$. Fibich and Gaeta[48] showed that α can range from 1.86225 to 6.58 for various beam profiles in bulk media and hollow waveguides, although α is close to the lower limit from their numerical simulations. Equation 7.16 shows that the threshold power can vary from 2 to more than 10 MW for different fiber diameters and numerical aperture, while Eq. 7.18 predicts a fixed threshold 4.4 MW regardless of fiber parameters. In the limit of an infinite waveguide, our theory can be used to model bulk media. As the core diameter increases, the

effective index of the fundamental mode approaches the core refractive index, and the mode approaches 100% confinement in the core. This latter condition can mathematically be written as $J_0(p_s a_{core}) = 0$. From this condition, the effective area of the mode, $A_{eff} = \pi r_0^2$ can be obtained by solving $J_0(p_s r_0) = 1/e$ where r_0 is the conventional definition of spot size. In this case, Eq. 7.16 simplifies to yield the exact form of Eq. 7.18 with $\alpha = 2.6188$. Not only does our theory simplify to the well known results for bulk media, but it yields excellent agreement with numerical value of α calculated for the J_0 Bessel beam profile[48].

However, for a fiber with a typical NA and core diameter approaching 1 mm, the filament threshold is around 2.6 MW, smaller than the self-focusing threshold predicted by the case of free-space propagation in bulk media(i.e Eq. 7.18 and simplified Eq. 7.16), due to the presence of the waveguide and material gain. Under such conditions, the light beam is confined mainly in the center of the core, leaving sufficient undepleted gain near the cladding that filamentation can occur before whole beam self-focusing. In the case of a small core diameter and a small NA, filamentation can not immediately appear in the core even after the occurrence of self-focusing, due to the weak waveguide confinement of higher-order filamentation modes. For this case, the filamentation threshold is much larger than the self-focusing threshold. In practice, LMA optical fibers are typically coiled to eliminate the higher-order modes from the output beam. This method increases the bend loss of the higher-order filamentation modes, increasing the filamentation threshold above 2.6 MW as is shown in Fig. 7.8.

The thresholds of SBS and SRS are around $\sim 30 W$ and $\sim 2.7 kW$ for short-length cw fiber lasers[151]. For short-pulse fiber lasers, SBS can be neglected due to the broad band spectral; the threshold of SRS can be increased to the MW level using the LMA fibers. Recently, Brooks[163] reported on a 4.5-MW-peak-power laser system using 100 μm core Yb-doped photonic crystal fibers with $M^2 = 1.3$. No filamentation occurs since this peak power is still under the filament spacing threshold (9.7 MW from our model). Given the rapid rate of progress in high-peak-power fiber lasers, self-focusing and filamentation will soon become a problem that needs to be addressed to retain high-beam-quality output. It is important to note that since these phenomena effectively increase the spatial frequency of the light in the fiber, bend loss will have a beneficial impact on the filamentation threshold.

In summary, an expression for filament power threshold was derived, using a perturbation method, starting from the paraxial wave equation. The spatial and temporal characteristics of the filament gain were analyzed. Two conditions must be satisfied simultaneously for filamentation to occur: the filament gain larger than cavity loss and filament spacing less than the core radius. The filamentation has the mode characteristics of optical fibers, and its threshold is on the order of a few MW depending on the parameters of the fiber. This work has been published in reference [164].

Chapter 8

Conclusion

Surface damage is one of the most problematic power limits in high-power fiber laser systems. All-fiber Faraday components are demonstrated as a solution to this problem, since they can be completely fusion-spliced into existing systems, eliminating all glass-air interfaces. Beam filamentation due to self-focusing places another limit on the peak power attainable from fiber laser systems. The limits imposed by this phenomenon are analyzed for the first time.

The concept of an effective Verdet constant is proposed and experimentally validated. The effective Verdet constant of light propagation in a fiber includes contributions from the materials in both the core and the cladding. It is measured in a 25-wt% terbium-doped-core phosphate fiber to be -6.2 rad/(Tm) at 1053 nm, which is six times larger than silica fiber. The result agrees well with Faraday rotation theory in optical fiber.

A compact all-fiber Faraday isolator and a Faraday mirror are demonstrated. At the core of each of these components is an all-fiber Faraday rotator made of a 4-cm-long, 65-wt%-terbium-doped silicate fiber. The effective Verdet constant of the terbium-doped fiber is measured to be -32 rad/(Tm), which is $27\times$ larger than that of silica fiber. This effective Verdet constant is the largest value measured to date in any fiber and is 83% of the Verdet constant of commercially available crystals used in bulk-optics-based isolators. Combining the all-fiber Faraday rotator with fiber polarizers results in a fully fusion-spliced all-fiber isolator whose isolation is measured to be 19 dB. Combining the all-fiber Faraday rotator with a fiber Bragg grating results in an all-fiber Faraday mirror that rotates the polarization state of

the reflected light by $88 \pm 4^\circ$.

An all-fiber optical magnetic field sensor is also demonstrated. It consists of a fiber Faraday rotator and a fiber polarizer. The fiber Faraday rotator uses a 2-cm-long section of 56-wt%-terbium-doped silicate fiber with a Verdet constant of -24.5 rad/(Tm) at 1053 nm. The fiber polarizer is Corning SP1060 single-polarization fiber. The sensor has a sensitivity of 0.49 rad/T and can measure magnetic fields from 0.02 to 3.2 T.

An all-fiber wavelength-tunable laser based on Faraday rotation is proposed. It consists of an all-fiber wavelength-tunable filter in a conventional fiber laser cavity. The filter includes a fiber polarizer and a fiber Faraday mirror in which a chirped fiber Bragg grating is directly written onto the 65-wt% terbium fiber. The ytterbium-doped fiber in the laser is gain flattened using a 1030/1090 nm WDM filter, resulting a net gain ripple that is measured to be less than 0.2 dB from 1047 to 1060 nm. The wavelength tuning range of the resulting fiber laser is therefore expected to be in this 1047 to 1060 nm range.

Filamentation is one of the nonlinear peak-power-threshold limits in high-power fiber lasers. Starting from the paraxial wave equation, an analytic expression for the filamentation threshold in fiber lasers is derived using a perturbation method. The occurrence of filamentation is determined by the larger of two thresholds, one of perturbative gain and one of spatial confinement. The threshold value is around a few megawatts, depending on the parameters of the fiber.

Bibliography

- [1] T. H. Maiman, “Optical and microwave-optical experiments in ruby,” *Phys. Rev. Lett.* **4**, 564–566 (1960).
- [2] J. Hecht, “Fiber lasers ramp up the power,” *Laser Focus World* **45**, 53–57 (2009).
- [3] W. Guan, “High-power single-frequency fiber lasers,” Dissertation, University of Rochester (2009).
- [4] H. Muller, V. R. J. Kirchhof, and S. Unger, “Fibers for high-power lasers and amplifiers,” *Comptes Rendus Physique* **7**, 154–162 (2006).
- [5] E. Snitzer, “Optical maser action of Nd^{3+} in a barium crown glass,” *Phys. Rev. Lett.* **7**, 444–446 (1961).
- [6] J. Stone and C. Burrus, “Neodymium-doped silica lasers in end-pumped fiber geometry,” *Appl. Phys. Lett.* **23**, 388 (1973).
- [7] R. J. Mears and L. Reekie and I. M. Jauncey and D. N. Payne, “Low-noise erbium-doped fiber amplifier operating at $1.54 \mu\text{m}$,” *Electron. Lett.* **23**, 1026–1028 (1987).
- [8] H. W. Etzel, H. W. Gandy, and R. J. Ginther, “Stimulated emission of infrared radiation from ytterbium-activated silica glass,” *Appl. Opt.* **1**, 534–536 (1962).
- [9] R. J. Mears, L. Reekie, S. B. Poole, D. N. Payne, “Neodymium-doped silica single-mode fibre lasers,” *Electron. Lett.* **21**, 738–740 (1985).
- [10] Y. Jeong, A. J. Boyland, J. K. Sahu, S. Chung, J. Nilsson, and D. N. Payne, “Multi-kilowatt single-mode ytterbium-doped large-core fiber laser,” *J. Opt. Soc. Korea* **13**, 416–422 (2009).
- [11] A. Giesen, H. Hugel, A. Voss, K. Wittig, U. Brauch, and H. Opower, “Scalable concept for diode-pumped high-power solid-state lasers,” *Applied Physics B: Lasers and Optics* **58**, 365–372 (1994).

- [12] E. Snitzer, H. Po, F. Hakimi, R. Tumminelli, and B. C. McCollum, "Double clad, offset core Nd fiber laser," in "Optical Fiber Sensors," (1988), 2, p. PD5.
- [13] H. Po, E. Snitzer, R. Tumminelli, L. Zenteno, F. Hakimi, N. M. Cho, and T. Haw, "Double clad high brightness Nd fiber laser pumped by GaAlAs phased array," in "Optical Fiber Communication Conference," (1989), 5, p. PD7.
- [14] H. Zellmer, "Leistungskalierung von faserlasern," Dissertation, University Hannover (1996).
- [15] H. Zellmer, A. Tunnermann, H. Welling, and V. Reichel, "Double-clad fiber laser with 30 W output power," in "Optical Amplifiers and Their Applications," (1997), 16, p. FAW18.
- [16] M. H. Muendel, "Optical fiber structure for efficient use of pump power", US-Patent US 5533163 (1996).
- [17] D. Digiovanni, "Method of making a cladding pumped fiber structure", US-Patent US 5873923 (1997).
- [18] D. Digiovanni, "Cladding-pumped fiber structures", US-Patent US 5949941 (1997).
- [19] R. Ifflander, *Solid-State Lasers for Materials Processing* (Springer-Verlag, 2001).
- [20] M. Karabulut, E. Melnik, R. Stefan, G. K. Marasinghe, C. S. Ray, C. R. Kurkjian, D. E. Day, "Mechanical and structural properties of phosphate glasses," *Journal of Non-Crystalline Solids* **288**, 8–17 (2001).
- [21] P. Polynkin, V. Temyanko, M. Mansuripur, and N. Peyghambarian, "Efficient and scalable side pumping scheme for short high-power optical fiber lasers and amplifiers," *IEEE Photon. Technol. Lett.* **16**, 204–206 (2004).
- [22] M. Poulain, "Fluoride glass fibers: applications and prospects," *Proc. SPIE* **3416**, 2 (1998).
- [23] M. J. F. Digonnet, *Rare-earth-doped Fiber Lasers and Amplifiers* (Marcel Dekker, 2001).
- [24] S. Ramachandran, J. M. Fini, M. Mermelstein, J. W. Nicholson, S. Ghalmi, M. F. Yan, "Ultra-large effective-area, higher-order mode fibers: a new strategy for high-power lasers," *Lasers & Photon. Rev.* **2**, 429 (2008).
- [25] J. P. Koplow, D. A. V. Kliner, and L. Goldberg, "Single-mode operation of a coiled multimode fiber amplifier," *Opt. Lett.* **25**, 442–444 (2000).

- [26] J. A. Alvarez-Chavez, A. B. Grudinin, J. Nilsson, P. W. Turner, and W. A. Clarkson, "Mode selection in high power cladding pumped fibre lasers with tapered section," in "Conference on Lasers and Electro-Optics," (1999), pp. 23–28.
- [27] R. A. Motes and R. W. Berdine, *Introduction to High Power Fiber Lasers* (Directed Energy Professional Society, 2009).
- [28] J. W. Dawson, M. J. Messerly, R. J. Beach, M. Y. Sherdin, E. A. Stappaerts, A. K. Sridharan, P. H. Pax, J. E. Heebner, C. W. Siders and C. P. J. Barty, "Analysis of the scalability of diffraction-limited fiber lasers and amplifiers to high average power," *Opt. Express* **16**, 13240–13266 (2008).
- [29] J. W. Dawson, M. J. Messerly, R. J. Beach, M. Y. Shverdin, A. K. Sridharan, P. H. Pax, J. E. Heebner, C. W. Siders, C. P. J. Barty, "Ultimate power limits of optical fibers," in "Optical Fiber Communication (OFC) Conference," (2010), p. OMO6.
- [30] R. W. Boyd, *Nonlinear Optics* (Academics press, 1992).
- [31] R. G. Smith, "Optical power handling capacity of low loss optical fibers as determined by stimulated Raman and Brillouin scattering," *Appl. Opt.* **11**, 2489–2494 (1972).
- [32] Y. Koyamada, S. Sato, S. Nakamura, H. Sotobayashi, and W. Chujo, "Simulating and designing Brillouin gain spectrum in single-mode fibers," *J. Lightwave Technol.* **22**, 631 (2004).
- [33] M. D. Mermelstein, M. J. Andrejeo, J. Fini, A. Yablon, C. Headley, D. J. DiGiovanni, and A. H. McCurdy, "11.2 dB SBS gain suppression in a large mode area Yb-doped optical fiber," *Proc. SPIE* **6873**, U63–U69 (2008).
- [34] Y. Imai and N. Shimada, "Dependence of stimulated Brillouin scattering on temperature distribution in polarization-maintaining fibers," *IEEE Photon. Technol. Lett.* **5**, 1335 (1993).
- [35] J. Hansryd, F. Dross, M. Westlund, P. A. Andrekson, and S. N. Knudsen, "Increase of the SBS threshold in a short highly nonlinear fiber by applying a temperature distribution," *J. Lightwave Technol.* **19**, 1691– (2001).
- [36] P. D. Dragic, C. Liu, G. C. Papen, and A. Galvanauskas, "Optical fiber with an acoustic guiding layer for stimulated Brillouin scattering suppression," in "Conference on Lasers and Electro-Optics/Quantum Electronics and Laser Science and Photonic Applications Systems Technologies," (2005), p. CThZ3.

- [37] B. G. Ward and J. B. Spring, “Brillouin gain in optical fibers with inhomogeneous acoustic velocity,” *Proc. SPIE* **7195**, 71951J (2009).
- [38] G. P. Agrawal, *Nonlinear Fiber Optics* (Academic Press, San Diego, 2001).
- [39] C.-H. Liu, B. Ehlers, F. Doerfel, S. Heinemann, A. Carter, K. Tankala, J. Farroni, and A. Galvanauskas, “810 W continuous-wave and single-transverse-mode fibre laser using 20 m core Yb-doped double-clad fibre,” *Electron. Lett.* **40**, 1471–1472 (2004).
- [40] K. O. Hill, B. S. Kawasaki, D. C. Johnson, “CW Brillouin laser,” *Appl. Phys. Lett.* **28**, 608 (1976).
- [41] J. Geng, S. Staines, Z. Wang, J. Zong, M. Blake, S. Jiang, “Highly stable low-noise Brillouin fiber laser with ultranarrow spectral linewidth,” *IEEE Photon. Technol. Lett.* **18**, 1813 (2006).
- [42] W. Guan and J. R. Marciante, “Single-frequency 1 W hybrid Brillouin/ytterbium fiber laser,” *Opt. Lett.* **34**, 3131–3132 (2009).
- [43] L. Zou, X. Bao, Y. Wan, F. Ravet, and L. Chen, “Distributed fiber Brillouin strain and temperature sensor with centimeter spatial resolution by coherent probe-pump technique,” *Proc. SPIE* **5855**, 68–71 (2005).
- [44] C. A. Galindez, F. J. Madruga, A. Ullan, M. Lopez-Amo and J. M. Lopez-Higuera, “Temperature sensing in multiple zones based on Brillouin fiber ring laser,” *J. Phys.: Conf. Ser.* **178**, 012017 (2009).
- [45] D. Strickland and G. Mourou, “Compression of amplified chirped optical pulses,” *Opt. Commun.* **56**, 219–221 (1985).
- [46] J. M. Fini, M. D. Mermelstein, M. F. Yan, R. T. Bise, A. D. Yablon, P. W. Wisk, and M. J. Andrejco, “Distributed suppression of stimulated Raman scattering in an Yb-doped filter-fiber amplifier,” *Opt. Lett.* **31**, 2550–2552 (2006).
- [47] E. Cumberbatch, “Self-focusing in non-linear optics,” *J. Inst. Maths Applics* **6**, 250 (1970).
- [48] G. Fibich and A. L. Gaeta, “Critical power for self-focusing in bulk media and in hollow waveguides,” *Opt. Lett.* **25**, 335–337 (2000).
- [49] D. C. Brown and H. J. Hoffman, “Thermal, stress, and thermo-optic effects in high average power double-clad silica fiber lasers,” *IEEE J. Quantum Elect.* **37**, 207–217 (2001).

- [50] W. F. Krupke, M. D. Shinn, J. E. Marion, J. A. Caird, and S. E. Stokowski, "Spectroscopic, optical, and thermomechanical properties of neodymium- and chromium-doped gadolinium scandium gallium garnet," *J. Opt. Soc. Am. B* **3**, 102–114 (1986).
- [51] D. E. Gray, *American Institute of Physics Handbook* (McGraw-Hill, 1972).
- [52] W. Koechner, *Solid State Laser Engineering* (Springer, 2006).
- [53] V. Gapontsev, D. Gapontsev, N. Platonov, O. Shkurkhin, V. Fomin, A. Mashkin, M. Abramov, and S. Ferin, "2 kW CW ytterbium fiber laser with record diffraction limited brightness," in "Conference on Lasers and Electro-Optics Europe," (2005), p. 508.
- [54] J. Limpert, S. Hofer, A. Liem, H. Zellmer, A. Tunnermann, S. Knoke and H. Voelckel, "100-W average-power, high-energy nanosecond fiber amplifier," *J. Lightwave Technol.* **75**, 477–479 (2002).
- [55] M. Faraday, "On the magnetization of light, and the illumination of magnetic lines of force," *Philos. Trans. R. Soc. London* **1**, 104–123 (1846).
- [56] P. S. Pershan, "Magneto-optical effects," *J. Appl. Phys.* **38**, 1482 (1967).
- [57] M. J. Freiser, "A survey of magneto-optic effects," *IEEE Trans. Magn.* **MAG-4**, 152 (1968).
- [58] E. Verdet, "Recherches sur les proprietes optiques developpees dans les corps transparents par l'action du magnetisme," *Ann. Chim. Phys.* **41**, 370–412 (1854).
- [59] A. Sommerfeld, *Optics, Vol. IV of Lectures on Theoretical Physics Series* (Academic, New York, 1964).
- [60] H. Becquerel, "The Faraday and Zeeman effects," *Comptes Rendu* **125**, 679–685 (1897).
- [61] J. H. V. Vleck, *The Theory of Electric and Magnetic Susceptibilities* (Oxford U. Press, New York, 1932).
- [62] H. Cole, "Magneto-optic effects in glass. part 1," *J. Soc. Glass Technol.* **34**, 220 (1950).
- [63] P. A. Schulz, "Wavelength-independent Faraday isolator," *Appl. Opt.* **28**, 4458–4464 (1989).
- [64] N. F. Borelli, "Faraday rotation in glass," *J. Chem. Phys.* **41**, 3289–3293 (1964).

- [65] M. J. Weber, *CRC Handbook of Laser Science and Technology Supplement 2: Optical Materials* (CRC Press, Boca Raton, FL, 1995).
- [66] J. H. Van Vleck and M. H. Hebb, "On the paramagnetic rotation of tysonite," *Phys. Rev.* **46**, 17 (1934).
- [67] J. T. Kohli, and J. E. Shelby, "Magnetic and magneto-optical properties of high-rare earth glasses," in "Ceramics Transactions, Vol. 28: Solid State Optical materials," (1992).
- [68] D. R. Lide, *CRC Handbook of Chemistry and Physics* (CRC Press, Boca Raton, FL, 2001).
- [69] M. McCaig and A. G. Clegg, *Permanent Magnets in Theory and Practice* (Pentech Press, Graham Lodge, UK, 1987).
- [70] E. H. Turner and R. H. Stolen, "Fiber Faraday circulator or isolator," *Opt. Lett.* **6**, 322 (1981).
- [71] G. W. Day, D. N. Payne, A. J. Barlow, and J. J. Ramskov-Hansen, "Faraday rotation in coiled, monomode optical fibers: isolators, filters, and magnetic sensors," *Opt. Lett.* **7**, 238 (1982).
- [72] J.-F. Lafortune, R. Vallee, "Short length fiber Faraday rotator," *Opt. Commun.* **86**, 497–503 (1991).
- [73] V. Annovazzi-Lodi, S. Donati, S. Merlo and A. Leona, "All-fiber Faraday rotator made by a multiturn figure-of-eight coil with matched birefringence," *J. Lightwave Technol.* **13**, 2349–2353 (1995).
- [74] E. Khazanov, N. Andreev, O. Palashov, A. Poteomkin, A. Sergeev, O. Mehl, and D. Reitze, "Effect of terbium gallium garnet crystal orientation on the isolation ratio of a Faraday isolator at high average power," *Appl. Opt.* **41**, 483–492 (2002).
- [75] R. Yasuhara, S. Tokita, J. Kawanaka, T. Kawashima, H. Kan, H. Yagi, H. Nozawa, T. Yanagitani, Y. Fujimoto, H. Yoshida, and M. Nakatsuka, "Cryogenic temperature characteristics of Verdet constant on terbium gallium garnet ceramics," *Opt. Express* **15**, 11255–11261 (2007).
- [76] K. Shiraishi, S. Sugaya, and S. Kawakami, "Fiber Faraday rotator," *Appl. Opt.* **23**, 1103–1106 (1984).
- [77] J. Ballato and E. Snitzer, "Fabrication of fibers with high rare-earth concentrations for Faraday isolator applications," *Appl. Opt.* **34**, 6848–6854 (1995).

- [78] G. P. Agrawal, *Lightwave Technology: Components and Devices* (Wiley, Hoboken, NJ, 2004).
- [79] T. Yoshino, “Theory for the Faraday effect in optical fiber,” *J. Opt. Soc. Am. B* **22**, 1856–1860 (2005).
- [80] <http://www.npphotonics.com/>.
- [81] L. Sun, S. Jiang, J. D. Zuegel, and J. R. Marciante, “Effective Verdet constant in a terbium-doped-core phosphate fiber,” *Opt. Lett.* **34**, 1699–1701 (2009).
- [82] Vytran Corporation, Operator’s manual: LDC-200 Automated Fiber Cleaver with Angled Cleave Option (2003).
- [83] Furukawa Electric Co. Ltd., User’s manual: S183PM fusion Splicer (2004).
- [84] C. A. Edwards, H. M. Presby, and C. Dragone, “Ideal microlenses for laser to fiber coupling,” *J. Lightwave Technol.* **11**, 252–257 (1993).
- [85] S. Yamashita, K. Hotate, M. Ito, “Polarization properties of a reflective fiber amplifier employing a circulator and a Faraday rotator mirror,” *J. Lightwave Technol.* **14**, 385–390 (1996).
- [86] C. R. Giles, “Suppression of polarisation hole-burning-induced gain anisotropy in reflective EDFAs,” *Electron. Lett.* **30**, 976–977 (1994).
- [87] M. Martinelli, “A universal compensator for polarization changes induced by birefringence on a retracing beam,” *Opt. Commun.* **72**, 341–344 (1989).
- [88] C. Vinegoni, M. Wegmuller, B. Huttner, N. Gisin, “All optical switching in a highly birefringent and a standard telecom fiber using a Faraday mirror stabilization scheme,” *Opt. Commun.* **182**, 335–341 (2000).
- [89] M. A. Quintela, J. M. Lopez-Higuera and C. Jauregui, “Polarization characteristics of a reflective erbium doped fiber amplifier with temperature changes at the Faraday rotator mirror,” *Opt. Express* **13**, 1368–1376 (2005).
- [90] T. Findakly, “Single-mode fiber isolator in toroidal configuration,” *Appl. Opt.* **20**, 3989–3990 (1981).
- [91] S. C. Rashleigh and R. Ulrich, “Magneto-optic current sensing with birefringent fibers,” *Appl. Phys. Lett.* **34**, 768 (1979).
- [92] R. H. Stolen, E. H. Turner, “Faraday rotation in highly birefringent optical fibers,” *Appl. Opt.* **19**, 842–845 (1980).

- [93] <http://www.advaluephotonics.com/>.
- [94] J. L. Cruz, M. V. Andres, and M. A. Hernandez, “Faraday effect in standard optical fibers: Dispersion of the effective Verdet constant,” *Appl. Opt.* **35**, 922–927 (1996).
- [95] V. Ramaswamy, I. P. Kaminow, P. Kaiser, and W. G. French, “Single polarization optical fibers: Exposed cladding technique,” *Appl. Phys. Lett.* **33**, 814 (1978).
- [96] T. Hosaka, K. Okamoto, T. Miya, Y. Sasaki, and T. Edahiro, “Low-loss single polarisation fibres with asymmetrical strain birefringence,” *Electron. Lett.* **17**, 530 (1981).
- [97] K. Okamoto, T. Edahiro, and N. Shibata, “Polarization properties of single-polarization fibers,” *Opt. Lett.* **7**, 569 (1982).
- [98] T. Katsuyama, H. Matsumura, and T. Suganuma, “Propagation characteristics of single polarization fibers,” *Appl. Opt.* **22**, 1748 (1983).
- [99] D. A. Nolan, G. E. Berkey, M. Li, X. Chen, W. A. Wood, and L. A. Zenteno, “Single-polarization fiber with a high extinction ratio,” *Opt. Lett.* **29**, 1855 (2004).
- [100] D. T. Walton, M. J. Li, D. A. Nolan, G. E. Berkey, X. Chen, J. Koh, J. Wang, S. Gray, and L. A. Zenteno, “Challenges in single-polarization fibers,” *Proc. SPIE* **5709**, 316 (2005).
- [101] M. Li, X. Chen, D. A. Nolan, G. E. Berkey, J. Wang, W. A. Wood, and L. A. Zenteno, “High bandwidth single polarization fiber with elliptical central air hole,” *J. Lightwave Technol.* **23**, 3454 (2005).
- [102] X. Chen, M. Li, J. Koh, and D. A. Nolan, “Wide band single polarization and polarization maintaining fibers using stress rods and air holes,” *Opt. Express* **16**, 12060–12068 (2008).
- [103] V. I. Kopp, V. M. Churikov, and A. Z. Genack, “Synchronization of optical polarization conversion and scattering in chiral fibers,” *Opt. Lett.* **31**, 571–573 (2006).
- [104] T. Schreiber, F. Roser, O. Schmidt, J. Limpert, R. Iliew, F. Lederer, A. Petersson, C. Jacobsen, K. Hansen, J. Broeng, and A. Tunnermann, “Stress-induced single-polarization single-transverse mode photonic crystal fiber with low nonlinearity,” *Opt. Express* **13**, 7621 (2005).
- [105] J. R. Folkenberg, M. D. Nielsen, and C. Jakobsen, “Broadband single-polarization photonic crystal fiber,” *Opt. Lett.* **30**, 1446–1448 (2005).

- [106] S. Zhang, V. I. Kopp, V. Churikov, and G. Zhang, “PANDA-based chiral in-fiber polarizer,” *Proc. SPIE* **7212**, 72120D (2009).
- [107] K. O. Hill and G. Meltz, “Fiber Bragg grating technology fundamentals and overview,” *J. Lightwave Technol.* **15**, 1263–1276 (1997).
- [108] R. Kashyap, *Fiber Bragg gratings* (Academic Press, San Diego, CA, 1999).
- [109] W. E. Gettys, F. J. Keller and M. J. Skove, *Physics, Classical and Modern* (McGraw-Hill, New York, 1989).
- [110] L. Sun, S. Jiang, J. D. Zuegel, and J. R. Marciante, “All-fiber optical isolator based on Faraday rotation in highly terbium-doped fiber,” *Opt. Lett.* **35**, 706–708 (2010).
- [111] L. Sun, S. Jiang, and J. R. Marciante, “All-fiber optical Faraday mirror using 56-wt% terbium-doped fiber,” *IEEE Photon. Technol. Lett.* **22**, 999–1001 (2010).
- [112] L. Sun, S. Jiang, and J. R. Marciante, “Compact all-fiber optical Faraday components using 65 wt% terbium-doped fiber with a record Verdet constant of -32 rad/(Tm),” *Opt. Express* **18**, 12191–12196 (2010).
- [113] J. Lenz, “A review of magnetic sensors,” *Proc. IEEE* **78**, 973–989 (1990).
- [114] A. Yariv and H. V. Winsor, “Proposal for detection of magnetic fields through magnetostrictive perturbation of optical fibers,” *Opt. Lett.* **5**, 87– (1980).
- [115] H. Okamura, “Fiber-optic magnetic sensor utilizing the Lorentzian force,” *J. Lightwave Technol.* **8**, 1558–1564 (1990).
- [116] V. Radojevic, D. Nedeljkovic, N. Talijan, D. Trifunovic and R. Aleksic, “Optical fibers with composite magnetic coating for magnetic field sensing,” *Journal of Magnetism and Magnetic Materials* **272-276**, e1755–e1756 (2004).
- [117] C. Tien, C. Hung, H. Chen, W. Liu and S. Lin, “Magnetic sensor based on side-polished fiber Bragg grating coated with iron film,” *IEEE Transactions on Magnetics* **42**, 2385–3287 (2006).
- [118] J. Marciante, N. Farmiga, J. Kondis, and J. Frederick, “Phase effects of secondary reflections on the performance of reflective liquid-crystal cells,” *Opt. Express* **11**, 1096–1105 (2003).
- [119] P. A. Williams, A. H. Rose, G. W. Day, T. E. Milner, and M. N. Deeter, “Temperature dependence of the Verdet constant in several diamagnetic glasses,” *Appl. Opt.* **30**, 1176–1178 (1991).

- [120] L. Sun, S. Jiang, and J. R. Marciante, “All-fiber optical magnetic-field sensor based on Faraday rotation in highly terbium-doped fiber,” *Opt. Express* **18**, 5407–5412 (2010).
- [121] X. Dong, N. Ngo, P. Shum, H. Tam and X. Dong, “Linear cavity erbium-doped fiber laser with over 100 nm tuning range,” *Opt. Express* **11**, 1689–1694 (2003).
- [122] C. Yeh and S. Chi, “A broadband fiber ring laser technique with stable and tunable signal-frequency operation,” *Opt. Express* **13**, 5240–5244 (2005).
- [123] X. He, X. Fang, C. Liao, D. N. Wang, and J. Sun, “A tunable and switchable single-longitudinalmode dual-wavelength fiber laser with a simple linear cavity,” *Opt. Express* **17**, 21773–21781 (2009).
- [124] M. Tang, X. Tian, X. Lu, S. Fu, P. Shum, Z. Zhang, M. Liu, Y. Cheng, and J. Liu, “Single-frequency 1060 nm semiconductor-optical-amplifier-based fiber laser with 40 nm tuning range,” *Opt. Lett.* **34**, 2204–2206 (2009).
- [125] M. Auerbach, P. Adel, D. Wandt, C. Fallnich, S. Unger, S. Jetschke, and H. Mueller, “10 W widely tunable narrow linewidth double-clad fiber ring laser,” *Opt. Express* **10**, 139–144 (2002).
- [126] H. Chen, F. Babin, M. Leblanc, and G. W. Schinn, “Widely tunable single-frequency erbium-doped fiber lasers,” *IEEE Photonics Technol. Lett.* **15**, 185–187 (2003).
- [127] M. Engelbrecht, A. Ruehl, D. Wandt, and D. Kracht, “Single-frequency ytterbium-doped fiber laser with 26 nm tuning range,” *Opt. Express* **15**, 4617–4622 (2007).
- [128] X. Zhu and R. Jain, “Watt-level 100-nm tunable 3- μ m fiber laser,” *IEEE Photonics Technol. Lett.* **20**, 156–158 (2008).
- [129] A. Luo, Z. Luo, and W. Xu, “Tunable and switchable multiwavelength erbium-doped fiber ring laser based on a modified dual-pass Mach-Zehnder interferometer,” *Opt. Lett.* **34**, 2235–2237 (2009).
- [130] V. A. Kozlov, R. L. Shubochkin, A. Kotze, E. Wetjen, A. L. G. Carter, H. Kung, D. A. Brown, and T. F. Morse, “Technique for continuous tuning of optical fiber lasers,” *Appl. Opt.* **37**, 4897–4901 (1998).
- [131] K. Sato, J. De Merlier, K. Mizutani, S. Sudo, S. Watanabe, K. Tsuruoka, K. Naniwae, and K. Kudo, “A compact external cavity wavelength tunable laser without an intracavity etalon,” *IEEE Photonics Technol. Lett.* **18**, 1191–1193 (2006).

- [132] S. Sudo, K. Mizutani, T. Okamoto, K. Tsuruoka, K. Sato, and K. Kudo, “C- and L-Band external cavity wavelength tunable lasers utilizing a wideband SOA with coupled quantum well active layer,” *IEEE Photonics Technol. Lett.* **20**, 1506–1508 (2008).
- [133] B. Pezeshki, E. Vail, J. Kubicky, G. Yoffe, S. Zou, J. Heanue, P. Epp, S. Rishton, D. Ton, B. Faraji, M. Emanuel, X. Hong, M. Sherback, V. Agrawal, C. Chipman, and T. Razazan, “20-mW widely tunable laser module using DFB array and MEMS selection,” *IEEE Photonics Technol. Lett.* **14**, 1457–1459 (2002).
- [134] M. A. Umyy, N. Madamopoulos, P. Lama, R. Dorsinville, “Dual Sagnac loop mirror SOA-based widely tunable dual-output port fiber laser,” *Opt. Express* **17**, 14495–14501 (2009).
- [135] D. A. Smith, M. W. Maeda, J. J. Johnson, J. S. Patel, M. A. Saifi, and A. Von Lehman, “Acoustically tuned erbium-doped fiber ring laser,” *Opt. Lett.* **16**, 387–389 (1991).
- [136] M. Kang, M. Lee, J. Yong, and B. Kim, “Characterization of wavelength-tunable single-frequency fiber laser employing acoustooptic tunable filter,” *J. Lightwave Technol.* **24**, 1812–1823 (2006).
- [137] R. Selvas, I. Torres-Gomez, A. Martinez-Rios, and J. A. Alvarez-Chavez, D. A. May-Arriola, P. LiKamWa, A. Mehta, and E. G. Johnson, “Wavelength tuning of fiber lasers using multimode interference effects,” *Opt. Express* **13**, 9439–9445 (2005).
- [138] K. Kieu and M. Mansuripur, “Tuning of fiber lasers by use of a single-mode biconic fiber taper,” *Opt. Lett.* **31**, 2435–2437 (2006).
- [139] Y. W. Song, S. A. Havstad, D. Starodubov, Y. Xie, A. E. Willner, and J. Feinberg, “40-nm-wide tunable fiber ring laser with single-mode operation using a highly stretchable FBG,” *IEEE Photonics Technol. Lett.* **13**, 1167–1169 (2001).
- [140] N. Q. Ngo, D. Liu, S. C. Tjin, X. Dong and P. Shum, “Thermally switchable and discretely tunable comb filter with a linearly chirped fiber Bragg grating,” *Opt. Lett.* **30**, 2994–2996 (2005).
- [141] Y. Han, X. Dong, J. Lee and S. Lee, “Wavelength-spacing-tunable multi-channel filter incorporating a sampled chirped fiber Bragg grating based on a symmetrical chirp-tuning technique without center wavelength shift,” *Opt. Lett.* **31**, 3571–3573 (2006).

- [142] X. Jia, Y. Liu, L. Si, Z. Guo, S. Fu, G. Kai, X. Dong, “A tunable narrow-line-width multi-wavelength Er-doped fiber laser based on a high birefringence fiber ring mirror and an auto-tracking filter,” *Opt. Commun.* **281**, 90–93 (2008).
- [143] Y. Shen, C. Gu, L. Xu, A. Wang, H. Ming, Y. Liu, and X. Wang, “A novel 852-nm tunable fiber laser,” *Chinese Opt. Lett.* **7**, 1022–1023 (2009).
- [144] T. Taunaya, P. Bernagea, G. Martinellia, M. Douaya, P. Niaya, J. F. Bayonb and H. Poignantb, “Photosensitization of terbium doped alumino-silicate fibres through high pressure H_2 loading,” *Opt. Commun.* **133**, 454–462 (1997).
- [145] Y. Chen and W. T. Joines, “A linear approximation of the coupling coefficient in the WDM coupler,” *Microwave Opt. Technol. Lett.* **37**, 12–15 (2003).
- [146] B. Ortac, A. Hideur, T. Chartier, M. Brunnel, C. Ozkul, and F. Sanchez, “90-fs stretched-pulse ytterbium-doped double-clad fiber laser,” *Opt. Lett.* **28**, 1305–1307 (2003).
- [147] J. R. Buckley, F. W. Wise, and F. O. Ilday, “Femtosecond fiber lasers with pulse energies above 10 nJ,” *Opt. Lett.* **30**, 1888–1890 (2005).
- [148] Y.-X. Fan, F.-Y. Lu, S.-L. Hu, K.-C. Lu, H.-J. Wang, X.-Y. Dong, and G.-Y. Zhang, “105-kW peak-power double-clad fiber laser,” *IEEE Photonics Technol. Lett.* **15**, 652–654 (2003).
- [149] F. Roser, J. Rothhard, B. Ortac, A. Liem, O. Schmidt, T. Schreiber, J. Limpert, and A. Tunnermann, “131 W 220 fs fiber laser system,” *Opt. Lett.* **30**, 2754–2756 (2005).
- [150] K. Shiraki, M. Ohashi, and M. Tateda, “Performance of strain-free stimulated Brillouin scattering suppression fiber,” *J. Lightwave Technol.* **14**, 549–554 (1996).
- [151] J. Toulouse, “Optical nonlinearities in fibers: Review, recent examples, and systems applications,” *J. Lightwave Technol.* **23**, 3625–3641 (2005).
- [152] V. I. Kovalev and R. G. Harrison, “Suppression of stimulated Brillouin scattering in high-power single-frequency fiber amplifiers,” *Opt. Lett.* **31**, 161–163 (2006).
- [153] H. Adachihara, O. Hess, E. Abraham, P. Ru, and J. V. Moloney, “Spatiotemporal chaos in broad-area semiconductor lasers,” *J. Opt. Soc. Am. B* **10**, 658–665 (1993).

- [154] D. J. Bossert, J. R. Marciante, and M. W. Wright, “Feedback effects in tapered broad-area semiconductor lasers and amplifiers,” *IEEE Photonics Technol. Lett.* **7**, 470–472 (1995).
- [155] J. R. Marciante and G. P. Agrawal, “Spatio-temporal characteristics of filamentation in broad-area semiconductor lasers,” *IEEE J. Quantum Electron.* **33**, 1174–1179 (1997).
- [156] D. F. Welch, “A brief history of high-power semiconductor lasers,” *IEEE J. Sel. Top. Quantum Electron.* **6**, 1470–1477 (2000).
- [157] P. L. Baldeck, F. Raccah, and R. R. Alfano, “Observation of self-focusing in optical fibers with picosecond pulses,” *Opt. Lett.* **12**, 588–589 (1987).
- [158] Y. M. Hua, Q. Li, Y. L. Chen, and Y. X. Chen, “The ring structure of self-focusing light in optical fibres,” *Opt. Commun.* **79**, 459–461 (1990).
- [159] G. Tempea and T. Brabec, “Theory of self-focusing in a hollow waveguide,” *Opt. Lett.* **23**, 762–764 (1998).
- [160] R. L. Farrow, D. A. V. Kliner, G. R. Hadley, and A. V. Smith, “Peak-power limits on fiber amplifiers imposed by self-focusing,” *Opt. Lett.* **31**, 3423–3425 (2006).
- [161] P. C. Becker, N. A. Olsson, and J. R. Simpson, *Erbium-doped Fiber Amplifiers: Fundamentals and Technology* (Academic Press, San Diego, 1999).
- [162] C.-J. Chen, P. K. A. Wai, and C. R. Menyuk, “Self-starting passively mode-locked lasers with fast saturable absorbers,” *Opt. Lett.* **20**, 350–352 (1995).
- [163] C. D. Brooks and F. Di Teodoro, “Multimegawatt peak-power, single-transverse-mode operation of a 100 μ m core diameter, Yb-doped rodlike photonic crystal fiber amplifier,” *Appl. Phys. Lett.* **89**, 111119 (2006).
- [164] L. Sun and J. R. Marciante, “Filamentation analysis in large-mode-area fiber lasers,” *J. Opt. Soc. Am. B* **24**, 2321–2326 (2007).